UNIVERSITY OF SOUTHAMPTON

FACULTY OF ENGINEERING AND THE ENVIRONMENT

Bone Matrix Material Properties on the Micro- and Nanoscale

by

Orestis L. Katsamenis

Thesis for the degree of Doctor of Philosophy

November 2012

UNIVERSITY OF SOUTHAMPTON

FACULTY OF ENGINEERING AND THE ENVIRONMENT

Thesis for the degree of Doctor of Philosophy

BONE MATRIX MATERIAL PROPERTIES ON THE MICRO- AND NANOSCALE

by Orestis Linos Katsamenis

ABSTRACT

The evaluation of fracture risk in osteoporotic patients, which is still mostly based on bone mineral density (BMD) measurements, constitutes a major clinical challenge. Despite the fact that BMD is highly correlated with fracture risk in large populations, it unfortunately fails to be an accurate predictor for the individual. To increase the accuracy of fracture risk evaluation, a better understanding of all factors affecting bone fracture behaviour, including (but not limited to) BMD, is needed. This means a deeper understanding of bone's material properties and structure-function relationship is required.

Mammalian bones are composed of mineralized type I collagen fibrils immersed in a matrix of non-collagenous proteins (NCPs). This fundamental unit assembles into progressively larger features in a hierarchical manner, supplying bone with various "lines of defence" against catastrophic failure. Optimal load transfer and energy dissipation mechanisms have, to some extent, been discovered within bone's nanostructure on which NCPs have been proposed to play a crucial role. Yet, it is largely unknown if integration of such mechanisms occurs to any other hierarchical level. This thesis attempts to answer this question for the osteonal level of cortical bone. The feature dominating this level is a hollow tubular structure of a few hundred micrometres in diameter, the *osteons*, consisting of concentric aligned lamellae. Lamellae range from 3 -10 μm in thickness and between them lie interlamellar areas (often referred to as thin lamellae).

This thesis is the outcome of three studies. The first focuses on the aforementioned osteonal features, namely lamellae and interlamellar areas, studying their structure, composition and their mechanical behaviour during loading. For this purpose a series of experimental techniques were used including μ-RAMAN microscopy, atomic force microscopy (AFM), AFM cantilever-based nanoindentation and in-situ AFM analysis during microtensile testing. It was shown that interlamellar areas differ from lamellae by (a) being collagen-deficient and NCP-rich, (b) having a

different arrangement of collagen fibres, (c) being more compliant when no load is applied to the bone and (d) exhibiting higher strains under loading conditions. Finally, stable crack propagation was for the first time captured in a time-lapsed fashion within the interlamellar areas by means of AFM, further proving their significant contribution towards fracture toughness.

The second is a technical study for the development of a method capable for generating full fracture-resistance curves (R-curves) of small bone samples where crack propagation cannot easily be observed. The outcome was the development of a novel computer-aided videography method, "whitening-front tracking" method, which uses the whitening effect formed by the development of the damage in front of the crack-tip (frontal process zone) to indirectly track the crack propagation which is needed for the generation of the R-curve.

The new method was then applied in the third study to correlate the ultimate toughness of human cortical bone, i.e. "fracture toughness" and "crack growth resistance" at the tissue-level, with the elasticity inhomogeneity between lamella and interlamellar areas at the osteonal-level and the damage-formation resistance at the micro-level. In this study the mechanical properties of bone in tissue-, micro- and osteonal-level were measured by means of the "whitening front tracking", reference point indentation (RPI) and AFM cantilever-based nanoindentation methods respectively. The results revealed a correlation of toughness and crack-growth resistance at the tissue-level with the elastic inhomogeneity between the sub-osteonal features. That is, the higher the difference between the moduli of lamellae and interlamellar areas the higher the toughness of the tissue. Furthermore, toughness and crack-growth resistance correlated with bone's "resistance to damage" as it was characterised by RPI at the micro-level. Finally, these measured suggested age-related degradation of the mechanical properties at all three levels measured.

Overall, the results presented in this thesis propose that osteons are the principal component of a previously unknown proactive mechanism which transfers load and movement in a manner analogous to engineered "elastomeric bearing pads". This ability originates from the elastic inhomogeneity between the lamellae and the interlamellar areas which allows osteons to adapt to high stresses without damage formation.

Contents

List of tables

List of figures [1]

[1] For reproduction of copyrighted material, i.e. figures and tables, permission has been obtained from the legal owner via the Copyright Clearance Center (http://www.copyright.com/)

DECLARATION OF AUTHORSHIP

I, Orestis Katsamenis declare that the thesis entitled "BONE MATRIX MATERIAL PROPERTIES ON THE MICRO- AND NANOSCALE" and the work presented in the thesis are both my own, and have been generated by me as the result of my own original research. I confirm that:

- this work was done wholly or mainly while in candidature for a research degree at this University;
- where any part of this thesis has previously been submitted for a degree or any other qualification at this University or any other institution, this has been clearly stated;
- where I have consulted the published work of others, this is always clearly attributed;
- where I have quoted from the work of others, the source is always given. With the exception of such quotations, this thesis is entirely my own work;
- I have acknowledged all main sources of help;
- where the thesis is based on work done by myself jointly with others, I have made clear exactly what was done by others and what I have contributed myself;
- parts of this work have been published as: Katsamenis, O.L., Chong, H.M.H., Andriotis, O.G., Thurner, P.J., 2012. "Load-Bearing in Cortical Bone Microstructure: Selective Stiffening and Heterogeneous Strain Distribution at the Lamellar Level". Journal of the Mechanical Behavior of Biomedical Materials

Signed: ……..

Date:…….

Acknowledgements

My most sincere thanks are due to:

my principal supervisor, Dr. Philipp J. Thurner, for entrusting me with his idea but most importantly for letting me free to mess with it;

Prof. Ian Sinclair for his critical, yet constructive, comments during the development of the "whitening-front tracking" method;

Dr. Harold M H Chong for allowing me access to the micro-RAMAN facilities of his group;

and Orestis Andriotis, Tom Jenkins, Nick Udell, Tsiloon Li and Dr. Louise Coutts for the fruitful discussions during our research-group meetings;

A special thank I owe to Sofia (Dr. Sofia Michopoulou) primarily for her endless encouragement and support but also for helping me with the "whitening-front tracking" method and for proof-reading this thesis. *Thank you for always being there for me!*

Finally, I would also like to acknowledge the Faculty of Engineering and the Environment of the University of Southampton, Asylum Research and EPSRC for the financial support of this project.

to my parents Linos and Rodanthi,
and my sister Danai.

Definitions and Abbreviations

μCT	micro-Computed Tomography
3D	Three Dimensional
AFM	Atomic Force Microscopy/e
ARF cycle	Activation, Resorption and Formation cycle
ASTM	American society for testing and materials standard
BAG-75	Bone Acidic Glycoprotein -75
BMD	Bone Mineral Density
BSP	Bone Sialoprotein
BSU	Basic Structural Unit
CFM	Chemical Force Microscopy
CT	Computed Tomography
DIC	Digital Image Correlation
DMP-1	Dentin Matrix Protein-1
DXA	Dual X-ray Absorptiometry
ED	Average Energy Dissipated
EDTA	Ethylenediaminetetraacetic Acid
ESEM	Environmental Scanning Electron Microscope
FS	Force Spectroscopy
HAP	Hydroxyapatite
HEPES	(4-(2-hydroxyethyl)-1-piperazineethanesulfonic acid)
IDI	Indentation Distance Increase
LEFM	Linear Elastic Fracture Mechanics
MEPE	Matrix Extracellular Glyco-phosphoprotein
NCP	non-Collagenous Protein
NHS	National Health System (usually referring to the UK)
NIH	National Institute of Health

List of Symbols

Fracture toughness

A_{pl}	Area under the load-displacement curve (N*mm)
B	Sample's thickness (m)
b_0	Initial un-cracked ligament (m)
E_f	Flexural modulus (Pa)
G	Strain-energy release rate ($J.m^2$)
J	J-integral ($J.m^{-2}$)
K	Stress intensity factor ($Pa.m^{1/2}$)
K_c	Critical stress intensity factor ($Pa.m^{1/2}$)
K_{eff}	Equivalent critical stress intensity factor ($Pa.m^{1/2}$)
P	Load (N)
S	Support span (m)
v	Displacement (m)
W	Sample's width (m)
a	Crack length (m)
θ	Angle
μ	shear modulus (Pa)
σ_{app}	Applied stress (Pa)
σ_{ij}	Local stresses (Pa)

Indentation analysis

A	Projected contact area of the indenter (m^2)
A	Contact area between the material and the indenter at the position of maximum load (m^2)
a,m	*Constants* (-)
E_r	Effective (or reduced) elastic modulus (Pa)
h	Indentation depth (m)
h	Load (N)
H	Hardness ($N.m^{-2}$)
h_c	Contact depth (m)
h_f	Indentation depth left on the surface (m)
h_{max}	Maximum indentation depth (m)
P	Force (N)
S	Stiffness (N/m)
β	*correction factor* (-)

Mechanics

E	Elastic modulus (Pa)
G	Shear modulus (Pa)
R_{ms}	Roughness root mean square (m)
v	Poisson's ratio (-)

Spectroscopy

a	Polarizability ($C.m^2.V^{-1}$)
E_{elect}	Electromagnetic Energy (Joule)
E_{nucl}	Nuclear energy (Joule)
E_{rot}	Rotational energy (Joule)
E_{tottal}	Total Energy (Joule)
E_{trans}	Energy of molecule parallel translation (Joule)
E_{vib}	Vibrational energy (Joule)
h	*Plank's constant*
J	Rotational quantum number
n	Electronic energy state (-)
r	Distance between the nuclei (m)
r_{eq}	Equilibrium distance distance between the nuclei (m)
u	Vibrational quantum number
u	Wavenumber (cm^{-1})
λ	wavelength (m)
v	radiation frequency (Hz)

Statistics

p	p-value probability
r	Pearson product-moment correlation coefficient (-)

Chapter 1

Introduction

1.1 Background

Bone is a complex nanocomposite material which in its healthy state provides high stiffness and toughness. However, age and/or disease related changes in bone lead to over 200,000 fractures in the UK every year. In addition to the significant reduced quality of life for patients suffering from a fracture, this also results in an estimated cost of approximately £1.7 bn [*Bukhari 2009*] for the National Health Service (NHS). The equivalent cost in the USA resulting from approximately 1.5 million fractures has been estimated between $5 -$10 bn [*Riggs and Melton 1995*]. Doubling of this cost is soon to be expected in the western world due to aging and increased lifespan of the population [*Bukhari 2009*].

These figures show the importance of the accurate fracture risk assessment in addition to the effective fracture risk reduction treatment. In the current clinical practice, the gold standard to predict bone fracture risk is based on the assessment of bone mineral density (BMD) by means of dual X-ray absorptiometry (DXA). Other risk factors such as oestrogen status, age, sex and lifestyle are also taken into consideration [*Kanis 2002b; Tremollieres et al. 2010*]. With the BMD having been associated with the risk of fracture, the fracture risk reduction treatment consequently is also focused on restoring BMD to the normal levels, i.e. within 2.5 standard deviations of the BMD of the healthy young population [*Kanis 2002b; Kanis 2007*]. However, bone fragility, and thus fracture risk as well, is also affected by other factors that are not taken into consideration in everyday clinical practice. These factors include among others body size, bone mass and bone mass distribution [*Riggs and*

Melton 1995]. Others, like disease [*Cowin and Corporation 2001*], and genetic background [*Jepsen et al. 2001*] are known to affect bone fragility almost independently of bone mass [*Hui et al. 1988; Kanis et al. 2005a*]. As a result, BMD fails to accurately assess the fracture risk for the individual [*Schuit et al. 2004; Siris et al. 2004a*] despite the fact that it is a good predictor of the fracture risk in the population [*Kanis 2002a*]. This limitation has been attributed to the inability of BMD-based measurements to provide any information regarding *bone quality*.

The term "bone quality" essentially includes all parameters and properties, including (but not limited to) bone mass or BMD, which influence bone mechanical and fracture behaviour [*Felsenberg and Boonen 2005; Ulrich et al. 1997a*]. For more than twenty years, research on bone quality has been conducted to elucidate specific parameters and the way each one of them affects bone fragility. Since the early 1980s, variations of the degree of mineralisation in bones have been linked with different mechanical properties of the tissue [*Currey 1984*], while almost at the same period, attention was drawn on the importance of collagen maturation and orientation on these properties [*Eyre et al. 1988; Viguet-Carrin et al. 2006*]. With the advent of micro-computed tomography (μCT) it has become clear that the microarchitecture of trabecular bone is also important for bone quality [*Feldkamp et al. 2009; Fratzl et al. 2004; Ulrich et al. 1997b*]. Beyond these particular findings it has been shown that there is an overarching hierarchical structure – function relationship, which is perhaps the "holy grail" in understanding the origin of the "material" properties of bone [*Weiner et al. 1999; Weiner and Wagner 1998a*]. Yet, the hierarchical structure – function relationship and its relevance for bone fracture toughness is still not very well understood. The complexity encountered is due to the fact that the final mechanical properties of bone derive from both the individual properties of the different hierarchical components and the way these components interact with each other [*Nyman et al. 2005; Rho et al. 1998b; Weiner and Wagner 1998a*].

From a materials science viewpoint bone can be described as a fibrous composite structure composed of mineralized type I collagen fibrils immersed into a matrix of mineralized noncollagenous proteins (NCPs) [*Braidotti et al. 2000b; Braidotti et al. 1997b*]. These fundamental elements are hierarchically organised in more than four different levels which span from the nano- up to

the macroscale [*Fratzl and Weinkamer 2007; Weiner and Wagner 1998a*]. On the nanoscale, the arrangement of basic elements of collagen type I and biological apatite nanocrystals [*LeGeros 1981*] into mineralized collagen fibrils, and further into progressively larger structural features is steered by NCPs [*Roach 1994b*]. The result of this complex arrangement on the microscale are the lamellae, which are essentially the micro-building blocks of mature compact bone [*Rho et al. 1998b*]. Each lamella can be described as a hierarchical composite of collagen fibrils, mineral and NCPs, which assemble together in sub-layers. According to the current model of the lamellar structure, within a single lamella, these sub-layers progressively rotate with respect to each other in a plywood-like fashion. The resulting lamella can vary in thickness from 3 up to 10 μm [*Giraud-Guille 1988; Weiner et al. 1999*]. Further concentric arrangement of cylindrical lamellae results in a hollow cylindrical laminate structure, known as an osteon, which surrounds a blood vessel [*Fratzl and Weinkamer 2007*]. In a single osteonal lamella, the previously mentioned sub-layers rotate to an angle from roughly 10° to 60° with respect to the osteon long axis [*Wagermaier et al. 2006*]. Finally, between two subsequent lamellae lies a putatively NCP-rich [*Derkx et al. 1998*] interlamellar area where the mineralized collagen fibrils are oriented perpendicularly to the longitudinal axis of the osteon [*Ascenzi and Benvenuti 1986; Reid 1986; Ziv et al. 1996*]. This area is often called "thin", "dense" or "transverse" lamella [*Marotti 1993; Reid 1986*], and has been characterized as a transition zone between lamellae [*Ziv et al. 1996*].

In bone, similarly to all hierarchically structured materials, the mechanical and eventually the fracture behaviour of a given hierarchical level strongly depends on the properties and the behaviour of the components of the lower hierarchical levels. Recent computational studies took an important step towards understanding this structure – function relationship by incorporating multiple hierarchical levels into their models. Hamed et al., using a bottom-up approach of four different hierarchical levels, with the output of a lower level serving as the input for the modelling of the higher one, were able to predict the effective elastic moduli of cortical bone [*Hamed et al. 2010*]. More recently, Vaughan et al. using a three-scale finite element model, studied the effect of mineral volume fraction, mineral aspect ratio and lamellar orientation on the elastic properties of cortical and trabecular bone [*Vaughan et al. 2012*]. These studies

clearly show that the properties of the higher hierarchical levels depend upon the properties of the lower ones.

The hierarchical structure supplies bone with a number of toughening mechanisms which protect bone against catastrophic failure. The first line of defence against bone fracture appears on the nanoscale, with NCP-mediated optimal load transfer between mineralized collagen fibrils [*Gupta et al. 2006b*]. Specifically, NCPs form a matrix (soft phase) around the mineralized collagen fibrils (hard phase), which dissipates energy during fracture [*Adams et al. 2008; Fantner et al. 2007; Fantner et al. 2005a*] and can also re-heal in a molecular fashion [*Zappone et al. 2008*].

On the higher (sub osteonal-) level, single lamellae, interlamellar areas and cement lines exhibit different mechanical properties with single lamellae exhibiting higher modulus of elasticity than interlamellar areas and cement lines [*Donnelly et al. 2006; Gupta et al. 2006a*]. The source of this dissimilarity is not clear yet, but it most likely is a combination of the inner architecture, i.e. arrangement of the fibres [*Gupta et al. 2006a*], composition [*Derkx et al. 1998; Nanci 1999*] and degree of mineralisation [*Donnelly et al. 2006*]. During failure, crack propagation preferably occurs through the interlamellar areas and cement-lines [*Peterlik et al. 2005*] while single lamellae act as crack barriers deflecting/twisting or even stopping the cracks [*Gupta et al. 2006a; Koester et al. 2008; Launey et al. 2010*]. Likewise, at the osteonal level cracks tend to deflect on the osteons and preferably propagate through the interstitial bone [*Nalla et al. 2005*]. Interestingly, both cement lines and interlamellar areas which facilitate crack propagation are enriched in NCPs [*Derkx et al. 1998; Nanci 1999*] suggesting that these proteins have an important role on the ultimate fracture behaviour of the tissue.

1.2 Objectives and Scope

All of the above clearly suggest that the ultimate bone toughness is the result of the synergistic action of different toughening mechanisms found in the various levels of bone architecture. It is noteworthy that within the different hierarchical levels, NCP-rich interfaces and interfacial structures (e.g. fibrillar interfaces, cement lines, interlamellar areas etc) appear to have an important contribution towards fracture toughness. Yet, these interfaces are not clearly

defined in all hierarchical levels and the exact mechanisms by which they contribute to the ultimate toughness of the material are not fully understood. A key challenge, formulated by Rho et al. that requires answering is "…*the lack of knowledge of the properties of the individual constituents [of cortical bone] and their associations in the matrix. What is the nature of the interfaces between the constituents of bone at all length scales?*" [*Rho et al. 1998b*].

To access the properties of these constituents and their contribution to the ultimate material properties of bone, we need to look closer onto each hierarchical level and study its behaviour during loading and fracture. We need to understand how intrinsic mechanisms like optimal load transfer and energy dissipation mechanism are integrated at the various hierarchical levels. This study, focusing on the osteonal level of bone and tries to shed light onto the importance of the NCP-rich interfaces. How toughening mechanisms similar to the optimal load transfer and energy dissipation mechanism found in the nanoscale are integrated in this higher hierarchical level; and most importantly, how the NCPs are involved on these mechanisms? Based on the idea that the "*lamella : NCP-rich interlamellar area : lamella*" interaction found on this level to have a self-similarity with the "*mineralised collagen fibril : NCP : mineralised collagen fibril*" interaction of the nanoscale, studying this system one should be able to extract information about the contribution of the NCPs to the toughening mechanisms of bone tissue.

The present work lies on the hypothesis that in bone, the interfaces enriched in NCPs, such as the cement lines and the interlamellar areas, are in a large part responsible for tuning the matrix material properties in order to achieve high toughness and hence high fracture resistance. It aims to study the toughening mechanisms which act at the osteonal-level of cortical bone tissue and analyse their relationship with the NCP-content of the matrix. This knowledge would further our understanding of bone structure-function relationship and it could lay important groundwork based on which more accurate fracture risk diagnostic tools and better treatments could be developed.

For this purpose, experimental investigations were carried out in order to characterise the mechanical behaviour of the secondary osteons of cortical bone and associate their behaviour with their structure and composition. These properties were then correlated with the damage susceptibility and the ultimate

mechanical properties of the tissue demonstrating the contribution of the NCP-rich interfaces to these properties.

1.3 Layout of the Thesis

In this thesis bovine bone was initially used to study mechanical behaviour of the various osteonal features, namely osteonal lamellae and interlamellar areas, as well as the structure and composition. Using cantilever-based nanoindentation, in-situ microtensile testing during atomic force microscopy (AFM), optical microscopy and digital image correlation (DIC), these experiments revealed evidence of a previously unknown mechanism which transfers load and movement in a manner analogous to the engineered "elastomeric bearing pads" used in large engineering structures. Furthermore, μ-RAMAN microscopy investigations showed compositional differences between lamellae and interlamellar areas with the latter exhibiting lower collagen content but an increased concentration of noncollagenous proteins (NCPs). Hence, NCPs enriched areas on the microscale seem to be similarly important for bone failure as they are on the nanoscale. Finally, stable crack propagation within a single osteon in a time-lapsed fashion was captured on the nanoscale by in-situ microtensile tests during AFM imaging proving their significant contribution towards bone's fracture toughness.

After this, the next step was to move from the animal model to human specimens and study the correlation between the properties measured at the osteonal level and the ultimate toughness of the tissue. For this, a method capable to measure the fracture toughness of the small (miniature) human cortical bone samples had to be developed as the only currently known alternative technique required the use of in situ microtensile testing during environmental scanning electron microscopy (ESEM) [*Koester et al. 2008; Nalla et al. 2003*]. The development of such a technique is presented in the second study. The new method ("Whitening Front Tracking" method) is a videography method capable of generating crack extension resistance curves in small bone samples, i.e. with cross-sectional dimensions of 1 mm x 1 mm or less, tested in three-point bending. The approach is based on indirect tracking of the crack front propagation via monitoring of the so-called "whitening zone", which develops in front of the crack tip. The main objectives of this study were (i) to quantify the correlation between the "whitening effect" and the crack

propagation and (ii) to develop a computer-aided methodology to generate crack propagation resistance curves for fracture toughness evaluation of small bone specimens. The results showed that the proposed technique has the ability to generate full crack extension

Finally in the third study, the multiscale correlation analysis study mentioned above is presented. This study investigates the fracture resistance of human cortical bone at the tissue level and its relationship with the properties measured at lower hierarchical levels, namely osteonal, and sub-osteonal level. The mechanical properties of the tissue where assessed in the tree hierarchical levels by means of videography fracture toughness, reference point indentation (RPI) and AFM cantilever-based nanoindentation respectively. The results reveal an association of fracture toughness and crack growth toughness of the bone at the tissue level with the crack initiation resistance of the micro-level and nanoelasticity inhomogeneity of the sub-osteonal level.

This thesis is divided into two sections. In the first section (Section I) the basic background information to this research project has been presented. This includes the basic biology, the composition and the structure and nanomechanical properties of the bone tissue (chapter 2), the clinical question based on which this project was designed (chapter 3) and the methods employed to address this problem (chapter 4). In the second section (Section II), the findings of this project are presented in three consecutive chapters as presented above. That is, the nanomechanical characterisation of the osteonal features along with the structure and composition analysis are been presented in chapter 5, the development of the "whitening-front tracking" method in chapter 6, and the multiscale correlation analysis of the human bone samples in chapter 7. Finally, a general discussion regarding the outcomes, the limitations and the potentials for future work is presented in chapter 8.

Chapter 2

Literature Review

This chapter consists of two sections. In the first section, the basic background information about bone biology and structure, in both the micro and macro scale is discussed. The second section, discusses the factors that contribute to the strength and toughness of bone tissue, the degradation of these properties due to osteoporosis and the fracture risk associated with it.

2.1 Bone

Bone is an important component of the skeletal system and its main role is to provide mechanical stability, protection and locomotion to the body. It also plays a significant role in the metabolic procedure. In the following sections these properties of bone will be introduced and a short overview will be attempted.

2.1.1 Bone and Skeletal System

The skeletal system is a body structure consisting of individual bones and soft tissue, like ligaments which hold individual bones together. The main purpose of the skeletal system is to provide mechanical stability to the body, protection to the vital organs and along with muscles to facilitate the motion of the body [*Nordin and Frankel 2001*]. The main component of the skeletal system is the bone, which is the most rigid and hard of all tissues. This property, is attributed to the inorganic salts, mainly impure hydroxyapatite ($Ca_{10}(PO_4)_6(OH)_2$), which grow into the organic matrix of the bone tissue. This complex structure results in a rigid and hard material able to serve the purposes mentioned earlier.

The skeletal system also plays a significant role in the metabolic procedure. More specifically, the bony skeleton is the main storage of calcium and phosphates of the human body (99% of body's calcium is stored there), and together with the spleen and liver comprise the main producers of blood cells [*Gray and Standring 2005*].

A common classification of skeleton is based on the shape of each individual bone. According to this, bones fall in the following four categories: (a) *long bones*; (b) *short bones*; (c) *flat bones* and finally (d) *irregular bones* (cf §2.1.5.1) [*Gray and Standring 2005*].

This study is focused on long bones, and more specifically on the cortical part of bone derived from the femur. For this reason only the structure of long bones will be discussed below in greater detail.

2.1.2 Composition of Bone

2.1.2.1 Mineral

As mentioned earlier, bone is a complex material consisting of inorganic salts, the organic matrix, cells and water. More specifically, 65% $^{w}/_{w}$ of bone consists of impure hydroxyapatite (HAP) ($Ca_{10}(PO_4)_6(OH)_2$) crystals in the form of needles and rods. Plate-like crystals have also been reported. Impurities could be Carbon (Carbonate Apatite or Dahlite or Pseudo-apatite - $Ca_5(PO_4,CO_3)_3F$), Magnesium, Fluoride (Fluorapatite - $Ca_5(PO_4)_3F$), etc. These ions can substitute the Hydroxide diatom of the HAP crystals (hydroxyl-deficient HAP), like fluoride (F^-) and carbonates (CO_3^{2-}) or they can be absorbed into the crystals surface. **Table 2-1** summarizes the chemical composition of bone as obtained by numerous analytical techniques [*Cowin and Telega 2003*].

2.1.2.2 Collagen

Organic matrix comprises the rest 35 % $^{w}/_{w}$ from which 90 % is collagen. The most abundant type is type I collagen while types II, V, XII are also present. The collagen molecules are secreted by the osteoblasts (cf. §2.1.3) and cross-linked in the extracellular matrix. The resulting structure then serves as a scaffold for the deposition of the mineral crystals. Although, collagen is the final "recipient" of the new formed mineral crystals, up until recently it was widely accepted that it does not directly involves in the mineral formation process

which was thought to be a noncollagenous protein-mediated process [*Gray and Standring 2005; Hollinger 2005*]. This model though has been recently apposed by L. B. Gower and the co-workers (cf. §2.1.4). A more thorough description about the collagen's molecular structure is given in §0.

2.1.2.3 Non-collagenous proteins

The remaining 5 –10 % of the organic matrix consists of non-collagenous proteins (NCPs). Although the role of these proteins is not entirely clear, they appear to contribute to the organisation and mineralisation of bone [*Cowin and Telega 2003; Hollinger 2005*]. The following section makes an effort to summarize the most important NCPs from each family.

Small Integrin Binding LIgand with N-Glycosylation (SIBLING) proteins as named by Fisher *et al.* [*Fisher et al. 2001; Hollinger 2005*] are the proteins that carry N-glycosylated residues –the term "Glycosylation" refers to the enzymatic process that links saccharine to produce polysaccharides or oligosaccharides, attached to organic molecules such as proteins. N-glycosylated means that the produced glycan is attached to a nitrogen of the protein molecule. Members of this family are the Osteopontin (OPN), the Bone Sialoprotein (BSP), the Dentin Matrix Protein-1 (DMP-1), the Dentin Sialoprotein, and the Matrix Extracellular Glyco-phosphoprotein (MEPE).

Table 2-1: Chemical Composition of Bone [*Cowin and Telega 2003*]

	Bovine Cortical Bone (wt % of whole bone)	Range in Literature for Healthy Adult Whole Bone (wt % of ash)
Calcium	16.7	32.6 – 39.5
Magnesium	0.436	0.32 – 0.78
Sodium	0.731	0.26 – 0.82
Potassium	0.055	–
Strontium	0.035	–
Phosphorus	12.47	13.1 – 18.0
Carbonate	3.48	3.2 – 13.0
Citrate	0.863	0.04 – 2.67
Chloride	0.077	–
Fluoride	0.072	0.02 – 0.207

Apart from the SIBLING proteins, there are also non-SIBLING proteins, such as the Bone Acidic Glycoprotein -75 (BAG-75) which inhibits osteoclasts activity. One of the most abundant NCP is Osteonectin which has the ability to bind calcium due to its calcium-binding domains [*Cowin and Telega 2003; Hollinger 2005*].

Finally, Gla-proteins are proteins with a γ-carboxyglutamic acid (Gla). Osteocalcin or Bone Gla Protein is the most abundant of all non-collagenous proteins. It is secreted by osteoblasts and studies show that it inhibits the mineralisation process in bone [*Hollinger 2005*].

The exact role of each NCP separately seems to be still under investigation, however, it is believed that they play an essential role on controlling the nucleation and the growth of the mineral phase [*Baht et al. 2008; Hunter and Goldberg 1993*], and they also facilitate attachment between collagens and mineral crystals [*Baht et al. 2008; Tye et al. 2005*].

Finally, other biomolecules like Proteoglycans and Lipids (~2 –4%) are also present within the bone tissue.

2.1.3 The Cells of Bone Tissue

There are three main types of cell found in bone tissue. These are the *Osteoblasts*, the *Osteoclasts* and the *Octeocytes* [*Miller and Jee 1987*]. Briefly, Osteoblasts are mononuclear cells of about 15 –30 μm in length in charge of bone formation. They arise from the differentiation of pluripotent mesenchymal progenitor cells and are located on the surfaces of growing, remodelling or healing bones. The main task of these cells is the synthesis of collagen molecules which are then secreted into the extracellular areas where they cross-link. They also secrete NCPs including osteopontin, osteocalcin, and bone sialoprotein [*Hollinger 2005*] – Ch3]. Figure 2-1 shows a topography image of an Osteoblast (Asylum Research Web-Photo gallery).

Osteoclasts are large cells (about 40 –100 μm in length) which are responsible for desorption of the bone tissue by releasing protons (H^+) and enzymes. As HAP is stable in basic pH (pH >8.5), the local concentration of protons alters the value of pH towards the "acidic" region resulting in dissolution of HAP

crystals. Subsequently the remaining organic matrix is deconstructed by the secreted enzymes.

Osteocytes are the most abundant cells within the bone tissue. They derive from osteoblasts which have been proliferated after their entrapment in the newly formed bone tissue. They lie into cavities, the lamellae, which are interconnected by long canals called *calaniculi*. Through canaliculi osteocytes develop *cytoplasmic processes* to form a cell network throughout the bone matrix (Figure 2-1) which is believed to be crucial for maintaining the bone tissue.

Importantly, both osteoblasts and osteoclasts are actively involved in bone remodelling, and many studies suggest that osteocytes are also involved in this procedure. The term remodelling is used to describe the biological procedure during which new bone is formed on the surface of pre-existing bone tissue. It is a very important process for the healing of bone as well as for its adaptation to mechanical and/or metabolic changes of its environment. Since Wolff's first report [*Wolff 1892*] the remodelling of the bone has been widely studied and it is nowadays believed that a key role on this process is played by osteocytes.

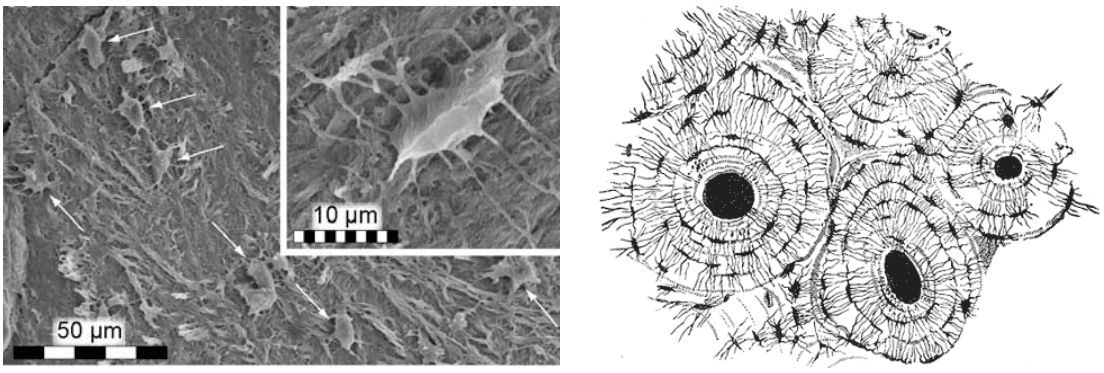

Figure 2-1: (left) Secondary electron micrograph of acid etched cortical bone showing osteoblasts at the bone's surface fibrous tissues and what appears to be part of the osteocyte-lacunocanalicular system (Image courtesy of Johan Lindgren; adapted from Wikimedia Commons; 2012); (right) Schematic representation of bone osteons. The lamellar structure and the developed network of osteocytes are also apparent (Adapted from Wikimedia Commons; 2011).

These cells are sensitive to mechanical changes (mechanosensing cell) and they respond to it by excreting metabolic factors which initiate remodelling. More specifically, low mechanical strains –or more accurately low mechanical stimulus– result in bone resorption while high mechanical stimulus results in new bone formation. It is also speculated that osteocytes contribute to the maintenance of bone tissue by initiating remodelling when fatigue damage occurs [*Hollinger 2005*].

In healthy cortical bone, remodelling can be briefly described as a sequence of three biological procedures. These are *activation*, *resorption* and *formation* (a.k.a. ARF cycle). The first procedure, activation, refers to the activation of the osteoclasts cell which is caused by apoptosis -programmed death- of the osteocytes. The cause of osteocytes' apoptosis is not very well understood but it is believed that it could be triggered by the direct damage of these cells or by the cells' disuse. During the resorption stage, osteoclasts start resorbing the bone matrix at the activation site, creating a channel of a typical diameter of 200 -300 μm. The newly formed canal is then filled with endothelial cells and perivascular mesenchymal cells. Finally, during formation, the mesenchymal cells differentiate into osteoblasts and they start bone deposition. The result of this process is a cylindrical layered structure called *osteon*. Osteons are roughly 200 –300 μm wide and their long axis is oriented parallel to the long axis of the bone [*Rho et al. 1998b; Weiner and Wagner 1998a*].

It is worth noting that bone resorption is closely followed by bone deposition in a manner that the mean bone mass remains unchanged [*Marcus et al. 2009*] – ch1; [*Robling et al. 2006*].

2.1.4 Collagen-Mineral Interaction: Nucleation and Crystallisation Process

The procedure of the physiological mineralisation of the organic matrix of bone has been at the epicentre of bone research since the mid-1960's, but to a large extend remains a mystery. The most well accepted model approaches the mineralisation process as a classical crystal growth procedure, i.e. nucleation → crystal growth → crystal proliferation. According to this model, the apatite crystals nucleate in the "gap" zone of collagen fibrils and grow along the a– and c–crystallographic axis; that is in width and length, forming plate-like

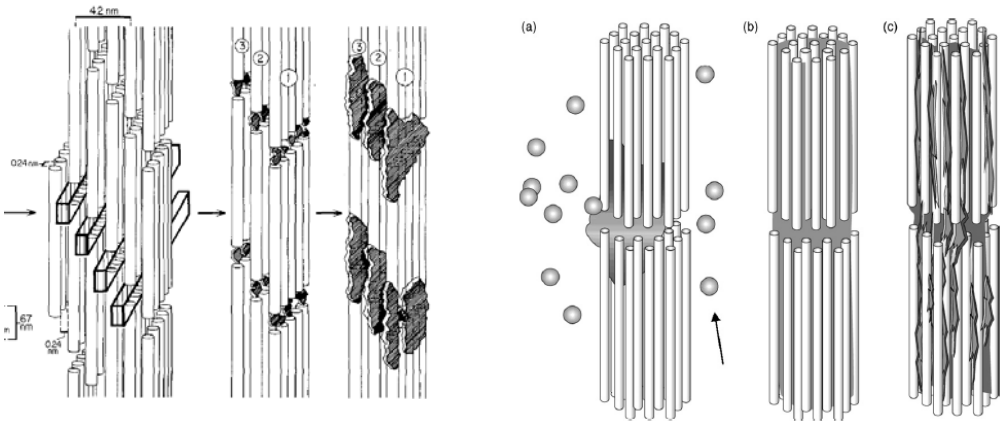

Figure 2-2: Gap-nucleation (left) and PILP precursor (right) models of bone mineralisation; (a) Collagen molecules are assembled spontaneously and stabilized via gross links resulting into the 3D structure. The gap between the collagen molecules seems to be the place that nucleation of the mineral crystals occurs. Finally, these crystals develop along the collagen "template" with their c-axis parallel to the long axis of collagens (adapted from [*Landis et al. 1993b*]). In PILP precursor model, the "nanoscopic droplets" of the hydrated calcium phosphate solution (PILP) phase is imbibed into the collagen fibre and during the water exclusion a solid amorphous precursor phase is formed. Finally, crystallisation of the amorphous calcium phosphate precursor is taking place and the fibre mineralises (Adapted from [*Olszta et al. 2007*]).

crystals (Figure 2-2a) [*Landis et al. 1993a*]. During this process, NCPs are thought to have an important role in both nucleation and crystal shape manipulation due to their calcium-binding ability and their high affinity to collagen [*Eanes 1992; Gray and Standring 2005; Hollinger 2005; Roach 1994a*].

This model has been recently questioned by L. B. Gower and the co-workers on the basis of the mechanism of nucleation of the mineral phase and the role of the NCPs. They counter-propose a model where the intrafibrillar mineralisation occurs via a polymer-induced liquid-precursor (PILP) process according to which a fluidic amorphous precursor phase is imbibed into the collagen fibre by capillary action induced by the highly anionic NCPs and crystallizes upon solidification [*Olszta et al. 2007*].

In addition to the intra-fibrillar mineral deposition Kindt et al. and Thurner et al. showed that the collagen fibrils are also coated with mineral crystals with the

NCPs intermediating between the mineral crystals as well as between the crystals and the collagen molecules (Figure 2-3).

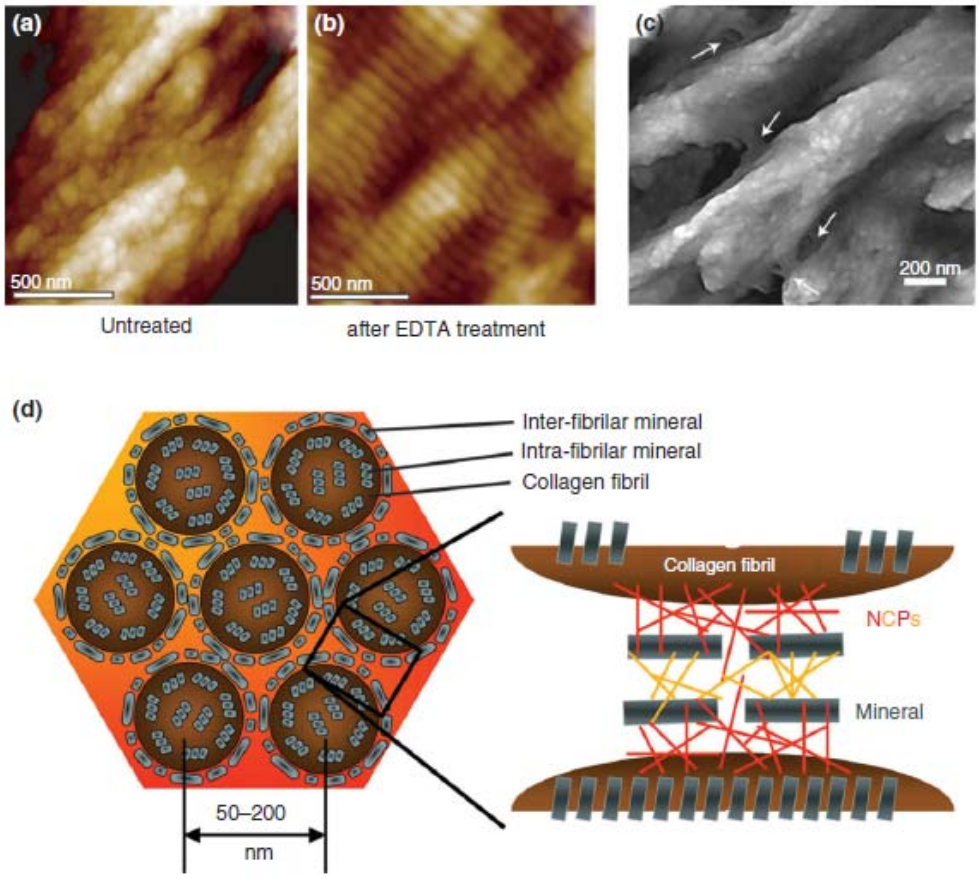

Figure 2-3: AFM (a) and SEM (c) images of fracture surface of trabecular bovine bone (b) after treatment with ethylenediamine tetraacetic acid (EDTA) the CDHA crystals were dissolved and the underling collagen fibre was revealed. (d) The proposed nanoscale model of bone [*Thurner 2009*]

2.1.5 The Hierarchical Organisation of Bone

If collagen fibrils, mineral crystals and NCPs are the main constituents of the mature bone, the mineralised collagen fibre comprises its fundamental structural unit. It is from the organization and the arrangement of this unit that all other –higher– hierarchical levels derive. Figure 2-4 illustrates a schematic bottom–up representation of the hierarchical structure of mature bone. It is important to note, that in this illustration the mineralised collagen fibril (level –

2) is presented according to the "gap-nucleation" model as to date this is the most widely accepted one and not in contradiction to Gower's.

Levels 1, 2 and 3: The hierarchical level 1 refers to the total of the main constituents of bone as described in the previous sections while level 2 refers to the first hierarchically structured entity which is the mineralised collagen fibril. Finally, level 3 corresponds to the bundling of these fibrils along their long axis the result of which is the mineralised collagen fibre [*Weiner and Wagner 1998a*]. In principle, the broad term "bone's nanostructure" which is often used in the literature is referring to these three hierarchical levels.

Level 4: The hierarchical level 4 refers to the organisation of the mineralised collagen fibres into ~3 –7 μm wide "sheets" called *lamellae* which are essentially the building blocks of almost all bone micro- and macro-structures (except woven bone) [*Marotti 1993; Rho et al. 1998b*]. Level 4 organisation is also sometimes called the "sub-osteonal" structure or "sub-microstructure".

Level 5: Osteonal (or micro-) structure of bone; the bone lamellae of level 4 further arrange around blood vessels in a concentric fashion forming a structure called osteon. Osteons are the most complex structure of bone tissue and they are the result of the remodelling process of the bone (cf. §2.1.3). [*Rho et al. 1998b; Weiner and Wagner 1998a*].

Level 6 and 7: In level 6 we find the two major types of bone tissue. That is the cortical (or Compact) and the trabecular (or cancellous) bone. As their name implies, the two types differ in density as a result of the different structure. Cortical bone is a highly dense bone tissue, consisting of osteons and some areas of lamellar bone (lamellae lay parallel instead of in concentric fashion). Trabecular bone is highly porous and in contrast to cortical bone, it lacks micro-structural features like osteons. Instead, it consists of parallel developed

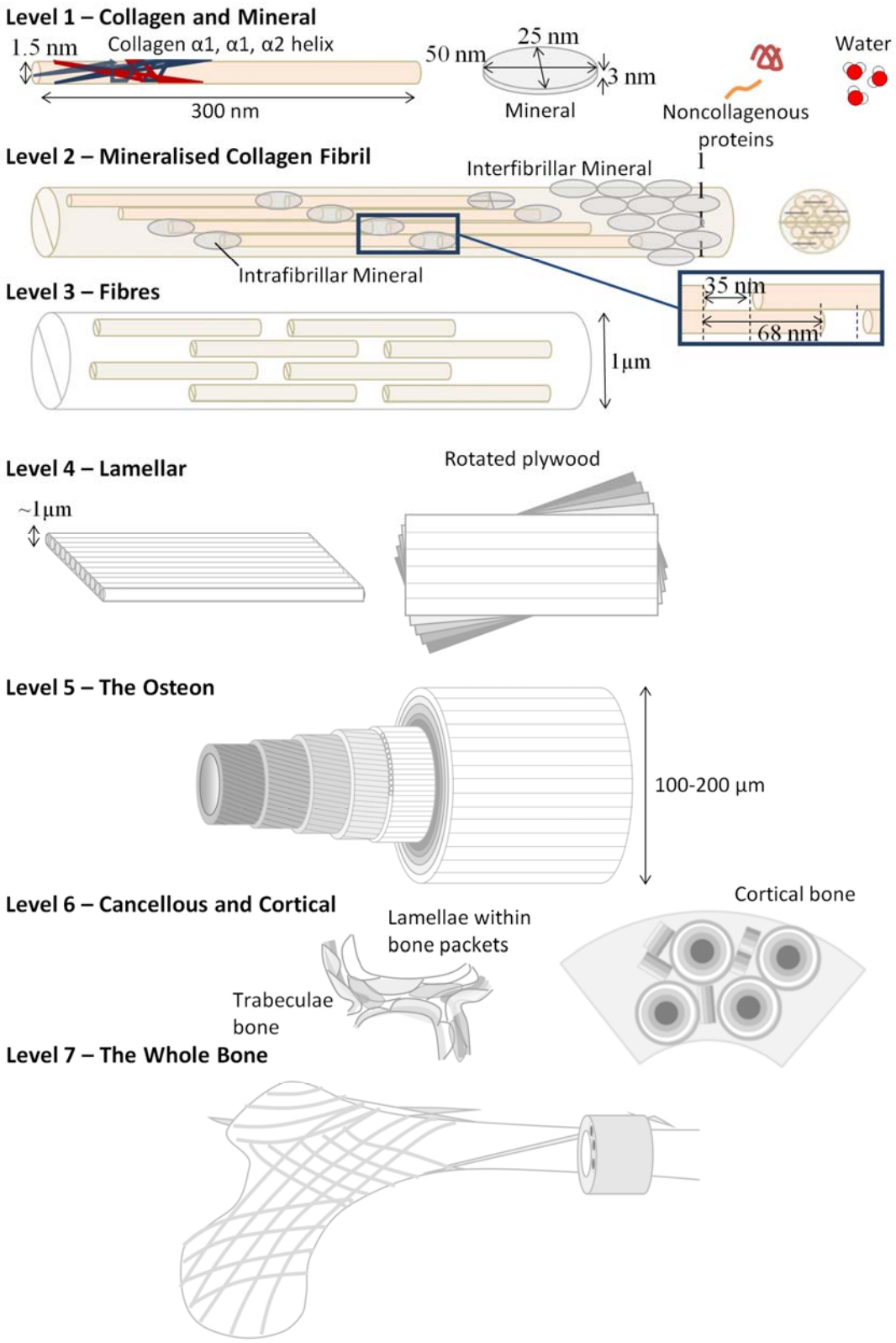

Figure 2-4: A bottom-up illustration of the hierarchical organization of bone (picture courtesy of T. Jenkins).

lamellae aligned with the orientation of the trabeculae [*Rho et al. 1998b; Weiner and Wagner 1998a*]. Level 7 is referred to the whole bone geometry and it is also called tissue-level. A more detailed description of all levels of organisation is given in the next paragraphs.

2.1.5.1 Level 7: The tissue level

Level 7 is referring to the "whole bones" of the skeleton which are divided into four broad categories according to their shape; these are (i) *flat bones*, like for example the bones of the scull, the scapula or the sternum; (ii) *short bones*, like the carpus and the tarsus; (iii) *long bones*, e.g. the femur and the tibia; and (iv) *irregular bones* which include all the rest which cannot be grouped under the forenamed categories. Examples of irregular bones are the vertebrae, the hyoid, etc. [*Gray and Standring 2005*].

The bones of all four categories mentioned above comprised of a porous core (trabecular or cortical bone) enclosed into a shell of dense bone (cortical or compact bone). The thickness of the cortical bone as well as the volumetric cortical/trabecular bone ratio varies among the various categories and it depends upon the biomechanical and anatomical role of each bone. For example, bones which have to regularly withstand high loads, like the femur, develop a thick cortical part while others made to facilitate muscular attachment, like scapula, develop into flat bones. In this case the trabecular tissue is covered by a thin cortical shell [*Gray and Standring 2005*].

As the present study is mainly focused on the micro- and nanomechanical properties of the cortical bone and more specifically the cortical bone derived from the midshaft of the femur, only the long bones will be discussed in more detail.

The characteristic shape of the adult long bone is dominated by two macroscopic anatomical features. (a) The cylinder like shape of the main body that widens gradually towards both edges called diaphysis (from the Greek "δια" (dia) meaning between and "φύσης" (physis) meaning growth | diaphysis =something that grows between..) and (b) the rounded extremities of both ends called *epiphyses* ("επί" (epi) =on the top). The area where the diaphysis widens to meet epiphysis is consider as separate anatomical feature and called *metaphysis* ("μετά" (meta) =after). Splitting a long bone sagittally or coronally

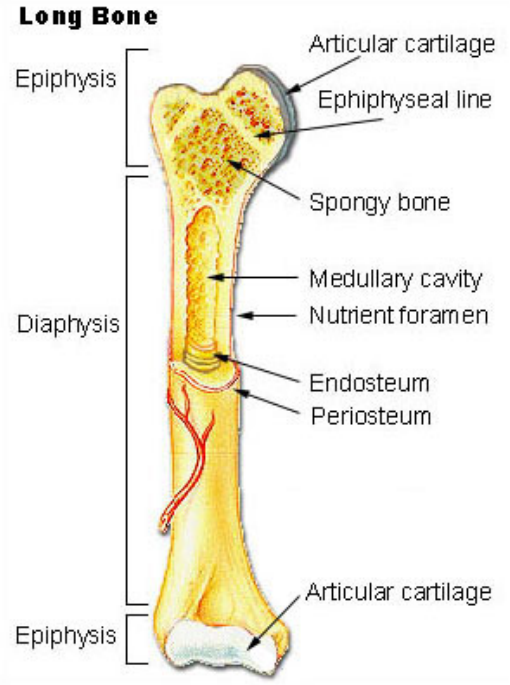

Figure 2-5: Schematic diagram of a long bone (Adapted from Wikimedia Commons; 2012).

the internal cavity where the red (haemopoietic) bone marrow is located can be exposed [*Gray and Standring 2005*] and the cortical and the trabecular bone can be revealed. The shell around the bone marrow is comprised of compact lamellar bone, while moving towards the epiphyses the highly porous structured cancellous (or trabecular) bone appears in the inner area of the bone (Figure 2-5).

2.1.5.2 Level 6: Woven, cortical and compact bone

woven bone

Woven bone can be considered as the pre-mature bone. This type of bone occurs during the very first stage of life. The skeleton of the human infants for example is made of woven bone which is gradually replaced with lamellar and osteonal bone by the age of ~2 -3 years. Woven bone is also the type of bone that initially forms in fractured areas after severe injuries. Its main difference to lamellar -bone is that woven bone is less organized and lacks the characteristic orientation of collagen fibrils of the lamellar structures [*Gray and Standring 2005*].

cancellous (or trabecular) bone

The cancellous (or trabecular) bone tissue consists of rod- and plate-like segments called single trabeculae which are interconnected to form a dense porous network (Figure 2-6) [Rho et al. 1998b]. Its porosity helps the weight of the bone to be kept low while at the same time redistributes the applied stresses along the cortical bone shell [*Keaveny et al. 2001*]. The highly porous structure results in a high surface-to-volume ratio resulting in a proportionally higher level of remodelling in comparison to the more dense (1.87 g/cc vs 1.91 g/cc) cortical bone [*Cowin and Telega 2003*]. Consequently, cancellous bone is overall "younger" than the cortical tissue.

In contrast to cortical bone, cancellous bone lacks micro-structural features like osteons. Instead, it consists of parallel developed lamellae aligned along the orientation of the trabeculae. These segments, called trabecular packets, are separated by cement lines and are the building blocks of trabecular bone. Table 2-2 presents the main compositional differences between cancellous and cortical bone tissue.

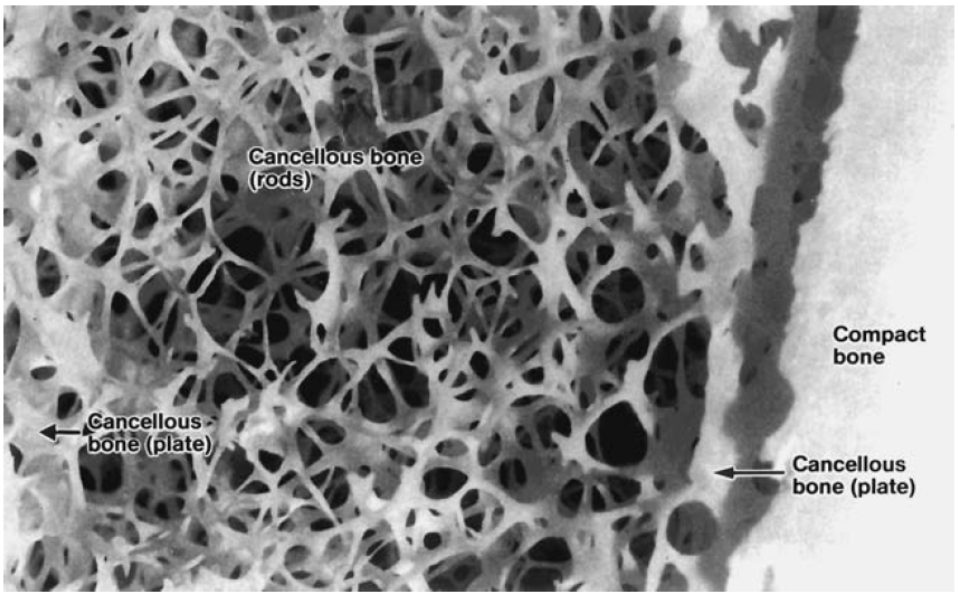

Figure 2-6: Segment of human tibia. Cortical or compact bone (far right) and trabecular or cancellous bone (left). Interconnected trabeculae network of rod-rod, rod-plate and plate-plate formations is also noted on the image. Picture scale 4x (Adapted from [*Cowin and Telega 2003*])

Table 2-2: Compositions of Cancellous and Cortical Bone Tissue [*Cowin and Telega 2003*]

Properties	Cancellous Tissue	Cortical Tissue
Calcium content (mg/g)	257.0	271 (bovine)
Calcium (% of ash weight)	34.4	38.5 (human)
Phosphorus content (% of ash weight)	18.1	17.9 (human)
Water (% volume)	27.0	22.9 (human)
Tissue density (g/cc)	1.87	1.91 (human)
Mineralisation (gray scale/mm^2)	0.34	0.29 (human)

cortical (or compact) bone

Cortical or compact bone is a highly dense bone tissue, comprising the outer shell of all bones as well as the diaphysis of the long bones where no trabecular core exists. It supplies bone with rigidity and strength required for the locomotion and protection of the body.

It consists of parallel and concentric lamellae embedded in a "matrix" of less organised interstitial bone. The concentric arrangement of the lamellae results in a complex structure called osteon. The outer layer of the osteon is a less-organized and collagen-deficient interfacial lamella called cement line with typical dimensions of 0.5 –2 μm [*Cowin and Telega 2003*][2]. Osteons are considered distinct hierarchical levels per-se and as such they are discussed separately in §0.

Parallel, non-concentric lamellar areas are also present in cortical bone. This arrangement is called plexiform of lamellar bone and it is of great importance in the fast growing bones as can be deposited in a much faster rate than osteonal bone [*Cowin and Telega 2003*][3]. An overview of the structure of long bones is given in Figure 2-7.

Cortical bone, like many natural materials, exhibits anisotropic mechanical behaviour [*Reilly and Burstein 1974*] meaning that the mechanical properties of cortical bone differ from one orthogonal direction to another. This anisotropy

[2] Chapter 10-4

[3] Chapter 19-2

originates from its hierarchical structure but also from the orientation of its micro- and nano-features; e.g. osteons, collagen fibrils and mineral crystal. Rho et al. [*Rho 1996*] and [*Franzoso and Zysset 2009*] independently of each other observed that, for the tree orthogonal directions, the anisotropy in elastic modulus (E) of cortical bone governed by the following relationship:

$$E_{longtitudinal} > E_{circumferential} > E_{radial}$$

Indicative values of bone's anisotropy as measured by Rho et al. by means of ultrasonic technique are presented in Table 2-3.

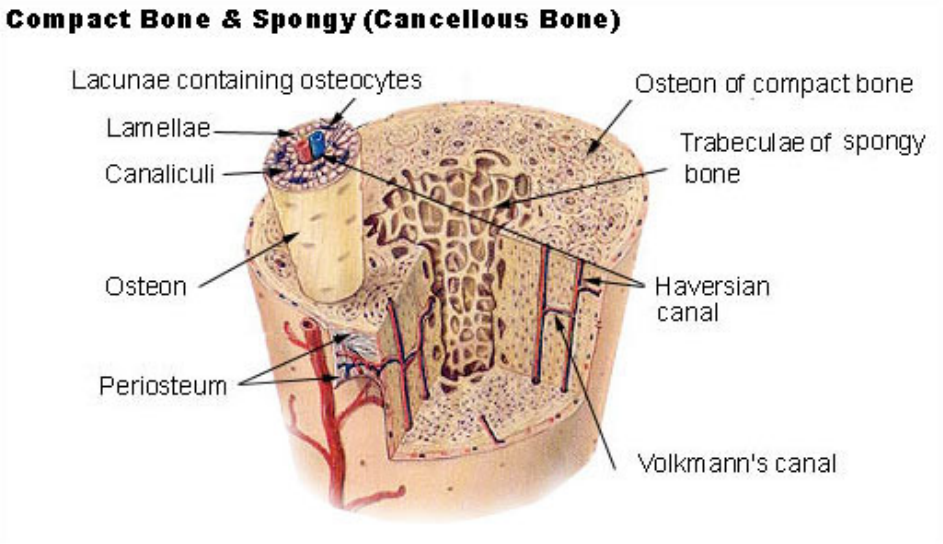

Figure 2-7: Schematic representation of the hierarchical features of long bones. From the periphery to the centre: periosteum (soft vascular tissue), lamellar area (outer region of compact bone comprised mainly of circumferentially developed lamellae), osteonal compact bone (inner region of compact bone comprised mainly of secondary osteons) and trabecular or porous bone. A single osteon along with the blood vessels, the nerves and the osteocytes located within it is called Haversian system and is the fundamental structural and biological unit of compact bone. Throughout the whole matrix of compact bone osteocytes are interconnected via tiny canals called calaniculi (adapted from Wikimedia Commons; 2012).

Table 2-3: Elastic moduli, shear moduli and Poisson's ratios of human tibia cortical bone. The main orthogonal directions are indicated by numbers as following 1: radial; 2: circumferential; 3:longditudinal [*Rho 1996*].

E_1 (GPa)	11.7 ± 1.3	G_{12} (GPa)	4.10 ± 0.5	ν_{12}	0.420 ± 0.074
E_2 (GPa)	12.2 ± 1.4	G_{13} (GPa)	5.17 ± 0.6	ν_{13}	0.237 ± 0.041
E_3 (GPa)	20.7 ± 1.9	G_{23} (GPa)	5.70 ± 0.5	ν_{23}	0.231 ± 0.035
				ν_{21}	0.435 ± 0.057
				ν_{31}	0.417 ± 0.048
				ν_{32}	0.390 ± 0.021

2.1.5.3 Level 5: The osteon

The osteon is the most complex structure of the mammalian bone and as such it is considered a separate hierarchical level. Osteons are laminate tubular structures oriented with their long axis parallel to the long axis of the bone. Their characteristic structure is the result of concentric arrangement of single lamellae developed around a blood vessel [*Fratzl and Weinkamer 2007*]. Each osteonal lamellae consists of sub-layers of mineralised fibres which rotate to an angle from roughly 10° to 60° in respect to osteon long axis [*Wagermaier et al. 2006*]. The outermost layer of the osteon is a ~2 μm thick zone which separates the osteon form the interstitial bone and is called cement line [*Cowin 2001*]. Similar boundary layers of ~1 -2 μm wide lay between subsequent lamellae [*Ziv et al. 1996*] which from now on will be referred as interlamellar areas. These three osteonal features will be discussed in more detail in §2.1.5.4.

Ascenzi et al. classified the osteons on three different types, type-I, type-II and type-III, based on their appearance under the polarised light microscope (PLM). Characteristic examples of each type are illustrated in Figure 2-8. The different appearance was attributed to the different birefringence pattern resulting from the differences of the principle fibre orientation of the successive lamellae (Figure 2-8:bottom) [*Ascenzi and Bonucci 1968; Martin et al. 1996*]. Between 1964 -1994 Ascenzi's group published a series of experimental studies on the mechanical characterisation of single osteons.

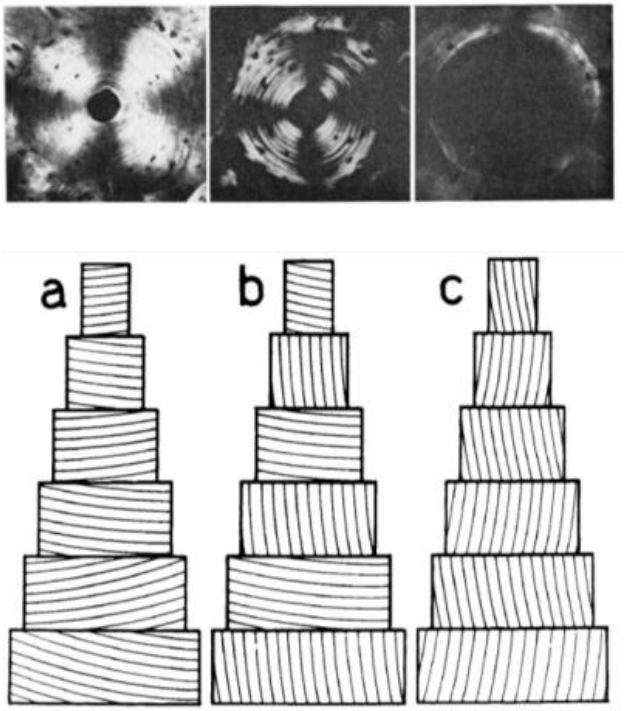

Figure 2-8: PLM images of the three different osteon types (top) and schematic representation of the principle fibre orientation of lamellae (top). (a): osteons of type-I, (b): type-II and (c) type-III (Adapted from [*Ascenzi and Bonucci 1968*]).

In these studies, they managed to isolate single osteons of various types and test them in tension, compression, shear, bending and torsion. They reported that, as the result of the different principle fibre orientation on their lamellae, each osteon type is better adapted for different types of loading conditions. That is, osteons of type I effectively resist compression and shear, type II perform optimally against tension and torsion while type III being a "mixture" of I and II performs better against complex loading conditions like bending [*Ascenzi et al. 1990*, *1994; Ascenzi and Benvenuti 1986; Ascenzi et al. 1982; Ascenzi and Bonucci 1964*, *1967*, *1968*, *1972*]. It is worth noting that so far these are the only studies on the mechanical characterisation of isolated osteons.

From the biomechanical point of view, osteons have a critical contribution on the ultimate fracture resistance of the cortical bone. The osteons, being laminated fibre-composite structures, act as crack deflectors increasing the length of the crack path and consequently the required energy-to-fracture [*Ritchie et al. 2005*].

2.1.5.4 Level 4: The osteonal structure

single lamellae

As mentioned in §2.1.5 the mineralised collagen fibres arrange into ~ 3 –7 μm wide "sheets" called lamellae. These which are essentially the building block of almost all bone micro- and macro- structures, including osteons and trabecular packages but not woven bone [*Marotti 1993; Rho et al. 1998b*].

The common perception of lamellae is this of the "twisted plywood" as described in the historical paper of Giraud-Guille. That is, each lamella consists of parallel arranged mineralised fibres organized in five sub-layers, each one of which gradually rotates "by a small and constant angle" in respect to the previous one [*Giraud-Guille 1988; Weiner et al. 1999*]. This structure is represented schematically in the drawing of Figure 2-9.

However, the current acceptable model for the lamella considers that there is an overall parallel orientation of collagen fibres but the final structure consists of interlaced collagen macromolecules forming a "spaghetti-like" bulk within lamellae [*Rho et al. 1998a*].

It is worth noting, though, that another, less popular, model argues that there is no preferential orientation of the collagen fibres within single lamellae [*Marotti 1993*]. To date, the actual structure of the single lamella is a mater of ongoing debate [*Rho et al. 1998b*].

interlamellar areas

The interlamellar areas are thin boundary layers separating two subsequent lamellae [*Ziv et al. 1996*]. These regions are often called "thin", "dense" or "transverse" lamellae [*Marotti 1993; Reid 1986*] but the term interlamellar areas is preferred here to emphasise their structural and compositional difference compared to osteonal lamellae.

It is interesting that although the contribution on the interlamellar areas to the fracture behaviour of bone has been recognised; it has been noted for example that cracks tend to deflect on interlamellar areas [*Hiller et al. 2006; Peterlik et al. 2005; Weiner and Wagner 1998a*], only a limited number of studies focusing on the characterisation of these areas have been published.

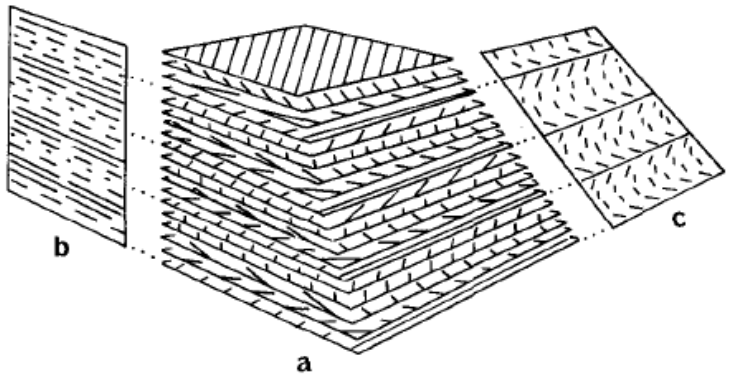

Figure 2-9: Representation of "twisted plywood" structure as proposed by Giraud-Guille. Each sheet represents a lamella while the parallel lines show the orientation of collagen fibres (Adapted from [*Giraud-Guille 1988*]).

An early study on interlamellar areas by Ascenzi and Benvenuti [*Ascenzi and Benvenuti 1986*] reported on a criss-crossed collagen fibril arrangement while Reid, referred to them as transverse lamellae, reported that they consist of fibres running circumferentially to the osteon's long axis [*Reid 1986*]. Weiner and Traub also payed attention to the interlamellar areas (or according to their terminology lamellar boundaries) and confirmed once again the circumferential arrangement of the collagen fibres in these areas [*Weiner and Traub 1992*]. Ten years after Ascenzi and Benvenuti's paper, Ziv et al. also found that interlamellar areas comprised of fibres laying more or less perpendicularly to the long axis of the bone but they further proposed that lamellae and interlamellar areas may not be separate structures. Instead, both features could be part of a single deposition cycle with interlamellar areas being the transitional zone from the one lamellae to the next [*Ziv et al. 1996*]. In contrast, Pazzaglia et al. in their resent study published in 2012 describe the interlamellar areas as "superficial grooves" [*Pazzaglia et al. 2012*]. Regardless of the ambiguity regarding the definition of the interlamellar areas all the forenamed studies agree that these features separate subsequent lamellae and consist of circumferentially aligned collagen fibres (Figure 2-10).

The composition of the interlamellar areas is another not-very well studied subject. The main reason is again that for many years these features have not attracted the interest of the bone research community. On top of that, their

small size (1 -2 μm wide) made the compositional analysis a challenging task. Nevertheless, a few studies that have achieved compositional characterisation of these areas report that they appear to be rich in non-collagenous proteins [*Derkx et al. 1998*] while observations made based on SEM images suggested that they exhibit lower density of collagen fibres in comparison to lamellae [*Pazzaglia et al. 2012*].

cement lines

The outer layer of the osteon is 1 -5 μm wide structure called a cement line and it is the feature that separates the osteon from the interstitial bone. Cement lines have similar collagen structure with interlamellar areas except that they are wider and in some cases more irregularly shaped [*Pazzaglia et al. 2012*]. Compared to lamellae, they also appear to be collagen-deficient and less mineralised [*Burr et al. 1988; Schaffler et al. 1987*] but the latter was recently questioned by Skedros and co-workers who find them to be highly mineralised [*Skedros et al. 2011*]. Finally, from the mechanical view point, cement lines are weaker than the rest of the osteonal features making them a preferential crack propagation path [*Dong et al. 2005*] [*Bigley et al. 2006*] [*Ager et al. 2006; Nalla et al. 2004; Ritchie et al. 2005*].

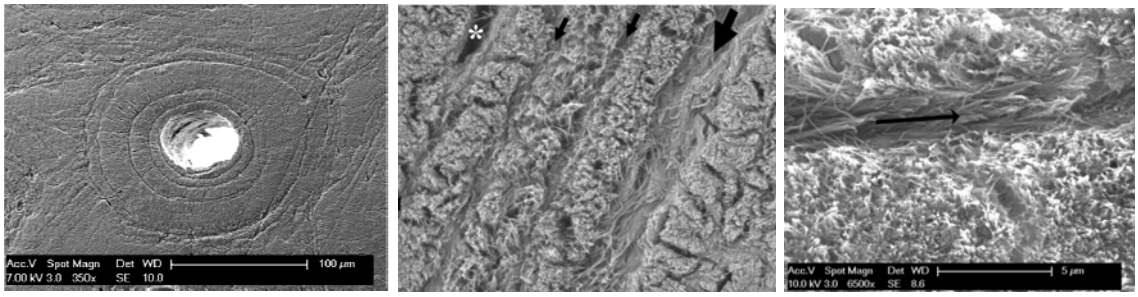

Figure 2-10: (left) SEM image of a Na_3PO_4 etched osteon; (middle) SEM image of the lamination structure of a chemically etched osteon. Thin arrows pointing onto the interlamellar areas while the thick one on the cement line. An osteocyte lacuna is also evident at the top left corner (white star); (right) Higher magnification of an interlamellar area. Note that the collagen fibres lie parallel to the page in contrast to the "standing" fibres of lamellae. (Adapted from [*Pazzaglia et al. 2012*])

2.1.5.5 Level 3: Long bone nanostructure

As discussed earlier, macro- and microscopic features of bone are all built from hierarchically arranged collagen fibrils filled and coated with the inorganic (mineral) phase of bone. These fibrils are molecular collagen macromolecules with a diameter of ~50 –250 nm which can be packed together to form a fibre of a few micrometers which are then further arranged in lamellae [*Thurner 2009*].

Molecular collagen and collagen fibrils

Collagen is a protein comprised of three polypeptide chains, also referred to as α-chains, in the structure of right hand triple-helix. Each α-chain is a macromolecule of the form $(Gly\text{-}X\text{-}Y)_n$; where usually $337< n <343$. Gly-X-Y refers to the peptide Glycine[4]-X-Y (*Gly-X-Y*) where *X* and *Y* can be any amino acid.

Figure 2-11 depicts the triple helix structure of a collagen molecule. This conformation is able to produce a number of different molecules, which all fall into the collagen superfamily. From all these proteins only the so-called fibrillar ones are of interest for this study. These are collagen conformations composed by molecules with typical dimensions of 300 nm long and ~ 1.5 nm wide. It is these supermolecules that when inspected under the various microscopic techniques exhibit the characteristic 64 -67 nm repeating banding (D-periodicity or D-banding); Figure 2-12:top.

Fibrillar collagen is the product of spontaneous assembly of collagen molecules which are then stabilized via cross-links [*Fratzl 2008b*]. In Figure 2-12 a 2D representation of this conformation and an AFM image of a collagen fibril are illustrated.

The biosynthesis of collagen starts intracellularly in the rough endoplasmic reticulum where the so called procollagen molecules are synthesised. These are soluble collagen molecules with N- and C-terminal domains which will be then removed by specific proteinases in the extracellular space. The secreted

[4] NH_2CH_2COOH

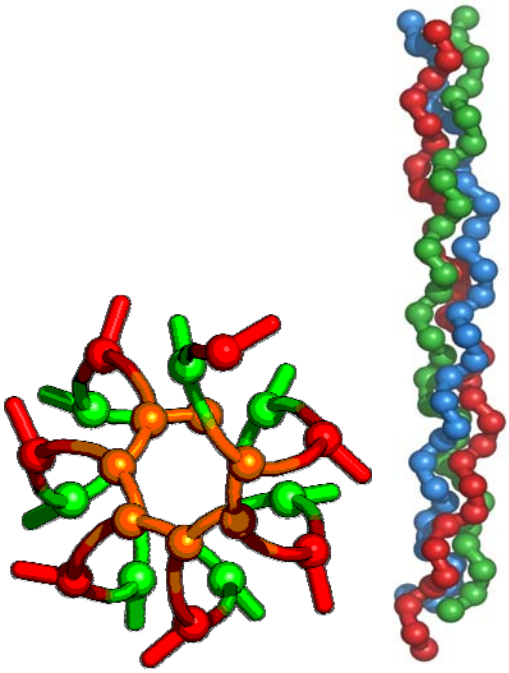

Figure 2-11: Top to bottom (left) and space-filling side (right) view of molecular collagen. α-Chains are denoted with different colours while the Gly-X-Y sequence is only presented at the bottom side view as differently coloured domains (orange, red, green). Note that as Gly molecule (left: orange domain) should always be in the "core" of the macromolecule the resulted structure is a right-handed helical twist (Adapted from Wikimedia commons).

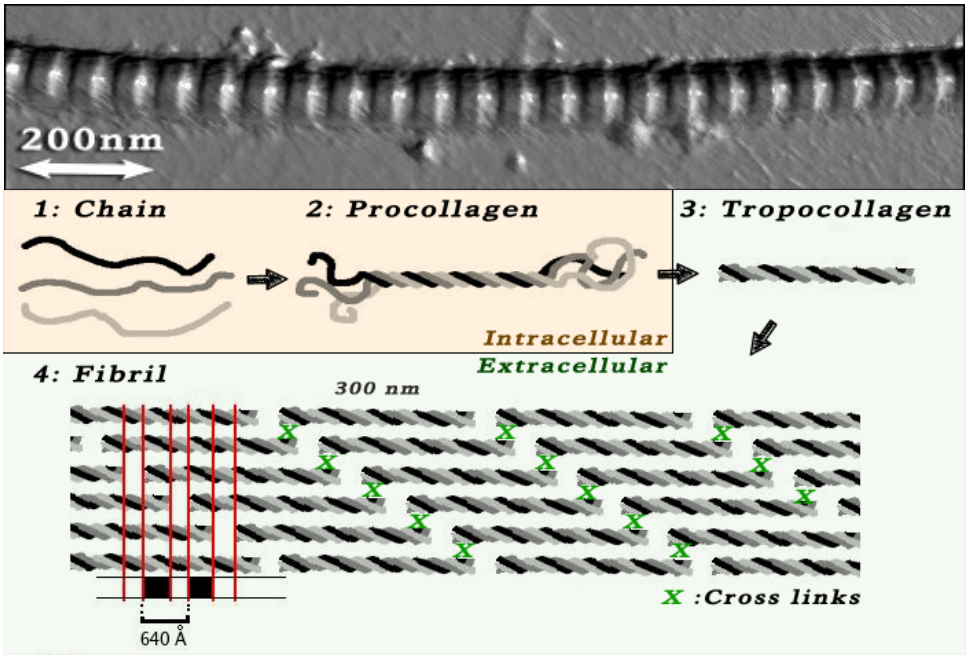

Figure 2-12: (top) High resolution AFM height image of rat tail tendon collagen fibre (O. Andriotis – 2011). (bottom) Assembly of fibrillar collagen molecules into a fibril [*Fratzl 2008b*]. The intramolecular pounds (cross-link) are noted schematically here with green "x"s. (Adapted from Wikimedia commons and edited)

collagen molecules will then self-assemble into fibrils and stabilised via cross-links [*Fratzl 2008b*]. This procedure is schematically represented in Figure 2-12.

2.1.6 Bone Micro- and Nanomechanical Properties

Here, with the term "nanomechanical properties" I refer to the mechanical properties of the individual sub-osteonal features or the fundamental component that build up bone.

Because of the highly complex hierarchical structure of bone tissue –more than five (5) hierarchical levels [*Fratzl and Weinkamer 2007*] –, its final fracture toughness strongly depends on the toughness that bone exhibits on each individual hierarchical level [*Fratzl 2008a*]. Consequently, understanding bone's toughness, presupposes the understanding of the mechanical properties –and behaviour– of its fundamental building blocks. In this context, researchers have pushed the mechanical testing to the limits, scaling down their experimental set-ups in order to study the mechanical properties of these building blocks.

As early as 1964, Ascenzi *et al.* isolates single osteons and tests them under tension [*Ascenzi and Bonucci 1972*] by means of microwave extensometer, based on cavity and pulse technique. That was the beginning of a whole series of studies in which they tested single osteons in tension [*Ascenzi and Bonucci 1964*, *1967*], compression [*Ascenzi and Bonucci 1968*], bending [*Ascenzi et al. 1990*], shear [*Ascenzi and Bonucci 1972*] and torsion [*Ascenzi et al. 1994*]. In all cases, the measured mechanical properties were significantly different among osteons with different collagen fibre orientation. Based on the birefringence of each osteon under a Polarised Light Microscope (PLM), they show that osteons with collagen fibres predominantly oriented longitudinally to the osteon's long axis, are more resistant to torsional failure and they exhibit greater elastic modulus and ultimate strength under tension than the ones with transversely oriented fibres. The opposite behaviour was evident for compression, where transversely oriented collagen fibres appear stronger and stiffer. These osteons were also better in withstanding bending and shear stresses, but the shearing strength of all different types of osteons –regardless fibre orientation– was considerably lower that the compressive and tensile strength.

Their studies established that even the osteons, *i.e.* the cortical bone's basic structural unit (BSU), should be considered as a complex structure which its material properties rely upon the properties and the arrangement of the sub-osteonal features.

Going a step further, they also tried to measure the mechanical properties under tension of a single osteonic lamella, which is the basic structural unit of the osteon. In their paper, they are reporting that, under tension, lamellae behaviour show similarities to these of osteons but technical difficulties did not allow the direct approximation of the measured strength and elastic modulus due to high degree of variability [*Ascenzi et al. 1982*]. Nevertheless, this was the first reported attempt to look deeper into the sub-osteonal features of cortical bone tissue, in order to understand how each one of them is contributing to the global mechanical response of bone tissue.

This past decade numerous studies have dealt with bone's mechanical characterisation in the nano-scale mainly by means of nanoindentation (both conventional and cantilever-based). A representative example of the interest that bone research community shows on studying bone's nanomechanical properties can be seen from Table 2-4 and Figure 2-13. There, the analysis of the search results returned using the criteria "Topic =(nanoindentation) AND Topic =(bone)" in the *Web of Knowledge*[5] website in October, 2012 are presented. The rapid increase in both published items and citations is a clear indicator of this trend.

Hengsberger *et al.* used conventional "nanoindentation" to investigate the differences between individual sub-osteonal features in wet and dry conditions. They reported a significantly different indentation modulus between two distinct sub-osteonal features. What they called "thick" lamellae exhibited higher modulus in comparison to the "thin" ones and they ascribe this to different collagen orientation and mineral content. Interestingly, they show that despite the increment in both "thin" and "thick" lamellae modulus induced by drying, the comparative trends were not affected [*Hengsberger et al. 2002*].

[5] http://apps.webofknowledge.com

Table 2-4: Analysis of search results returned using the criteria "Topic=(nanoindentation) AND Topic=(bone)" [Web of Knowledge; October, 2012].

Results found:	**724**
Sum of the Times Cited:	10398
Sum of Times Cited without self-citations:	7455
Citing Articles:	5746
Citing Articles without self-citations:	5260
Average Citations per Item:	14.36
h-index:	50

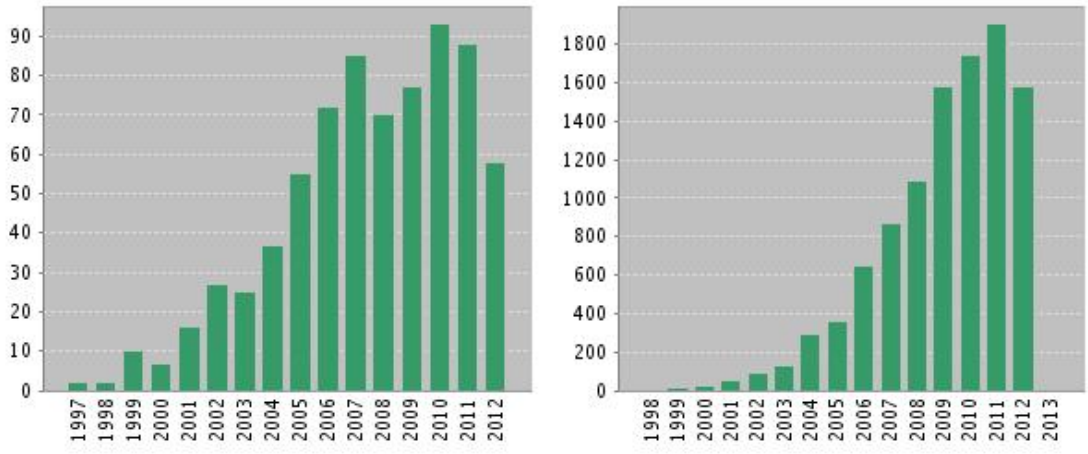

Figure 2-13: Analysis of search results returned using the criteria "Topic=(nanoindentation) AND Topic=(bone)" [Web of Knowledge; October, 2012]; (left) published items in each year; (right) citations in each year

Similar differences between "thin" and "thick" lamella moduli were also reported by Xu *et al.* although this difference found to associate with the roughness of the surface [*Xu et al. 2003*]. X-ray microanalysis of the osteonal samples revealed no significant difference in the composition of these areas with respect to calcium and phosphorus ion concentrations.

Rho *et al*. investigated the "variations in the individual thick lamellar properties within osteons" by conventional "nanoindentation" to assess potential differences among lamellae located closer to Haversian canal and the outermost ones. Their results show gradient reduction of the values of elastic modulus and

hardness, when moving from the Haversian canal to the periphery of the osteon [*Rho et al. 1999*].

The first 2D graphical representation showing the modulation of the Reduced Modulus (E_r) within a single osteon was reported by Gupta *et al.* [*Gupta et al. 2006a*]. For this purpose, they used conventional "nanoindentation" mapping with a spatial resolution of ~1 μm in an observation window of 100 x 100 μm. The derived 2D map exhibited a laminated modulation of the E_r and it was directly comparable to the scanning electron microscopy images from the same area. In contrast with Xu *et al.* though, using back scattering electron imaging in the same indentation window they report mineral composition modulation, similar to that of Reduced Modulus and Stiffness. Thus, they speculate that the measured mechanical modulation is the result of both structural, *i.e.* orientation of collagen fibrils, and compositional variations between these areas.

The same year, Hofmann *et al.*, publish their study in which they combined acoustic microscopy, Raman spectroscopy and conventional "nanoindentation" to assess the composition and elastic properties of osteonal lamellae [*Hofmann et al. 2006*]. They also report significant difference of the elastic moduli of "thin" and "thick" lamellae, but this was not correlated with differences of the degree of mineralisation. It was attributed to the orientation of the collagen fibrils instead. It is worth noting that this was the first time where acoustic microscopy was used to study the structural and mechanical properties of bone in the sub-osteonal level.

Cantilever-based nanoindentation was, also, recently employed to study bone nanomechanical properties on an even smaller scale. This technique used the AFM tip for both imaging and indentation of the sample, allowing for even higher spatial resolution, which could resolve variations at the single-collagen-fibre level. In their study, Tai *et al.* propose a new energy-dissipation mechanism based on the variations they show in the distribution of the elastic modulus. By feeding the indentation results into a finite element model, they demonstrate that this variation results in an increment of the inelastically deformed area when the tissue is under load. As a consequence, during tissue loading, a higher amount of energy is dissipated [*Tai et al. 2007*].

Using cantilever based nanoindentation and AFM in AC imaging mode (they refer to this as "Dynamic Nanoindentation"), Minary-Jolandan and Yu, reveal

similar elastic variations between the gap and overlap regions of Type I collagen fibrils in partially demineralised bone samples [*Minary-Jolandan and Yu 2009*]. The mechanical properties of single collagen fibres forming bone tissue were also studied by Hang and Barber [*Hang and Barber 2011*]. This time the AFM cantilever was used as "load cell" to record Load – Displacement curves of single mineralised collagen fibres under uniaxial tension. They indentify two distinct loading behaviours during single collagen fibre loading which they assign to different mineral content.

Finally, "breaking" further down bone's nanomechanical behaviour, recent studies characterised the behaviour of single demineralised collagen fibres [*Balooch et al. 2008*], single apatitic crystals [*Viswanath et al. 2007*] and films of non-colagenous proteins [*Adams et al. 2008; Fantner et al. 2007; Fantner et al. 2005a; Zappone et al. 2008*].

2.2 Risk of Fracture and Osteoporosis

2.2.1 Bone Strength and Bone Toughness

Before set off analysing the various factors that influence bone strength, and the contribution of each one of them to it, it is necessary to first define the term "strength" from the engineering point of view. Strength is used very often in every day life to describe various material properties but from the mechanical / biomechanical point of view *strength* is a very well defined property which describes the "resistance to permanent (plastic) deformation". As such, it is defined either at the maximum load of the elastic region, i.e. yield strength or at the maximum load of the plastic region, i.e. ultimate strength. In brittle materials though, where there is practically no plastic deformation the measured strength is mainly a function of the pre-existing damage distribution. Thus, the measured "strength" cannot characterise the *resistance to fracture* if the distribution of the pre-existing damage is not known. Given that in most cases this distribution cannot be found, the "worst case scenario" approach is adopted. In this case, a sharp pre-crack is introduced to the samples in order to focus the stress concentration onto a known area. Then, the required stress intensity or energy to fracture can be measured independently to the unknown distribution of the pre-existed damage [*Ritchie et al. 2008*].

Cortical bone is a brittle solid capable of deforming only about 0.5 –3.5 % its initial length before failure. As such, for the reasons mentioned earlier, the bone's strength is highly dependant upon the pre-existent damage, micro-crack defects and crack propagation mechanisms [*Bonfield 1987; Ritchie et al. 2008*]. This is also the reason why, when it comes to bone strength measurements, the characterisation is done in terms of *fracture toughness* (amount of consumed energy to fracture) or *crack growth toughness* (amount of consumed to propagate a crack) [*Bonfield 1987; Ritchie et al. 2008; Zioupos and Currey 1998b*].

The *resistance to fracture* or *fracture toughness* is probably the most clinically important mechanical property of bone, due to its direct correlation with osteoporosis. It is not until recently (2008) that a reference tutorial on this topic was published by Ritchie *et al.* who analysed and compared the various techniques used in the past to evaluate bone's toughness. In their study, the calculation of mammalian bone's fracture toughness was estimated by means of both linear elastic fracture mechanics (LEFM) fracture toughness (K_c) and non-linear elastic fracture mechanics (nLEFM) fracture toughness (J_c). Crack growth toughness is also evaluated by means of the crack resistance curve (R-curve). The latter is a very useful parameter when stable crack growth occurs prior to fracture. In such a case, not only the value of the fracture toughness of the material is of interest but also the way the material resists (toughens) against the propagation of the stable crack [*Ritchie et al. 2008*].

Bone, besides being a brittle material, often exhibits stable crack growth due to the various extrinsic toughening mechanisms which are acting during bone failure. These include among others (i) deflection and twisting of cracks on the microstructural features i.e. osteons, cement lines, etc; (ii) collagen-mediated bridging of the developed crack; (iii) uncracked ligaments and (iv) defuse damage formation [*Launey et al. 2010; Ritchie et al. 2008; Ritchie et al. 2009*]. Thus, the crack growth toughness analysis can provide valuable information regarding these mechanisms and should also be taken into account when one evaluates bone's toughness.

As a complex composite material, bone's mechanical properties derive from the contribution of each one of its fundamental component (collagen, mineral, NCPs) and the nano- and micro-structures that these components form (osteons, lamellae, rod or plate like trabeculae, etc). Weiner and Wagner

outlined 7 hierarchical organisation levels in bone, each one of which contributes to the final mechanical properties of the tissue [*Weiner and Wagner 1998b*]. These levels have been presented in Figure 2-4 and a detailed presentation has already been given in the previous chapters. From the mechanical point of view, it is noteworthy that in contrast to many materials where low toughness is usually related with high elastic modulus, the mechanical dissimilarity of the fundamental constituents of bone along with the extrinsic toughening mechanisms, result in a material with both high modulus of elasticity and high toughness. Interestingly, most of the biogenic composites exhibit similar behaviour (Figure 2-14) [*Fratzl 2008b*] –Ch7].

Furthermore, the different components contribute differently to the mechanical properties according to the type of loading. Collagen for example seems to provide tensile strength while the mineral phase is responsible to withstand compressive forces [*Weiner and Wagner 1998b*]. Recent studies show that NCPs, despite the fact that they only constitute ~10% of the whole tissue also play an important role on load bearing, thus effecting fracture toughness. They act as organic glue that holds together the mineralized collagen fibres. The applied load is transmitted from one fibre to another or from collagen to the mineral by shear loading these proteins (Figure 2-15: top). Moreover, the unfolding procedure involves stretching of this NCP meshwork and at some extent breaking of ion-mediated sacrificial bonds. This results in energy dissipation and increases the material's stiffness and fracture toughness (Figure 2-15) [*Fantner et al. 2005b; Gupta et al. 2006c*].

In more detail, when bone is under tension, the applied load is transferred from the mineralised fibrils to the adhesion medium that holds together the non-collagenous matrix and vice versa [*Gupta et al. 2006c*]. This matrix is a spaghetti-like meshwork of unstructured NCPs like those presented in the bottom picture of Figure 2-15. Numbers 1-3 in this image, indicate the possible ion-mediated bonds formation at a meshwork like this. As NCPs have negatively charged domains, positive ions bond on them acting as inter- and intra-molecular cross-links. Such links could form between negatively charged domains of the same or different polymeric molecules or between NCP and mineral crystals [*Fantner et al. 2005b*].

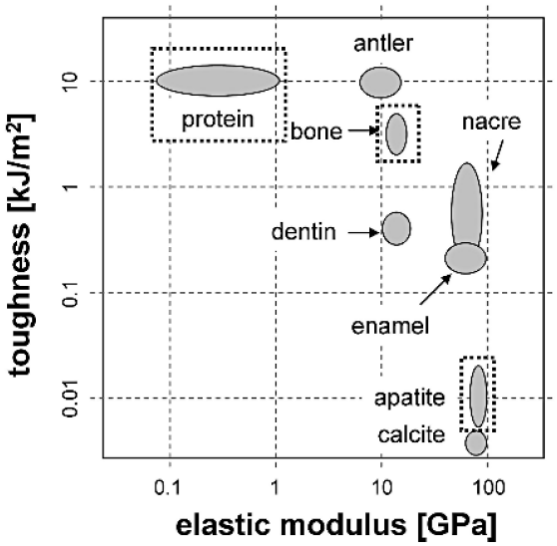

Figure 2-14: Ashby plot of toughness vs compliance for various biologically relevant materials. Composite materials like bone, dentine and enamel combine high stiffness with high toughness as a result of the combination of elastically dissimilar materials. (Adapted from [*Fratzl 2008b*] – Ch7)

Stressing this meshwork initially results into the breakage of these ion-mediated links and followingly into the breakage of the actual molecule. This procedure requires a mean force of 100 –300 pN per molecule and as a result dissipates considerable amount of the applied energy into heat. Calculations have shown that the 1% per weight fraction of NCPs in the bone matrix is enough to explain the ~150 MPa yield strength measured for bone. Most importantly, these bonds between the same or new domains can be reformed once the strain is removed [*Fantner et al. 2005b; Gupta et al. 2006c*].

In addition to these mechanisms which act intrinsically during loading, protecting bone from crack initiation, there are also extrinsic mechanisms which contribute significantly to fracture toughness during crack growth. These mechanisms are present in higher hierarchical levels (Level 4 – 6) and include crack bridging via collagen fibres, un-cracked ligament bridging as well as crack twist and deflection on the various micro-features (osteons, lamellae, cement lines) [*Launey et al. 2010*]. The extrinsic toughening mechanisms act together with the intrinsic ones after crack initiation as a common "defence front"

against catastrophic failure, but the intrinsic mechanisms are the ones comprising the first line of defence against crack initiation [*Launey et al. 2010*].

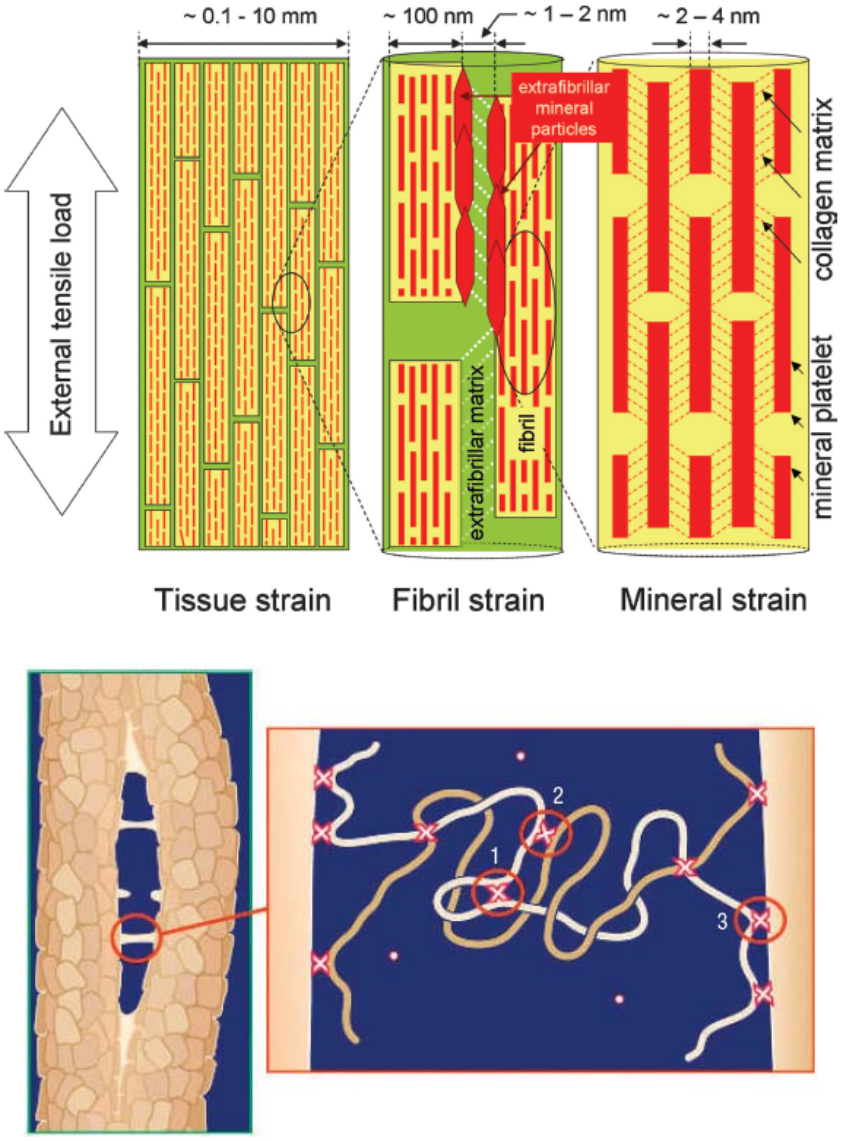

Figure 2-15: (top) Gupta's proposed deformation models for bone. Tensile load applied on the tissue causes the separation of mineralized collagen fibrils. This separation is transferred through the NCPs (white dots) to the next collagen fibril. Similar mechanism can be observed within the mineralized fibril, where the shearing of the inter-particle collagenous matrix translated into tension on the mineral plates (Adapted from [*Gupta et al. 2006c*]); (bottom) During stretching of the NCPs the unfolding and breaking of ion mediated bonds dissipates energy thought the matrix increasing the stiffness of the material. (Adapted from [*Fantner et al. 2005b*])

2.2.2 The Role of Non-Collagenous Proteins

Throughout the various hierarchical levels NCPs play a very important role not only from the biological and biochemical point of view but also form the mechanical. From level -2 and all the way up to level -7 NCPs facilitate attachment, stabilise interfaces, reinsure optimal load transfer and repeatedly dissipate significant amounts of energy protecting bone against failure.

Gupta *et al.* studied bone deformation by means of in situ micro-tensile experiments during high brilliance synchrotron X-ray diffraction. They discovered that in the elastic range mineral plates and collagen fibres carry approximately the 55% of the applied load while in the plastic region their contribution on load-bearing drops down to 45%; that is less than the half. According to them, the remaining load must be carried by the remaining NCP organic components [*Gupta et al. 2006c*].

Grynpas et al. used gel electrophoresis to investigate the changes in concentration of collagenous and NCPs in osteoporotic bone. They found that in osteoporotic bone the presence of NCPs is significantly decreased from 9.1% of the total organic matrix in young control groups or 11.4% in old control groups to 6.4% [*Grynpas et al. 1994*]. Since osteoporosis is known to increase the likelihood of bone fracture, a potential association between the diminished bone toughness and the decrement of the NCPs content should be considered. In fact a resent study by Thurner *et al.* focused on this association by studying the way that osteopontin (SIBLING NCP) deficiency affects bone fragility on mice. They find that on the osteopontin-deficient animals the fracture toughness of their bone reduced by 30% and their elastic modulus by 15.1% compared to the wild-type littermates. They present, probably for the first time, evidence which strongly correlate the mechanical behaviour of the bone with its NCP content [*Thurner et al. 2010a*].

2.2.2.1 Level 2: mineral – collagen attachment

Regardless of the role that NCPs have at the mineralisation process these proteins are known to bind on both collagen and mineral crystals. Specifically, on the crystal side the negatively charged NCPs bound on positively charged domains of the crystals [*Denhardt and Guo 1993; Fujisawa and Kuboki 1991; Goldberg et al. 2001; Kirkham et al. 2000a; Wallwork et al. 2002*] while

collagen-binding domains attach to the collagen molecules [*Tye et al. 2005*]. Hence, it seems very likely that these proteins act as adhesives between the two phases forming the "lower-level" interface within bone structure [*Gupta et al. 2007; Gupta et al. 2005*].

2.2.2.2 Level 3: building up the mineralised collagen fibre

Moving on to the next hierarchical structure, which is the mineralised fibre of level 3, another interface appears; this time between the mineralised fibrils which constitute the fibre. Here the inter-fibrillar space is filled with mineral crystals (also referred to as "extra-fibrillar minerals) [*Bonar et al. 1985; Pidaparti et al. 1996*], NCPs [*McKee et al. 1989; McKee et al. 1993*] and probably other non-collagenous moieties like glycosaminoglycans and/or lipids.

Fantner and co-workers [*Fantner et al. 2005a*] take a closer look at this region focusing on its non-fibrillar organic component. They propose that this non-fibrillar component acts as "glue" sticking the mineralised fibrils together (Figure 2-16). During loading this "glue" is stressed resisting fibril separation. At the same time rupture of ion-mediated sacrificial bonds dissipate significant amount of energy adding further to the toughness of the material [*Fantner et al. 2005a*].

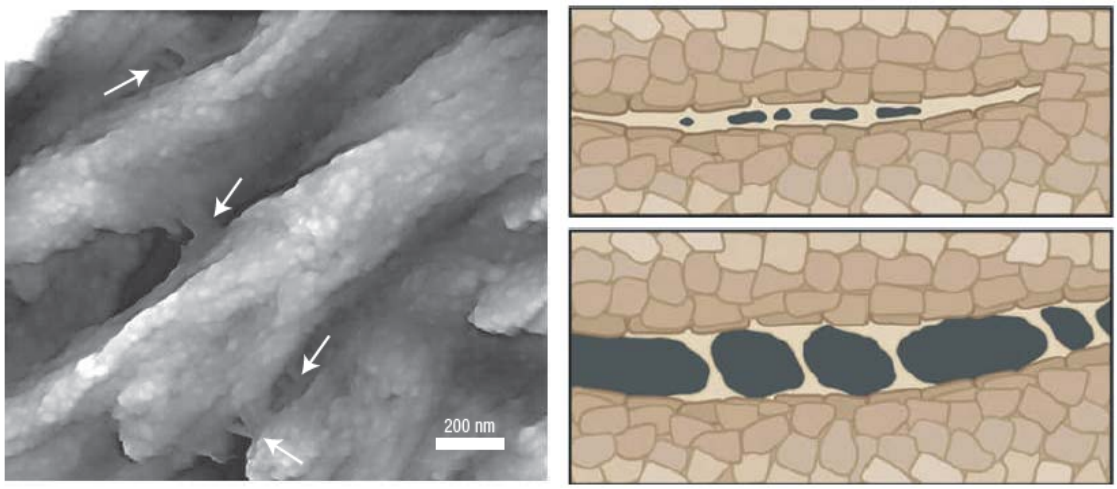

Figure 2-16: (left) AFM image of a fractured surface showing the interfibrillar NCP glue; (right) schematic representation showing the interfibrilar glue resisting fibrils separation.

Further to this point, shear transfer in this matrix redistributes the load between the fibrils preventing stress concentration and consequently crack formation [*Fantner et al. 2005a*].

2.2.2.3 Level 4 and 5: bone fracture and the role of NCP-rich interfaces

In these levels, the actual role of NCPs in terms of mechanics is in a big part a mater of ongoing research. While both the mechanical- and the fracture behaviour of bone tissue have been extensively studied at these scales, only a few data correlating these behaviours with the NCPs are available.

Level 4 features i.e. single lamellae, interlamellar areas and cement lines are known to have different mechanical properties. For example single lamellae exhibit higher modulus of elasticity than interlamellar areas and cement lines [*Donnelly et al. 2006; Gupta et al. 2006a*] but the source of this dissimilarity is not clear yet. It most likely is a combination of the inner architecture, i.e. arrangement of the fibres [*Gupta et al. 2006a*], composition [*Derkx et al. 1998; Nanci 1999*] and degree of mineralisation [*Donnelly et al. 2006*]. Furthermore, these features are also known to affect bone fracture behaviour. During failure, crack propagation preferably occurs through the interlamellar areas and cement-lines [*Peterlik et al. 2005*] while single lamellae act as crack barriers deflecting/twisting or even stopping the cracks [*Gupta et al. 2006a; Koester et al. 2008; Launey et al. 2010*]. Likewise, at the osteonal level (Level 5) cracks tend to deflect on the osteons and preferably propagate through the interstitial bone [*Nalla et al. 2005*]. Interestingly, both cement lines and interlamellar areas which facilitate crack propagation are enriched in NCPs [*Derkx et al. 1998; Nanci 1999*] suggesting their importance on the ultimate fracture behaviour of the tissue.

2.2.2.4 Level 6 and 7: Osteopontin deficiency and fracture toughness

The fracture of bone is a highly complex process on which all the hierarchy levels of the structure are involved. For fracture to occur at the higher levels (level 6 and 7), failure has to be also taking place at the lower ones. This "lower–level" failure generally occurs at the weak interfaces found in each level which, as described above, are populated by NCPs or they are NCP-rich. Therefore it can be argued that variability, such as compositional variations, at these interfaces may influence fracture behaviour and hence fracture

toughness. This hypothesis was recently tested by Thurner and co-workers which studied the structure, composition, and material properties of bone from osteopontin-deficient mice and wild-type littermates at several length scale [*Thurner et al. 2010b*]. The results showed that blocking the expression of osteopontin, OPN, one of the main non-collagenous proteins of bone, results in a decrement of bone fracture toughness by as much as 30%.

2.2.3 Osteoporosis

As already mentioned in the introduction of this thesis age or disease related increment in bone fragility lead to a large number of fractures witch for the UK alone have been estimated to over 200,000 per year [*Bukhari 2009*]. The condition that has been associated with this kind of skeletal fragility is called *osteoporosis* and according to the national institute of health, NIH, is defined as "*a disease characterized by low bone strength, leading to enhanced bone fragility and a consequent increase in fracture risk*" [*Marcus et al. 2009*][6]. From this definition one can see than osteoporosis is a condition associated with *increased fracture risk* which is something that cannot be directly measured. In fact is has been argued that "*it is debatable if osteoporosis should be considered as a unique diagnostic entity or it would be more accurate to be viewed as the result of the various [risk] factors […] which affect the fragility of the skeleton*" [*Riggs and Melton 1995*][7]. In order to give a measure of the complexity of the fracture risk assessment, some of the factors that affect bone fragility will be briefly presented in the next section.

2.2.3.1 Bone remodelling regulation

Reduced bone remodelling[8] is one of the main reasons of bone loss and it depends on both intrinsic (biological) and extrinsic (mechanical stimulus) factors. In this context, as intrinsic factors are considered the various sex hormones which regulate remodelling. These are mainly steroid hormones

[6] Chapter 2

[7] Chapter 2

[8] Bone remodelling has been discussed in §2.1.3. It is defined as the biological process during which new bone is formed on the surface of pre-existing bone tissue

including oestrogens and testosterone. Oestrogen deficiency reduces remodelling by increasing the lifespan of the osteoclasts which in turn results in bone resorption. In both sexes, steroid hormone expression reduces with age but this reduction is faster in women which is also the reason why elderly women are of higher risk than men [*Khosla et al. 1998; Riggs et al. 2002*].

Extrinsic factors are all these activities affecting the mechanical stimulus of bone like for example exercise. Bone remodelling is highly affected by the strain environment and continually adapt on it by adjusting its bone mass and distribution. Long term low-strain environment such the one caused by the lack of exercise or normal activity levels also results in bone resorption [*Riggs et al. 2002*].

2.2.3.2 Nutrition

With bones being the main storage repositories of both calcium (Ca) and phosphorus (P) in the body, when the typical baseline intake of 1100 mg/day and 700 mg/day for the Ca and P respectively are not reached the body turns to them. In this case bone resorption occurs to prevent hypocalcemia. An indirect effect on bone resorption has been also noted to occur due to low or high protein intake. "Indirect" because for low protein intake, bone resorption does not occur to restore protein concentration as in the case of low Ca intake, but it is instead affecting the Ca concentration which in turn causes the bone resorption [*Ilich and Kerstetter 2000*].

2.2.3.3 Lifestyle and other risk factors

The risk of fracture is not related only to bone biology but it also to life style. Apart from the exercise which mentioned earlier, nicotine, alcohol and caffeine have also been implicated in fracture risk [*Kanis et al. 2005b; Kanis et al. 2005c; Kiel et al. 1990*]. Finally, a set of other factors which do not directly associate with bone quality can also increase fracture risk in elderly people. For instance, the fracture risk of a 40 year old individual is not the same of that of a 70 year old even if bone quality is similar among the two. An elderly individual is more likely to fall due to factors like reduced vision or reduced mobility. At the same time due to the same factors the fall severity is also higher which in turn results to a higher fracture risk [*Greenspan et al. 1994*].

It is obvious that taking all these factors into consideration for the assessment of bone fracture risk in everyday clinical practice would be extremely difficult, if not impossible, and also very expensive. What we need is a parameter that it is somehow associated with all these risk factors, or at least with the most important ones, and which we can easily measure. The role of this parameter is currently held by the BMD. In clinical practice BMD is measured as index of bone quality based on the definition of osteoporosis formulated by Who. Based on it an individual with BMD < 1 of the standard deviations of the BMD of the healthy young population is considered osteopenic while with BMD < 2.5 osteoporotic [*Kanis 2008*].

In other words, in this approach BMD is screened as a measure of bone quality and thus associated with the risk of fracture.

Consequently, the treatment of osteoporosis is also focused on restoring the BMD within the "normal" limits. This is usually done with drug therapy aiming to inhibit osteoclastic activity. Common drug therapy involves the administration of biophosphonates, calcitonin or estrogens [*Deal 1997*].

Unfortunately, while BMD is directly correlated with fracture risk on large population [*Kanis 2008*], it fails to do so for the individual [*Marshall et al. 1996*]. A characteristic example of this is the study of Siris et al. where 149,524 white postmenopausal women aged 50 -104 years (mean age 64.5 years) where screened for osteoporosis based on the measured BMD. They found that 82% of women who had experienced a fracture within one year after the evaluation had not been classified as osteoporotic. [*Siris et al. 2004b*].

This difficulty of BMD to accurately predict fracture risk derives from the dependence of fracture risk upon factors which are not directly associated with BMD. It is noteworthy that the recent NIH definition of osteoporosis, given at the beginning of this section, based on these observations does not contain the term BMD. In contrast it draws the attention on bone's strength implying that this is the key factor of an accurate assessment of fracture risk.

Chapter 3

Experimental Techniques for Studying Bone Structure, Synthesis and Mechanics

In this chapter the main experimental techniques which are used in this study are briefly presented and discussed.

3.1 Atomic Force Microscopy

Scanning probe microscopy (SPM) or Atomic Force Microscopy (AFM) is a technique introduced in 1986 by Binning *et al.* [*Binnig et al. 1986*] capable of obtaining information related to the nanoscale features of the sample. This information could be topographical (imaging), mechanical, (stiffness, elastic modulus, adhesion, friction) or chemical (chemical force microscopy – CFM) information [*Jena and Hörber 2006; Kirkham et al. 2000b; Thurner 2009*].

In principle, AFM measures the changes of deflection or oscillation amplitude of a cantilever that is scanning across the sample's surface. A feedback signal is then produced from this change and a controller adjusts the height of the cantilever with respect to the sample surface in order to keep deflection or amplitude at a constant, pre-defined, set point. As topographic variations could be even of the order of some picometres, scanning and cantilever positioning is achieved by means of three piezoelectric transducers (X- , Y- and Z-piezos). By shrinking or expanding the Z-piezo where the cantilever is mounted, the controller keeps deflection or amplitude at the desired set point. Finally, these adjustments are linked with the lateral X, Y position of the cantilever, converted from Volts (V) to nanometres (nm) based on the piezos' calibration and plotted [*Meyer 1992*]. Figure 3-1 schematically represents the AFM operation.

The deflection of the cantilever is produced from a four segment photodiode (Figure 3-1). The actual deflection signal is calculated from the voltage that is produced in each segment of the photodetector.

AFM imaging can be accomplished in many different ways depending on the information which is being recorded. For surface topography the most common modalities are *contact* and *non-contact* scanning (Figure 3-2). In each one of these, two different imaging modes can be selected. These are the *static* mode in which the cantilever is driven in a constant deflection along the surface or the *dynamic* mode in which the cantilever scans along the surface while is being oscillated close to it [*Meyer 1992*].

In contact mode the cantilever's response is mainly due to strong ionic repulsive forces and thus high resolution images can easily be obtained. In non-contact mode, the cantilever scans in a small distance above the sample's surface (typically 10 –100 nm) without touching it.

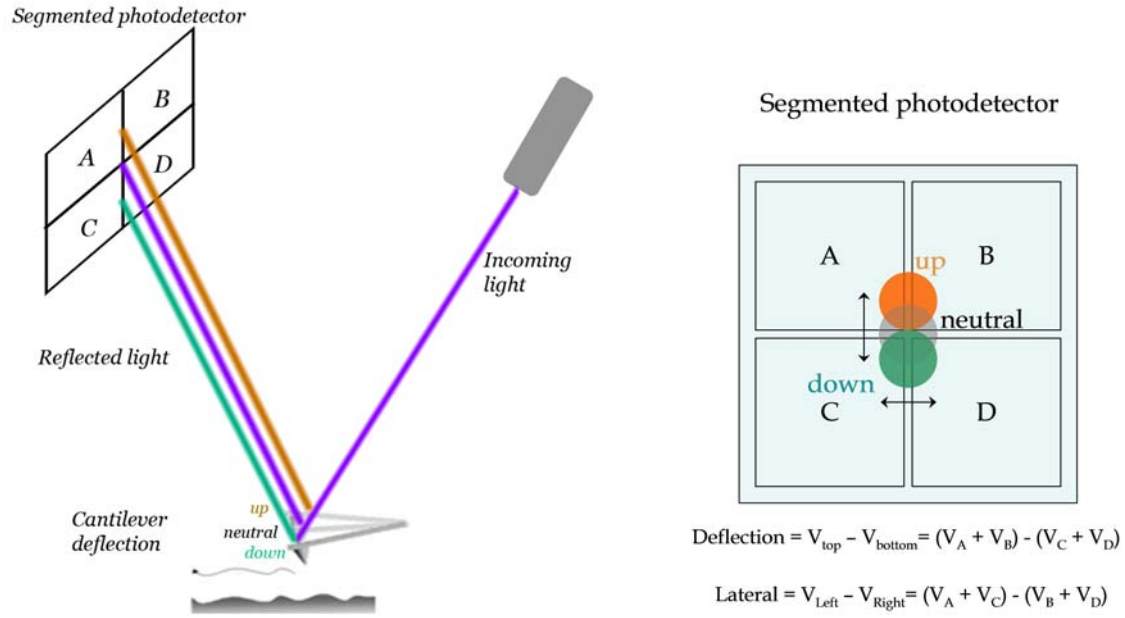

Figure 3-1: Schematic representation of an AFM cantilever scanning a sample's surface in "contact mode". The controller approaches or withdraws the cantilever when the deflection in below or above the setpoint by shrinking or expanding the Z-piezo (picture courtesy of O. Andriotis; 2011).

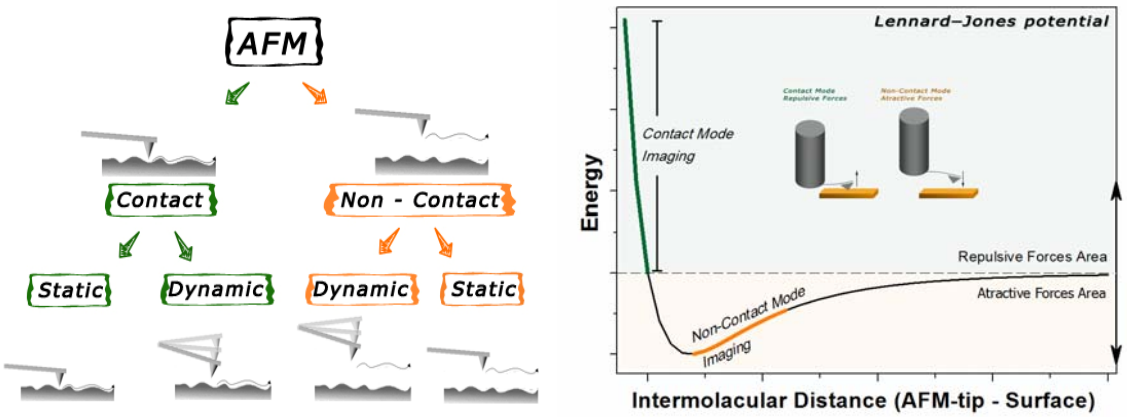

Figure 3-2: Possible operation AFM modes (left) and the Lennard – Jones potential which describes the interactions between the tip and the surface (Right)

In this mode, the response of the cantilever is governed by longer range –attractive– forces like van der Waals, electrostatic, magnetic or capillary forces. Figure 3-2, depicts a schematic diagram of the different AFM imaging techniques as well as the Lennard–Jones potential which can be used to describe the interactions that take place at various modes [*Meyer 1992*].

A tip radius which can go down to ~3 nm allows the cantilever to "feel" topographical variations of several nanometres, while the low spring constant (0.006 N/m –48 N/m) ensures that the cantilever will react even on the presence of a tiny potential [*Thurner 2009*]. Figure 3-3 depicts a schematic diagram of the MFP3D^{TM} AFM (Asylum Research) used in this study. The photodiode (position sensitive detector) which produces the signal of the deflection or oscillation amplitude of a cantilever as well as the piezoelectric actuator, which is responsible for controlling the micro-movements of the cantilever, are noted.

AFM offers the ability to scan samples under ambient environmental conditions or even under conditions which simulate the physiological environment of the sample, e.g. scanning in flow cell, temperature regulated scanning etc. while at the same time the imaging resolution is comparable and sometimes even better to that of SEM or transmitted electron microscope TEM. This further allows studying of the structure-function relationship of the sample under various conditions. In bioengineering and biology, AFM is regularly used for characterising biological relevant samples. The characterisation techniques are

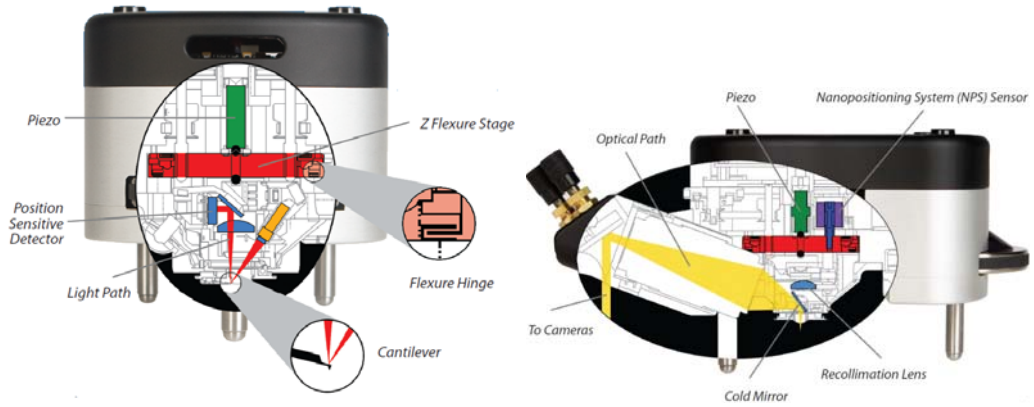

Figure 3-3: AFMs head (MFP-3D – Asylum Research). (Left) diffraction limited optics and a low coherence (instead of laser) light path. The NPSTM (Nano Positioning System) sensored Z axis measures the cantilever's position. (Right) Optical imaging light path (Images from Asylum Research web site)

not limited on imaging modalities. They have also been expanded on the assessment of inter- and intramolecular interaction of biomolecules, measuring forces involved in antibody –antigen interactions or assessing the nanomechanical properties of biological structures and molecules [*Jena and Hörber 2006; Kasas et al. 1997; Thurner 2009*]. These studies have shown that AFM is also a powerful tool for the characterisation of samples with complex hierarchical structure like bone. The ability of AFM to study the nanostructural features is immensely important in order to further our understanding of fundamental components of the tissue and the role that each one of these play on its ultimate mechanical properties [*Braga and Ricci 2004*].

3.1.1 Micromechanical Testing Apparatus (Nanorack™ prototype)

For the work presented in this thesis, a prototype micromechanical testing apparatus was manufactured by Asylum Research. This apparatus allows for the application of *in-situ* tensile loading of the sample during AFM analysis providing qualitative information about the occurring deformation and the crack propagation mechanisms [*Katsamenis et al. 2010*]. In this way, information about local deformations or crack propagation in cortical bone specimens can be gained. The stretching stage of the apparatus is manually controlled by two

micrometres and allows for two axis tensile stress control (500 μm per revolution; 5 μm resolution). The sample size can vary from a few- up to 12 mm in width, and up to 40 mm in length. A removable aluminium post is mounted underneath the sample stabilizing the sample against bending. The prototype apparatus is illustrated in Figure 3-4 while Figure 3-5 illustrates final, commercially available, version of this prototype (Nanorack®). In the commercially available apparatus a series of functions and characteristics have been improved the most important of which are: a) the presence of a controller witch support recording of the NanoRack's force and displacement readings via the MFP3D software; b) better sample gripping mounts which allow for easier and more stable sample mounting; c) support for wider and thicker samples as well as higher total travel which can reach up to 400%.

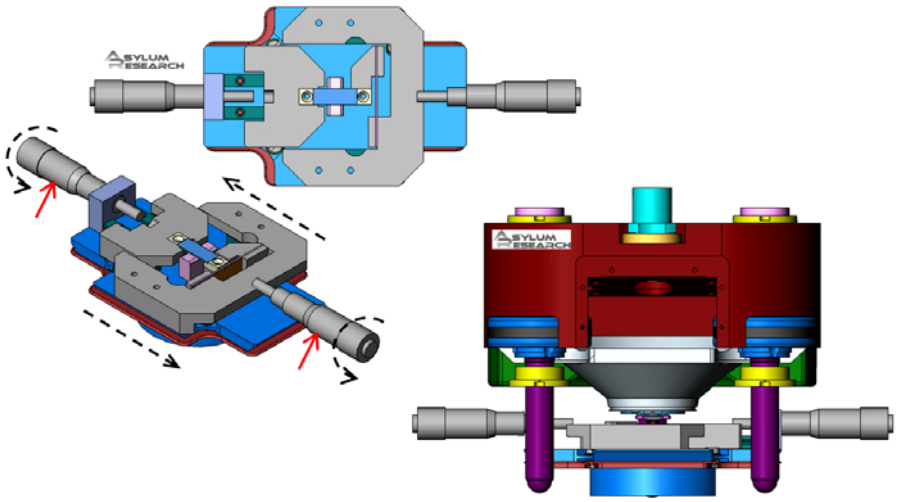

Figure 3-4: (top left) Nanorack® prototype apparatus. Two micrometer screws (red arrows) are fixed on both edges. Displacement is achieved via the micrometers' trimbles (black bashed arcs) (bottom right) front view of microtensile stage under the AFM's head. (Images courtesy of Paul Costales and Roger Proksch, Asylum Research)

Figure 3-5: (a) The nanorack® stage. The tensile stage is carried on the MFP-3D's XY scanner and interfaces with an instrument box containing signal conditioning electronics that are SmartStart bus compatible. The dual axis position encoders provide 5 μm positioning accuracy over the full 6 cm range of travel (12cm total) (Image courtesy of Asylum Research)

3.1.2 Cantilever-based Nano-indentation

Conventional "nanoindentation" is an adaptation of the classic indentation technique introduced by Oliver and Phar in 1992 [*Oliver and Pharr 1992*] for measuring the elastic properties of materials of smaller scales. This technique is using a micrometer-size indenter to apply pressure against the material's surface while it records the load vs indentation-depth curve [*Oliver and Pharr 2004; Oliver and Pharr 1992*]. The recorded curve is then used to calculate the elastic properties of the tested material. A typical "nanoindenter" tip size is of the order of some micrometers, but for several years the term nanoindentation was used to distinguish it from the traditional indentation.

The development of the AFM pushed the indentation-based mechanical characterisation of the materials to even smaller scales. AFM cantilever-based nanoindentation, as the name of the technique implies, is a mechanical characterisation technique which uses the AFM cantilever as the indentation probe. In principle, during AFM indentation the sharp AFM tip indents the surface of the sample at a certain loading rate until a maximum force (a.k.a force controlled indentation) or a maximum depth (a.k.a displacement controlled indentation) is achieved. A "hold time" at the maximum load or the

maximum depth is kept to allow for any transition processes like creep or stress relaxation to equilibrate, and then the load is removed. Finally, the indenter retracts from the sample leaving an imprint on the sample's surface. During this procedure the force and the displacement are constantly recorded. These data can then be used to calculate the elastic modulus, the stiffness and the hardness of the material.

In bone research community, the most widely used experimental approach for the characterisation of bone nanoelasticity uses a force controlled indentation [*Thurner 2009*] and the obtained data are analysed using the Oliver-Pharr method [*Oliver and Pharr 1992*].

A schematic representation of an indentation cross-section along with the various measures used for the analysis is illustrated in Figure 3-6. During indentation the recorded load – displacement curve has the form of the curve presented in Figure 3-7. According to the Oliver-Pharr method the unloading part of the indentation curve can generally be expressed by the following equation:

$$P = a(h - h_f)^m \tag{3-1}$$

where P is the load, h the displacement h_f the imprint depth left on the surface and a and *m* are power law fitting constants depending on the material of the indenter and its geometry.

By adjusting the parameters *"a"* and *"m"* the equation 3-1 can be fitted onto the unloading part of the indentation curve. From the fitted curve the unloading stiffness (*S*) can then be calculated as follows:

$$S = \frac{dP}{dh} = \beta \frac{2}{\sqrt{\pi}} E_r \sqrt{A} \tag{3-2}$$

where β is a correction factor related on the tip geometry, A the contact area between the material and the indenter at the position of maximum load and E_r the effective (or reduced) elastic modulus which is defined as:

$$\frac{1}{E_r} = \frac{1-\nu^2}{E} + \frac{1-\nu_i^{\,2}}{E_i} \tag{3-3}$$

with E, E_i being the specimen's and the indenter's Young's modulus respectively and ν, ν_i the specimen's and indenter's Poisson ratio.

E_r is a convoluted measure of the elastic modulus which accounts for the deformation of both the sample and the indenter during the indentation [*Oliver and Pharr 1992*]. When either the sample's or the indenter's Poisson's ratio is not known, the E_r which is derived from the equation 3-2 is commonly used. For an indenter much harder than the sample E_r essentially expresses the elastic modulus of the sample as the deformation of the indenter is practically zero.

In such a case rearranging the equation 3-2 and solving for E_r results in

$$E_r = \frac{\sqrt{\pi}}{2}\frac{S}{\sqrt{A}} \tag{3-4}$$

where again *S* is the stiffness of the material which can be calculated from the slope of the uppermost part of the unloading curve as shown in Figure 3-7 and *A* is the *contact area* between the material and the indenter at the position of maximum load.

Because of the elasto-plastic behaviour of the material (pileup phenomenon), at any time during loading the part of the *contact area*, *A,* equals to the projected area of the indenter at the *contact depth*, h_c. h_c is defined as "the vertical distance along which contact is made" and can be estimated by the intercept of the initial unloading slope with the displacement axis, *h,* (cf. Figure 3-7) [*Oliver and Pharr 2004; Oliver and Pharr 1992*]. Finally, the hardness, *H*, of the material can be determined from:

$$H = P_{\max} / A \tag{3-5}$$

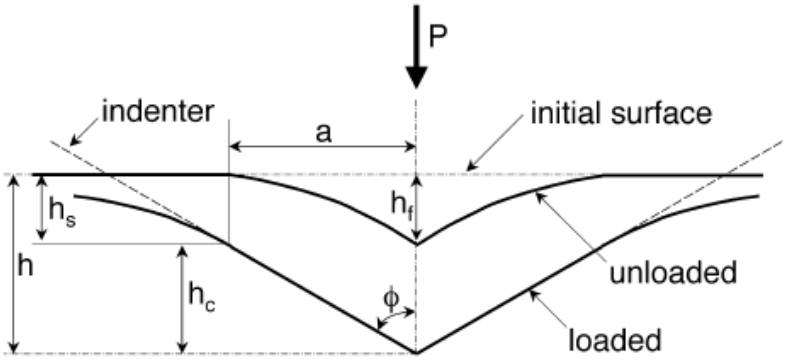

Figure 3-6: Schematic illustration of the indentation process showing parameters characterizing the contact geometry. *P*: load; *h*: the maximum indentation depth; h_f final depth; h_c: contact depth $h_c = h - h_s$; φ: conical indenter's half-included angle (image adapted from [*Oliver and Pharr 1992*])

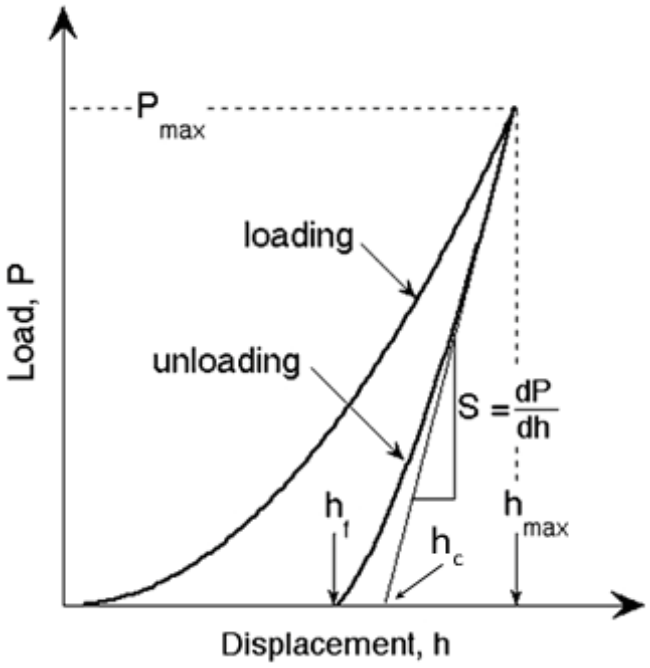

Figure 3-7: Representative load-displacement data plot obtained after a nanoindentation test [*Oliver and Pharr 2004*].

3.1.3 Digital Image Correlation (DIC)

Evaluation and quantification of the induced strains of a loaded sample is important in biomechanics, as it can provide information regarding the material's behaviour under various loading conditions. The most common method for experimental strain analysis is by means of strain gauges. Despite the wide use of this technique, one of the main disadvantages is that strain gauges can only measure strain on a single location. As a result, this approach is not able to produce strain maps. To overcome this limitation, the research community is nowadays moving towards non-contact strain measurements by means of Digital Image Correlation (DIC) systems.

DIC is applied on two or more subsequent images taken during different loading stages and then uses a mathematical correlation to calculate the magnitude and direction of the relative deformation of each image in respect to a reference one. By dividing the image into smaller parts (sub-images), the system is able to calculate the relative deformation of each one of them in respect to the corresponding sub-image of the reference. The resulted displacement vector can be different in both magnitude and direction among the different sub-images. This way, a displacement field (or map) which depicts the induced displacements on the sample's surface is generated [*Liu and Iskander 2010*].

DIC algorithm assumes that the gray-levels are not changing during the translation of the image and thus all the observed changes are attributed to the relative displacement of each sub-image in respect to the same sub-image of the reference image. In such case, for two sub-images, $f(m,n)$ and $g(m,n) = f(m+\Delta m, n+\Delta n)$ with a dimension of $M \times N$ pixels, the discrete cross-correlation function is given by:

$$c(l,k) = \sum_{m=1}^{M} \sum_{n=1}^{N} f(m,n) g(m+l, n+k) \tag{3-6}$$

As the auto-correlation (cross-correlation of one image with itself) results in a peak of cross-correlation function in the middle of the image, locating the peak of the cross-correlation function between the original and the displaced image results in a correlation peak located in a small distance from the centre of the image (Figure 3-8). This distance can be perceived as the relative displacement between the two images the magnitude of which is given by the distance of the

two correlation peaks while the vector which connects them defines the direction of the translation. This procedure is repeated for each sub-image resulting in a displacement map like the one shown in Figure 3-8.

Since DIC systems analyse subsequent images to calculate strains, it is able to push experimental strain analysis limits to a much smaller scale where analysis via stain gauges would be impossible [*Pan et al. 2009*]. In the present study, DIC was used on AFM images to analyse the behaviour under tensile load of the sub-osteonal features of bone (typical feature's size 1 – 10 μm).

Further use of DIC technique on loaded and unloaded AFM images allows the quantification of the induced strains on the imaged microstructural features. This could also lead to determination of the mechanical properties of these features and investigate possible changes due to age and/or disease [*Chang et al. 2005; Kammers and Daly 2011*].

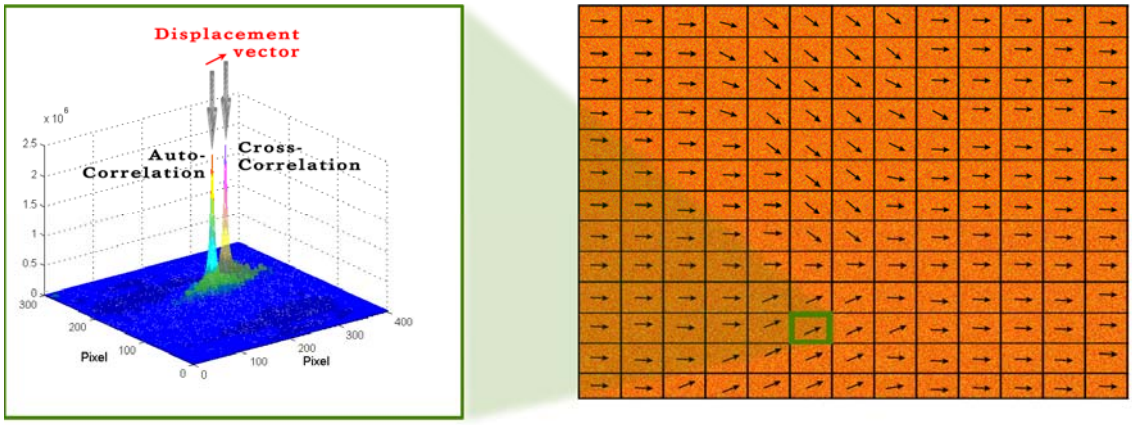

Figure 3-8: (left) The peaks of Auto- and Cross-Correlation functions as calculated for a sub-image; (right) Combination of the calculated vectors of all sub-images results in the displacement map.

3.2 Vibrational Spectroscopy: a short introduction

Over the last few decades vibrational spectroscopic has become a widely used characterisation technique among the researchers working in the biomedical

research. The main reason for this is spectroscopic methods are now able to provide molecular level information, by using a very small amount of material and in a very short time. Importantly, spectroscopical techniques are in general non destructive and easy to use [*Movasaghi et al. 2007b*]. The basic principal of vibrational spectroscopy relies on the physics of the light –matter interaction. In the next paragraphs a short introduction of these principles will be given in order to then be able to discuss the use of RAMAN spectroscopy for the characterisation of bone.

According to quantum mechanics as atoms form molecules, new discrete energy states corresponding to (1) the rotation of the whole molecule; (2) the vibrations of the atoms which build up the molecule and (3) the motion of the electrons within the molecule are formed [*Nakamoto 1986*].

The total energy of such a molecule is given by the sum of the nuclear and electromagnetic components and is expressed as

$$E_{total} = E_{nucl} + E_{elect} \tag{3-7}$$

where E_{nucl} is again a sum of the three nuclear components, i.e.

$$E_{nucl} = E_{trans} + E_{rot} + E_{vib} \tag{3-8}$$

here E_{trans} is the energy of molecule parallel translation; E_{rot} the rotation energies and E_{vib} the vibration of the molecule.

If the main goal is measuring the electronic excitations or the internal movements of the molecule, then the translation energy can be ignored. When a molecule interacts with an oscillating electro-magnetic field, *i.e.* radiation with specific frequency, energy can be transferred from the field to the molecule. This is only possibly if the conditions described by Bohr's equation are fulfilled. According to Bohr's equation that is when:

$$\Delta E = h\nu \tag{3-9}$$

where ΔE is the energy difference between the initial and the final quantum state h the Plank's constant and ν the radiation frequency.

Figure 3-9 depicts a simplified energy diagram of a diatom molecule as a function of internuclear separation. The quantum number *n* denotes the *electronic* state of the molecule where for the ground electronic state *n* =0 and *n* =1 for the first excited one. Each electronic state is divided into several *vibrational* states which are denoted with the vibrational state quantum number *u* (*u* =0 ground state, *u* =1 1st excited state, etc). Similarly, each vibrational state is divided into *rotational* states which are denoted with the rotational state quantum number *J*. In a certain vibrational state all rotational states are close to each other, thus the required energy for a rotational transition is relatively low. As a result, low energy radiation (low frequency or high wavelengths) can trigger these transitions (cf. Figure 3-9).

Rotational spectra measured in the bandwidth area of microwaves up to the infrared; that is $\tilde{u}$ =1 cm^{-1} (λ =104 μm) – 102 cm^{-1} (102 μm). It is reminded here that wavelength, λ, can be transformed into wavenumber, $\tilde{u}$, or, frequency *v,* using the formula:

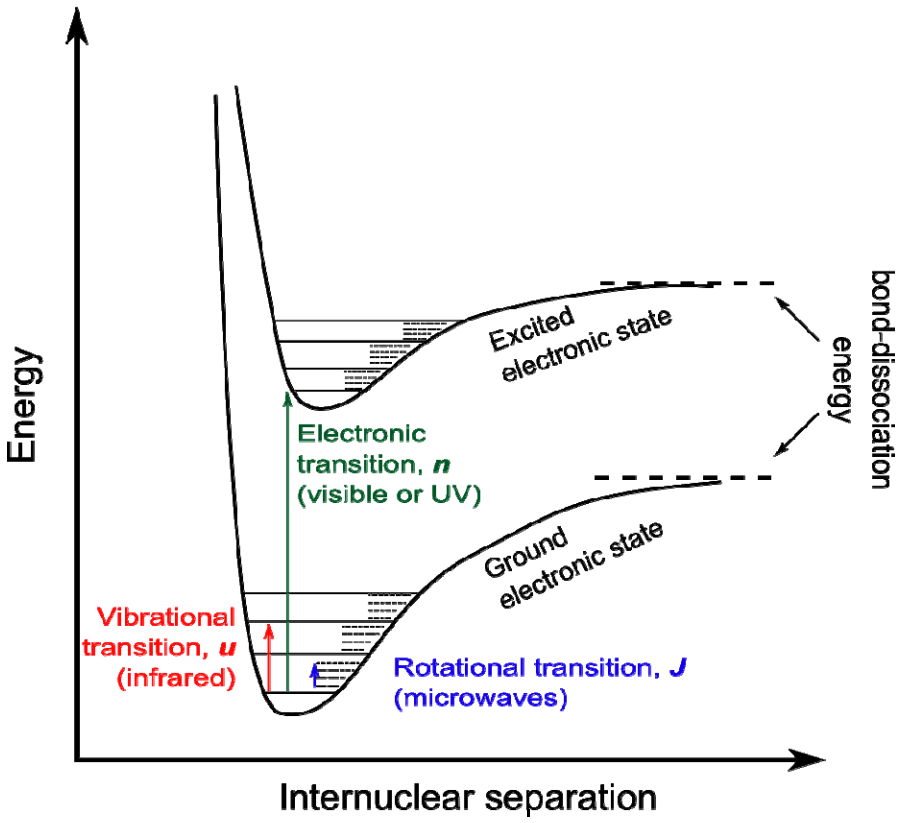

Figure 3-9: Simplified energy diagram of the energy states of a diatom molecule.

$$\lambda = c/\nu = 1/\tilde{u} \quad (3\text{-}10)$$

where *c* is the speed of light (299,792,458 m/s)

The energy gap between the vibrational states is higher and as a result a higher energy radiation (higher frequency or lower wavelength) is needed for a vibrational transition to take place. Vibrational spectra are usually recorded in the bandwidth area of $\sim \tilde{u} = 10^2$ cm^{-1} ($\lambda = 10^2$ μm) -10^4 cm^{-1} (1μm) which is the infrared area of the spectrum. Finally, electronic transition spectra for the same reasons are measured in the area of $\sim \tilde{u} = 10^4$ cm^{-1} ($\lambda = 1$ μm) up to 10^5 m^{-1} (0.1 μm) which is the visible or ultraviolet area.

Vibrational spectra are experimentally measured using RAMAN and IR spectroscopy but each one of these techniques depends on a different physical phenomenon. The main difference lies in the manner in which the energy is transferred from the radiation onto the molecule. IR spectra are generated by recording the absorbed amount of infrared radiation from the molecule at the different energies (wavelengths) and it is associated with changes in the molecular moment of the molecule. On the other hand, RAMAN spectra derive from measuring the amount of energy a monochromatic ray lost (or gained) during its interaction with the sample. This change is expressed as a shift of the ray's frequency towards lower (energy loss) or higher (energy gain) wavelengths and it associates with the change of the molecule's polarisation potential, i.e. the amount of deformation of the electron cloud of the molecule [*Nakamoto 1986*]. Raman and infrared spectroscopy are complementary techniques and they have both been widely used in biomedical research. In this study RAMAN instead of IR spectroscopy was used as it provides better spatial resolution [*Morris and Finney 2004*].

3.2.1 RAMAN and μ-RAMAN Spectroscopy

RAMAN spectroscopy is based on the RAMAN scattering phenomenon. A RAMAN spectrum depicts the intensity of the scattered radiation as a function of the energy difference between the incident and scattered radiation (in wavelengths) [*Lewis and Edwards 2001; Movasaghi et al. 2007a*]. RAMAN scattering is taking place when a monochromatic electromagnetic radiation

interacts with a molecule and depending on the induced vibrational transition, it loses or gains energy. This phenomenon, as it will be described bellow, is associated with the change of the polarizability of the molecule.

When radiation is scattered by a molecule, the scattered radiation contains both Rayleigh and RAMAN components. In contrast with the elastic (or Rayleigh) scattering where the incident radiation is scattered by the molecule preserving the same frequency, the characteristic feature of RAMAN scattering is the shift in frequency of scattered radiation in respect to the incident one. If the molecule's final energy is higher than the initial then the scattering is called *Stokes* Raman scattering. This for example could happen when the molecule is excited from the ground stage, g_0, to a higher virtual state and then returns to a higher state g_1 where $g_0<g_1<g_{virtual}$. If on the other hand, the molecule's final energy is lower (i.e. by starting from an elevated vibrational level following the transition route $g_1 \rightarrow g_{virtual} \rightarrow g_0$) the scattering is called anti-Stokes (cf. Figure 3-10 [*Lewis and Edwards 2001*]. All these can be more accurately described as follows [*Skoog et al. 2000*]:

Let *E* be the electric field of a monochromatic radiation. This can be expressed as:

$$E = E_0 \cos(2\pi v_{ex} t) \tag{3-11}$$

where E_o is the amplitude of the propagation wave, v_{ex} the frequency and *t* the time. When this wave interacts with the electron cloud of a bond, induces a dipole moment *m* which can be expressed by the:

$$m = aE = aE_0 \cos(2\pi v_{ex} t) \tag{3-12}$$

where *a* is a constant called *polarizability* and is a measure of the deformation ability of the bond. This is the parameter which also determines if a bond would be Raman-active or not. In order for the bond to be Raman-active, "*a*" should be a function of the nuclei distance, *r*, such as:

$$a = a_0 + (r - r_{eq})\left(\frac{\partial a}{\partial r}\right) \tag{3-13}$$

Here a_0 is the polarizability at the nuclei equilibrium distance, r_{eq}, and r is the distance between the nuclei at a given time. For an oscillating bond the change of the nuclei distance is given by:

$$r - r_{eq} = r_{\max}\cos(2\pi v_v t) \tag{3-14}$$

where r_{max} is the maximum distance between the nuclei in respect to the r_{eq}.

Substituting the 3-14 into 3-13:

$$a = a_0 + \left(\frac{\partial a}{\partial r}\right) r_{\max}\cos(2\pi v_v t) \tag{3-15}$$

which can then be used in 3-12 for expressing the induced dipole moment, m:

$$m = a_0 E_0 \cos(2\pi v_{ex} t) + E_0 r_{\max}\left(\frac{\partial a}{\partial r}\right)\cos(2\pi v_v t)\cos(2\pi v_{ex} t) \tag{3-16}$$

Finally, applying the trigonometric identity:

$$\cos x \cos y = \left[\cos(x+y) + \cos(x-y)\right]/2 \tag{3-17}$$

The 3-15 becomes:

$$m = a_0 E_0 \cos(2\pi v_{ex} t) + \frac{E_0}{2} r_m\left(\frac{\partial a}{\partial r}\right)\cos\left[2\pi(v_{ex} - v_v)t\right] + \frac{E_0}{2} r_m\left(\frac{\partial a}{\partial r}\right)\cos\left[2\pi(v_{ex} + v_v)t\right] \tag{3-18}$$

As previously stated, the scattered radiation contains all the three scattering components, i.e. Rayleigh, Stokes and anti-Stokes scattering, which are no other than the first, the second and the third term which appears in equation 3-18. Note that as said, Rayleigh scattering occurs at the frequency of the incident radiation (v_{ex}) while Stokes and anti-Stokes scattering occur at lower ($v_{ex} - v_v$) and higher ($v_{ex} + v_v$) frequencies around Rayleigh.

As there is higher probability a molecule to be found in its ground state instead of in an excited one, the Stokes raman scattering is stronger phenomenon when compared to the anti-Stokes scattering and thus a higher signal to noise

ratio can be achieved. For this reason the anti-Stokes raman area of the spectrum is usually used for the analysis [*Lewis and Edwards 2001*]. Nevertheless, RAMAN scattering is a very week phenomenon when compared to the Rayleigh scattering[***], thus in order to achieve Raman scattering of measurable intensity a powerful light source is needed [*Lewis and Edwards 2001; Movasaghi et al. 2007a*].

Biological sample characterisation by means of RAMAN spectroscopy has been widely used on more than thirty different types of biological samples including bone, proteins, cornea, cervical tissue, epithelial tissue, lung, breast, skin, etc. [*Movasaghi et al. 2007a*]. In many in order to achieve higher spatial resolution, a microscope is fitted on the RAMAN spectrometer and it is used to focus the laser beam onto a smaller area of the sample (spot size can go smaller that ~500 nm) and to collect the scattered radiation. This setup is called micro-RAMAN (μ-RAMAN) and it is this setup which will be used in the present study (Figure 3-11).

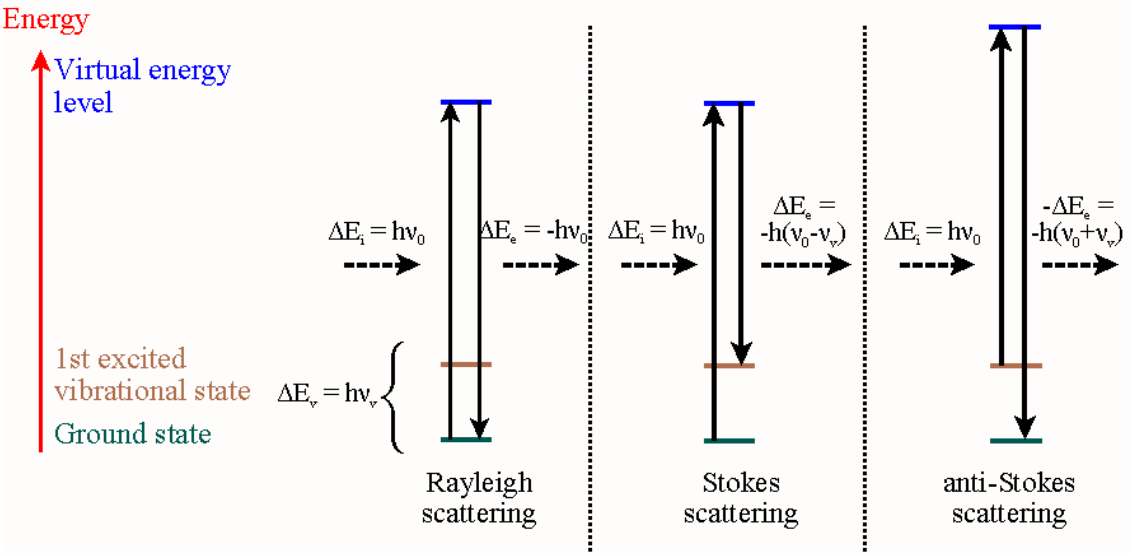

Figure 3-10: Elastic (or Rayleigh), Stokes (molecule absorbs energy) and anti-Stokes (molecule loses energy) Raman scattering of a diatom molecule. Lines represent the molecule's simplified energy diagram of the energy states (adapted from Wikimedia Commons (2011)).

[***] I_{inc} / I_{Rayl} / I_{RAMAN} ≡ 1 / 10^{-3} / 10^{-7}

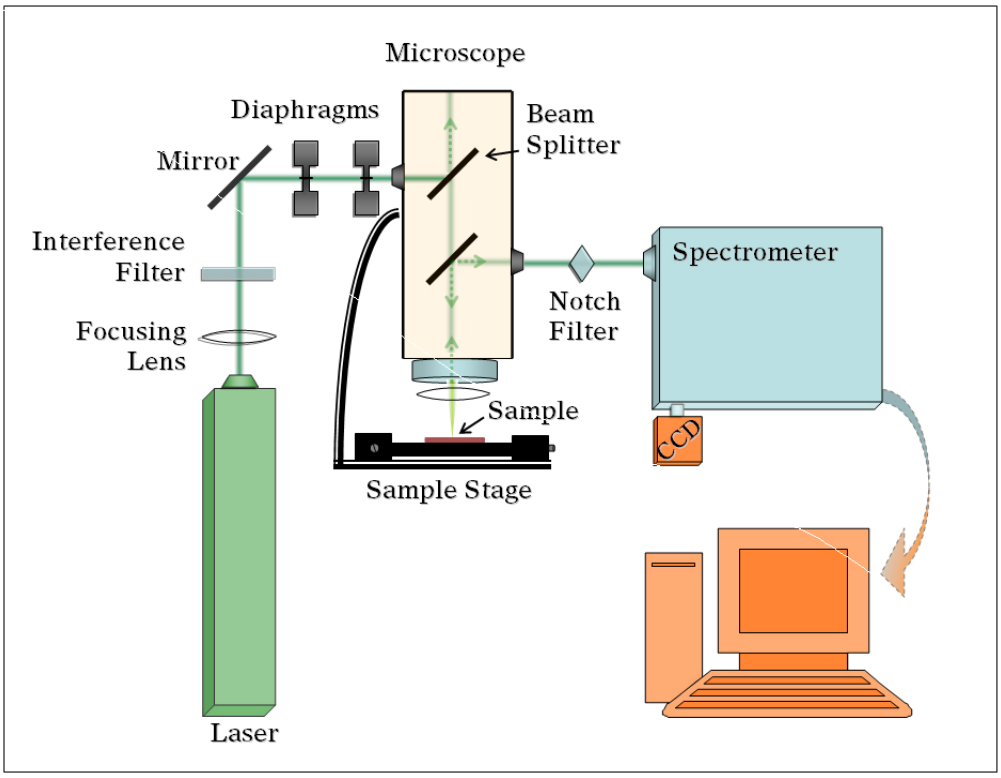

Figure 3-11: Diagram of a typical μ-RAMAN System

3.3 Reference Point Indentation

The reference point indentation technique (RPI) was introduced in 2006 by Paul Hansma's group as a micromechanical testing technique capable of direct assessment of bone's mechanical properties with in-vivo usage potentials. It is a technique based on the conventional[†††] nano-indentation measurements of bone but instead of using a free-standing indentation probe it uses a smaller one housed within a reference probe which during the measurement remains fixed at the bone's surface. The reference probe is a modified hypodermic needle in the order of 600 -700 μm in diameter while the test probe is conical shaped with a tip radius of 2 -3 μm [*Hansma et al. 2008; Hansma et al. 2006; Randall et al. 2009*].

[†††] "conventional" is being used to discriminate the technique from the AFM cantilever-based nanoindentation

The main difference of the RPI to the conventional nano-indentation is that the output measurments do not include hardness, stiffness or elastic modulus which can be produced from a single indentation curve [*Oliver and Pharr 2004*]. Instead, the RPI technique for each single measurement applies a number of indentation cycles (typically 10 -20) at a given frequency (typically 1 -2 Hz) [*Randall et al. 2009*]. Then, by comparing parameters like the indentation distance or the unloading slope between the first and the last indentation cycle generates a number of output parameters which can not be generated by the conventional nano-indentation. These parameters include the Indentation Distance Increase, IDI, which measures the indentation depth difference between the first and the last cycle; the Total Indentation Distance, TID, which measures the depth of the final indentation from the point of first contact of the first cycle; the average energy dissipation, ED, which is the average dissipated energy (defined as the area under the load-unloading curve) over all cycles (cf. Figure 3-12).

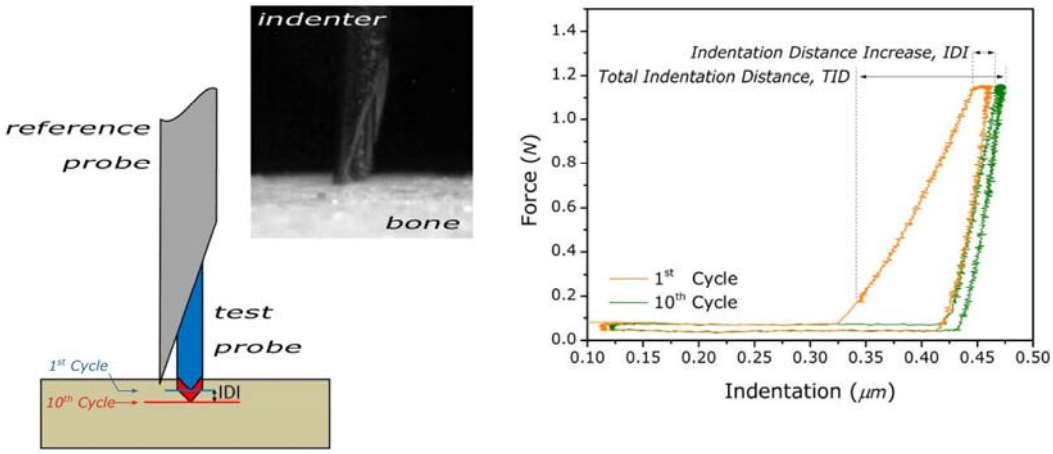

Figure 3-12: (left) Schematic representation and microscope image of the RPI indenter. The reference probe is a modified hypodermic needle with a 700 μm diameter housing the test probe; (right) Force vs indentation distance curves recorder during a single RPI measurement along with the definition of the IDI and TID. For clarity reasons only the 1st and the 10th cycle are presented.

Interestingly, while none of the forenamed parameters corresponds to any of the mechanical properties typically measured in bone research, recent RPI studies have shown strong correlation between IDI and diminished fracture toughness, age and damage development [*Diez-Perez et al. 2010; Hansma et al. 2008; Kennedy et al. 2012; Randall et al. 2009*].

3.4 Fracture Mechanics of Bone

3.4.1 Measuring fracture toughness

Probably the most clinically important property of bone, because of its direct correlation with the osteoporosis, is its ability to withstand loads without fracturing. In other words it is its *resistance to fracture* or *toughness*. It was not until recently (in 2008) that a reference tutorial in this topic was published by Ritchie *et al*. who analysed and compared the various techniques used in the past to evaluate bone's toughness. In their study, the calculation of mammalian bone toughness calculated by utilizing linear elastic fracture mechanics (LEFM) fracture toughness (K_c), non-linear elastic fracture mechanics (nLEFM) fracture toughness (J_c) and the crack resistance curve (R-curve) [*Ritchie et al. 2008*].

LEFM makes the following considerations: (a) the material is nominally elastic (b) the only inelastic area is around the crack tip and (c) the plastic zone remains small compared to the dimensions of the specimen. When these criteria are met, the local stresses, σ_{ij}, in an angle θ around the crack tip and in a distance r$\rightarrow$0 are given by

$$\sigma_{ij} \rightarrow \left[\frac{K}{(2\pi r)^{1/2}} \right] \cdot f_{ij}(\theta) \tag{3-19}$$

where $f_{ij}(\theta)$ is the angular function of θ and K is the so-called *stress intensity factor* which is defined as

$$K = Q\sigma_{app}(\pi a)^{1/2} \tag{3-20}$$

where Q is a geometry function, σ_{app} the applied stress and a the crack length. K is a factor that describes the local stress field and is expressed for the three different modes of crack displacement as K_I, K_{II} and K_{III} for mode I, II

and III respectively. These modes are schematically depicted in Figure 3-13. In LEFM the *fracture toughness* is defined as the critical value of the *K* at the moment of instable crack initiation ($K = K_c$).

Another approach for evaluating fracture toughness measures the strain-energy release rate (*G*). *G* expresses the "*rate of change in potential energy per unit increase in crack area*" and the *G*-value at the failure point (G_c) can be used as a measure of fracture toughness. For linear-elastic materials, the strain-energy release rate (*G*) can be expressed as:

$$G = \frac{K_I^2}{E'} + \frac{K_{II}^2}{E''} + \frac{K_{III}^2}{2\mu} \tag{3-21}$$

with μ being the shear modulus, *E'* the Young's Modulus in plain stress, and $E'' = E'/(1-v^2)$ with *v* being the Poisson's ratio [*Ritchie et al. 2008*].

In materials where the LEFM considerations do not apply, the contribution of the energy stored in the form of plastic deformation in the ultimate toughness of the material should also be taken into account. In such case the applied stress is associated with the resulted strain in a non-linear manner according to

$$\frac{\varepsilon}{\varepsilon_0} = \alpha\left(\frac{\sigma}{\sigma_0}\right)^n \tag{3-22}$$

where σ_0, ε_0 and α are constants, and *n* is the strain hardening exponent[‡‡‡]. Similarly to the LEFM in the nonlinear-elastic fracture mechanics approach (nLEFM) the local stresses around the crack-tip are given by the

$$\sigma_{ij}(\theta, n) \to \alpha\left(\frac{J}{\alpha\sigma_0\varepsilon_0 \mathrm{I}_n r}\right)^{1/n} f_{ij}(\theta, n) \tag{3-23}$$

where $f_{ij}(\theta, n)$ is the angular function, I_n the integration constant and J is the so-called *J-integral* which is the equivalent "*K*" parameter of the nLEFM. As in the LEFM the *J* characterises the stress and strain field around the crack tip.

[‡‡‡] The *n*-value relates to the ability of the material to be stretched and takes values between 0 for perfectly plastic materials and 1 for perfectly elastic ones.

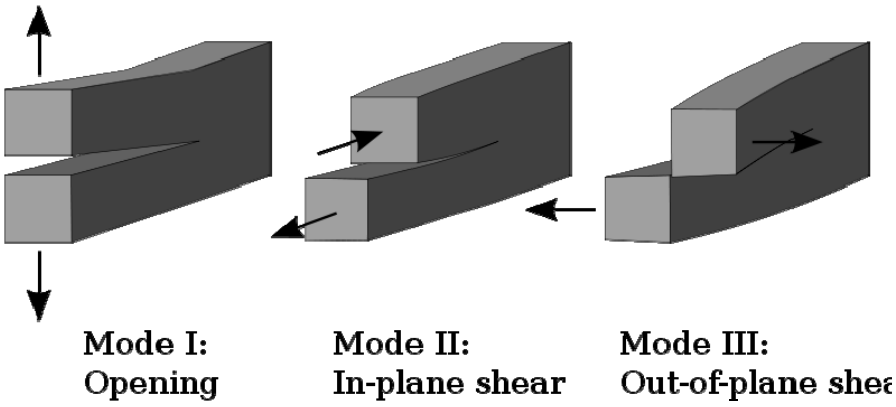

Figure 3-13: Mode I, the displacement is perpendicular to the crack (tensile opening); Mode II and Mode III, the displacement is parallel to the crack (Adapted from Wikimedia Commons; 2012).

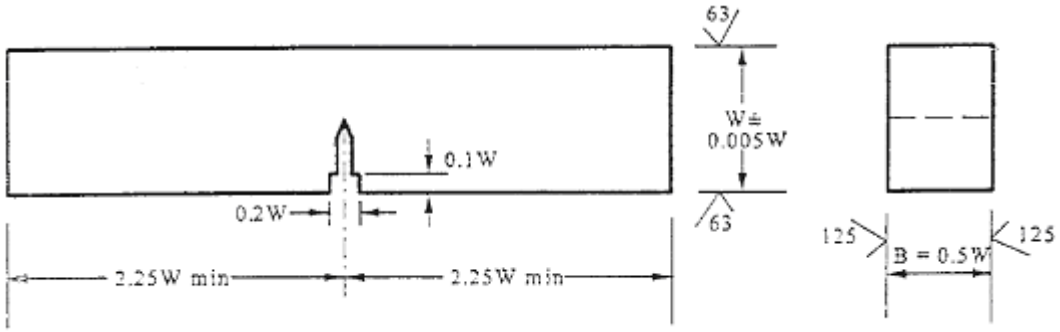

Figure 3-14: Single-edge notched three-point bend", SE(B), sample geometry. The machined notch shall be perpendicular to specimen length and the support span, *S*, should be $S \geq 4W$ and $1 \leq W/B \leq 4$ (Adapted from [*ASTM 2004*])

In bone research community, because of the limitation imposed by the size and the shape of the bone, and especially the human ones, the most commonly used sample geometry is the so-called "single-edge notched three-point bend", SE(B), sample presented in Figure 3-14. According to the American Society for Testing and Materials (ASTM) standards the SE(B) is a single edge-notched beam sample designed to be tested in three-point bending. It has a support span, *S*, nominally equal to four times the width, *W*, and the width to thickness, *B*, ratio should be $1 \le W/B \le 4$ [*ASTM 2004*]. In this case, the stress intensity factor, *K*, for a given load, *P*, and crack length, *a*, is calculated as

$$K_{(i)} = \left[\frac{P_i S}{\left(BB_N\right)^{1/2} W^{3/2}} \right] \cdot f\left(a_i / W\right) \tag{3-24}$$

where

$$f\left(a_i / W\right) = \frac{3\left(a_i / W\right)^{1/2} \left[1.99 - \left(a_i / W\right)\left(1 - a_i / W\right)\left(2.15 - 3.93\left(a_i / W\right) + 2.73\left(a_i / W\right)^2\right)\right]}{2\left(1 + 2a_i / W\right)\left(1 - a_i / W\right)^{3/2}}$$

where W is the specimen's width (3-25)

Followingly the *J* can be given by

$$J = J_{el} + J_{pl} \tag{3-26}$$

where J_{el} and J_{pl} the elastic and the plastic component of the load-displacement curve respectively. For the SE(B) sample

$$J_{el} = \frac{K^2\left(1 - \nu^2\right)}{E}$$
$$and \tag{3-27}$$
$$J_{pl} = \frac{2A_{pl}}{Bb_0}$$

where A_{pl} is the area under the load-displacement curve without the contribution of the elastic regime as shown in Figure 3-15, B the specimen's thickness and $b_0 = W - a_o$ the initial un-cracked ligament.

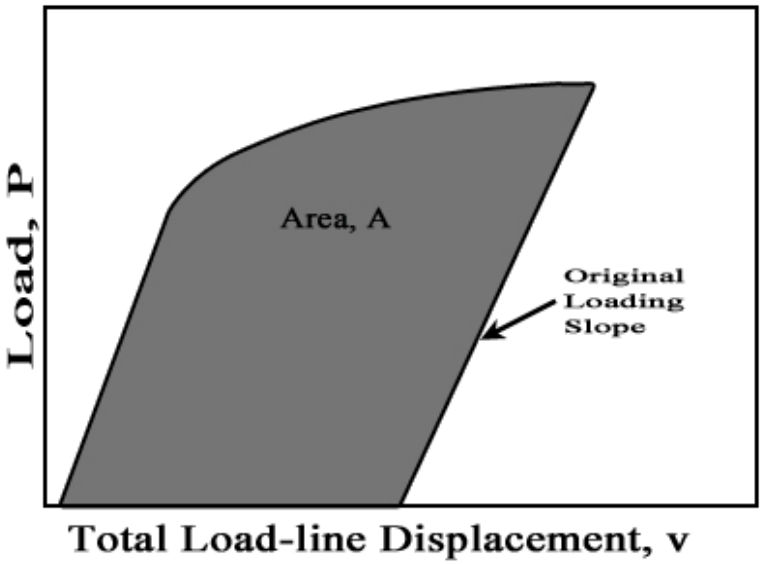

Figure 3-15: Definition of the "area under the curve" used in 4.17 for the calculation of J_{pl} (adapted from [*ASTM 2004*])

3.4.2 Crack-resistance curve (crack-growth toughness)

Because of the various intrinsic and extrinsic toughening mechanisms acting during bone fracture [*Launey et al. 2010*], stable crack propagation of significant length can occur prior to the occurrence of instable fracture. In this case, apart from the fracture toughness which describes the stress concentration factor at the moment of failure, K_C, tcrack-growth toughness of the material is also of high importance. Crack-growth toughness expresses the toughness of the material against the propagation of an existing crack for stress concentrations below the critical point, i.e. $K < K_C$. This requires the determination of the crack-resistance curve (also referred to as R-curve) which essentially describes the crack driving force, expressed in terms of K or G depending on the approach, as a function of stable crack extension, Δa [*Ritchie et al. 2008*].

In this case, the equations 4.25 and 4.26 are modified as

$$J_i = J_{el(i)} + J_{pl(i)} \tag{3-28}$$

where $J_{el(i)}$ and $J_{pl(i)}$ the elastic and the plastic component of the load-displacement curve respectively for the given load-displacement point. As before, for the SE(B) sample geometry [*ASTM 2004*]:

$$J_{el(i)} = \frac{\left(K_{(i)}\right)^2\left(1-\nu^2\right)}{E}$$

and (3-29)

$$J_{pl(i)} = \left[J_{pl(i-1)} + \left(\frac{2}{b_{(i-1)}}\right)\left(\frac{A_{pl(i)} - A_{pl(i-1)}}{B}\right)\right]\left[1 - \frac{a_{(i)} - a_{(i-1)}}{b_{(i-1)}}\right]$$

where A_{pl} is the area under the plastic part of the load-displacement curve as shown in Figure 3-16 B the specimen's thickness and $b_0 = W - a_o$ the initial un-cracked ligament

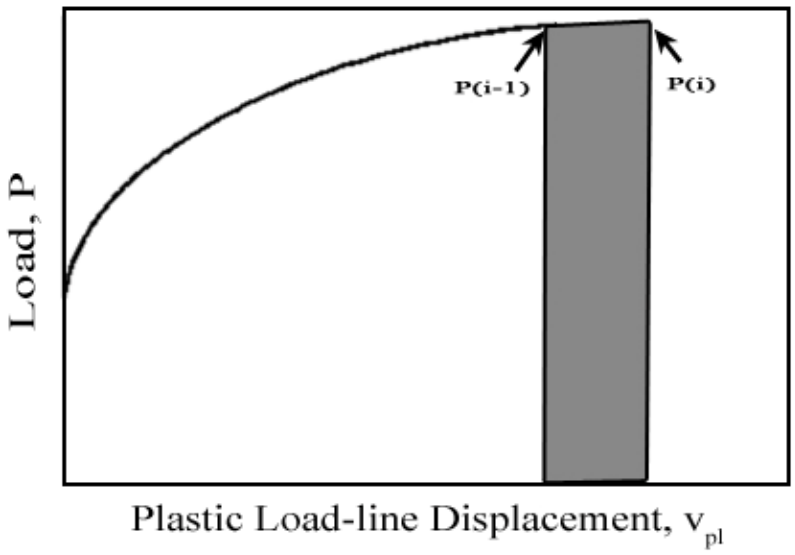

Figure 3-16: definition of the "area under the plastic deformation part" used in eq. 4.16 for the calculation of $J_{pl(i)}$ (adapted from [*ASTM 2004*])

Chapter 4

Elasto-Plastic Regions in the Micro-structure of Cortical Bone for Energy Storage and Dissipation

The study presented in this chapter has been published in the Journal of the Mechanical Behavior of Biomedical Materials [*Katsamenis et al. 2012*] while preliminary results obtained from it were presented in the following conferences:

- ✓ 17th Congress of the European Society of Biomechanics (ESB), Edinburgh, UK, July 5-8, 1058, 2010
- ✓ Annual Meeting of the Orthopaedic Research Society (ORS), Long Beach, LA, USA, January 13-16, 2011
- ✓ 2011 Scanning Probe Microscopy Meeting of the Royal Microscopical Society (RMS), Edinburgh, UK, June 22-23 2011

Mammalian bones are composed of mineralized type I collagen fibrils immersed in a matrix of non-collagenous proteins, which assemble into progressively larger features. Optimal load transfer, energy dissipation and toughening mechanisms have been discovered to some extend in some hierarchical levels, however to explain the remarkable properties of bone material, and specifically its toughness and elasticity, we need to understand how such mechanisms are integrated from the lower to the higher hierarchical levels.

The load transfer in the osteonal and sub-osteonal levels was the epicentre of this study aiming to elucidate the behaviour of lamellar interfaces (interlamellar areas) under loading conditions.

A previously unknown mechanism which transfers load and movement in a manner analogous to engineered "elastomeric bearing pads" used in bridges was discovered; while time-lapsed AFM imaging of stable crack propagation within the interlamellar areas proved their significant contribution towards fracture toughness.

4.1 Material and Methods

4.1.1 Sample preparation

One bovine femur was acquired from a local slaughterhouse and immediately stored in -20 °C until further preparation. Freezing is a common storage method used in the bone-research community as it allows for long preservation of the tissue without altering its mechanical behaviour [*Bonfield 1968; Linde and Sørensen 1993; Pelker et al. 2005*]. Bone samples (n ≥3 for all analysis methods except EDTA where n =1) were harvested from the midshaft of the femur as follows; a bandsaw (BG 200, Medoc, Logrono, Spain) was used for cutting the femur into transverse cylindrical-like pieces of ~4 cm long (Figure 4-1) and further cut them in half parallel to the bone's long axis. These bits were then cut onto slices of 800 μm and then again into rectangular bars of 0.8 - 1.0 mm width/height and 3 cm long oriented perpendicular to the bone's long axis, using a low speed precision saw (IsoMet, Buehler, Lake Bluff, IL, USA). Next, the samples were polished on their top side using sandpapers and diamond suspensions until a final surface roughness of ~1 μm was achieved. This is step is necessary in order to uncover to underlying lamellar structure of the cortical bone. In more detail, samples were first polished using a Grit 400 sand paper and followingly a Grit 600 and Grit 1200 (Buehler - Carbimet® Paper Disks) until a fairly smooth surface could be observed. The final polishing was given using microcloth polishing cloths (Buehler) and a sequence of 6 μm, 3 μm and 1 μm diamond suspension polishing solutions (Buehler MetaDi® Monocrystalline Diamond Suspension). After each polishing step the samples were immersed in an ultrasonic bath for five (5) minutes to clean the polished surface from any stacked bone powder and diamond crystal residuals. This is a cleaning method used frequently in the bone-research community [*Li and Aspden 1997; Zysset et al. 1999*] and it is crucial for avoiding contamination of the cloths with bigger size diamond crystals used on every previous step. It is

also important to note that the 1 μm roughness corresponds to the overall roughness of the sample. Areas with lower or higher roughness could still be found on the surface.

Finally, an initial notch (~300 *μm*) was made on one side of the specimen parallel to the bone's long axis by means of a low speed saw and was further sharpened to a final notch radius of a few micrometers using a surgical blade combined with 1 μm diamond suspension (Figure 4-1).

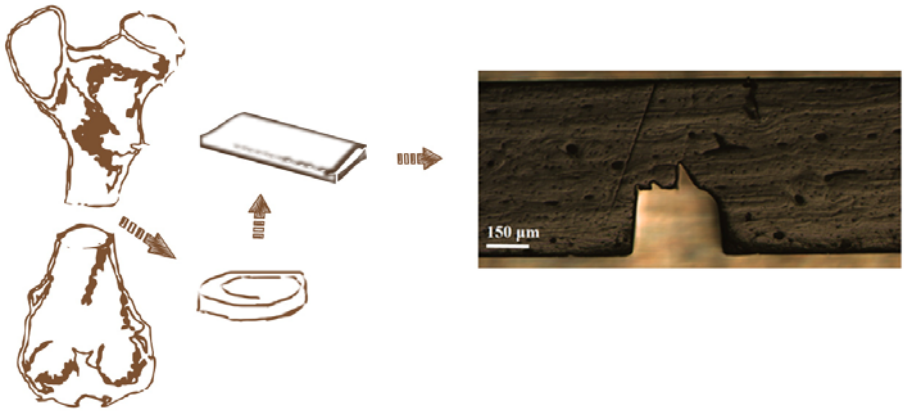

Figure 4-1: (*left*) Schematic representation of sample orientation on bovine femoral diaphysis. Drawing not in scale. (right) Optical microscope image of the final sample

For the in-situ AFM or Optical Microscopy imaging during micromechanical testing as well as for the nanoindentation experiments, the sample ends were embedded in PMMA resin, used as clamp points during the test. Figure 4-2 illustrates the final micromechanical testing specimen.

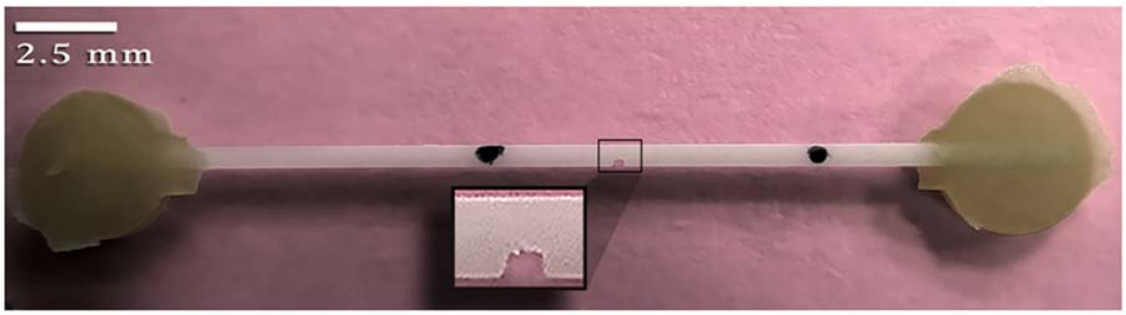

Figure 4-2: Micromechanical testing bone specimen

4.1.2 Micromechanical testing of cortical bone samples under light microscope

With these experiments, the micromechanical behaviour of the tissue under tensile (mode I) loading conditions was observed. The main aim was to observe how cracks propagate through the microstructure of bone tissue and to assess the ability of this experimental setup to capture stable crack propagation through the micro-features of cortical bone.

For micro-mechanical testing the prototype apparatus described in paragraph 3.1.1 was fitted under a metallographic light microscope which was operated in reflection mode. Tensile experiments were performed under displacement control (isostrain mode) with the rate of 0.05 mm/step. Measurement of load (displayed in N) and displacement (manually measured in mm) for each step were performed after the stabilisation of displayed load value. At this point the microscopic image was obtained as well.

4.1.3 In-Situ Micromechanical Testing of Cortical Bone Samples during AFM Imaging

Here, experiments are focusing on what actually happens within the lamination structures, i.e. osteons and lamellar bone, when cracks propagate through them. How lamellar and interlamellar areas behave during loading, and which is the preferable propagation path.

As before, the micro-mechanical testing prototype apparatus was used for stretching the sample during AFM imaging. In all cases, load and displacement did not exceeded 7.2 N or 0.015 mm respectively, which resulted in a maximum applied stress of 8.5 – 10.5 MPa. Images were acquired by means of an MFP3D AFM (Asylum Research) in contact mode, in air, using Au coated triangular silicon nitride probes (Olympus - TR400PSA; k = 0.08 N/m, Tip radius 20 nm).

All measurements were performed in air under ambient conditions and tensile experiments were performed as described in §4.1.2

4.1.4 Digital Image correlation

In order to visualise the strain field which had been developed in the osteonal structure under loading conditions, a region of interest (ROI) within an osteon was selected and the displacement map was generated by means of digital image correlation (DIC). The same approach was used to visualise the strain field of loaded osteon on which the cantilever-based indentation measurements had been performed (cf. §4.1.5). The procedure followed is described in more detail bellow.

First, AFM greyscale height images were acquired from the ROI (Figure 4-4) in contact mode using the same Olympus TR400PSA cantilevers in the unloaded as well as in the loaded state. The images were then extracted in lossless (.tif) format and enlarged in Adobe Photoshop® CS5 (v12 x64) using the bicubic interpolation algorithm (from initial image size 512 x 512 to 2000 x 2000 pixels). The strain map was then generated by feeding both images into commercial digital image correlation software (Vic-2D 2009, Correlated Solutions, Columbia, SC, USA). The subset size was set at 101 pixels (i.e. the number of pixels in each interrogation window) and the step size to 1.

4.1.5 Cantilever-Based Nanoindentation of Loaded and Unloaded Bone Osteons and Digital Image Correlation studies

To further understand the differences between lamellar and interlamellar areas, which may explain why cracks preferably propagate through these areas, AFM cantilever-based nanoindentation of loaded and unloaded bone osteons were carried out. Furthermore, digital image correlation analysis was employed to study any potential difference in the strain behaviour of these areas under tensile loading.

All bone samples were harvested from the cortical part of bovine femoral bone as described earlier in §4.1.1. Nanoindentation measurements of lamellae and interlamellar areas of secondary osteons were performed by means of MFP-3D AFM (Asylum Research) in order to study the potential differences in the elastic properties of these areas. It is noted here that all measurements were conducted on lamellae and interlamellar areas only. Cement lines were

considered distinct osteonal features and were not included in the analysis. Lamellae and interlamellar areas were distinguished visually based on the gray level, the size of the feature (typically ~ 1 μm for interlamellar areas) and the topography as expressed by the profile analysis (cf. Figure 4-3). The interlamellar areas exhibited diminished resistance against wear and they always appear lower than lamellae. This was true in both perpendicularly and parallel cut samples. To avoid indenting any potential "transition zone", all measurements were performed at locations central within each feature.

First step of the procedure was the imaging of the micro-tensile sample in order to locate the osteon of interest. This, had to be an intact secondary osteon lying as close to the pre-notch as possible to ensure the maximisation of the stress field when the sample was loaded. Next, a region of interest (ROI) that included two or more lamellae was selected. After imaging the ROI, approximately 600 ($550 \leq n \leq 625$) force controlled (max. load =80 nN; indentation rate =45 nm/s) force -indentation curves where recorded on each sub-osteonal feature.

The reduced modulus (E_r) was calculated separately for each force -indentation curve by applying the Oliver-Pharr model [*Oliver and Pharr 2004*] to the unloading data as described in §3.1.2.

A custom made Matlab® (version 7.10 Natick, Massachusetts: The MathWorks Inc., 2010) algorithm based on the numerical deconvolution proposed by Keller and Franke [*Keller and Franke 1993*] was used to reconstruct the tip shape (Figure 4-5) and the reconstructed tip shape was then used to calculate the cross-sectional contact surface area function.

In brief, Keller and Franke's "envelope reconstruction technique" uses the recorded height AFM image to analytically reconstruct the tip or the sample's surface. Given that the recorded height image is essentially a convoluted surface resulting from the interaction of the tip/sample-surface interaction shown in Figure 4-5, knowing the shape of one of these two surfaces the other one can be found through deconvolution. In this study, the reconstruction of the tip shape was done by imaging a calibration grating consisting of sharp Si spikes of known geometry (TGT-1, NT-MDT; cone angle 50°).

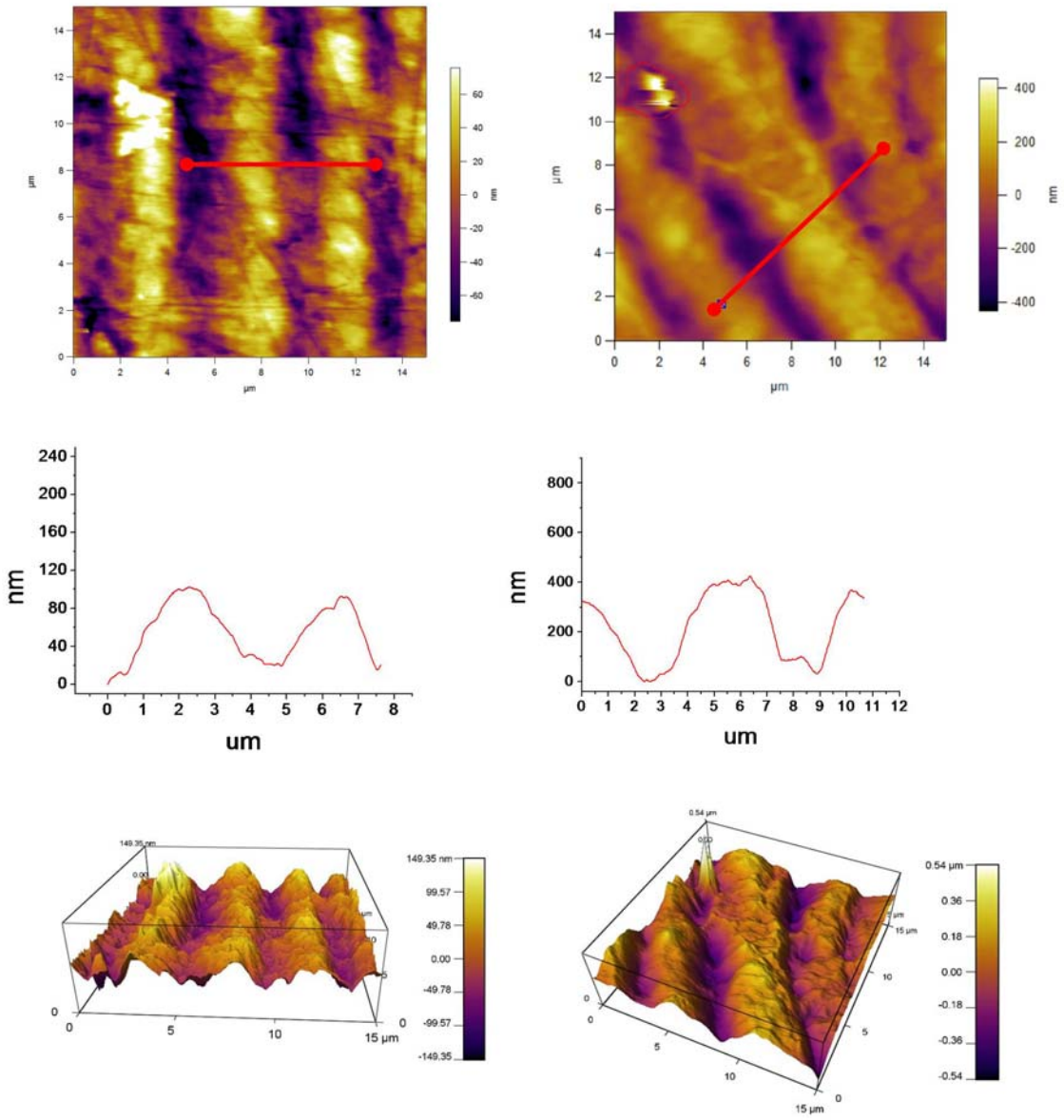

Figure 4-3: Figure showing the topographical and gray level variation of lamella – interlamellar area. Interlamellar areas are typically ~ 1 μm thick while lamellae vary from 5 -10 μm. Because of the low resistance of interlamellar areas against wear they always appear lower than lamellae. In both perpendicularly and parallel cut samples. Top: height AFM images of an osteon cut parallel (left column) and perpendicularly (right column) to the Haversian canal. Middle: profile analysis across the red profile-line depicted in height images. Bottom: 3D reconstruction of the same areas highlighting the hypsometric difference between lamellae and interlamellar areas.

On AFM Force Measurments the actual force is calculated on the basis of Hook's law (F = −kx) where "k" is the cantilever spring constant and "x" the flexion [*Meyer and Amer 1988*]. These two values are intrinsic properties of cantilever and an estimated value is provided by the manufacturer. However the provided values could differ significantly from the real ones. Thus, the accurate determination of each cantilever's "*k*" value is necessary. This can be done from the AFM software built-in routines by analysing the thermal vibration (noise) spectrum of the free vibrating cantilever. The final "k" value is calculated by an algorithm using the Equipartition Theorem [*Butt and Jaschke 1995*]; Asylum Research MFP-3D manual].

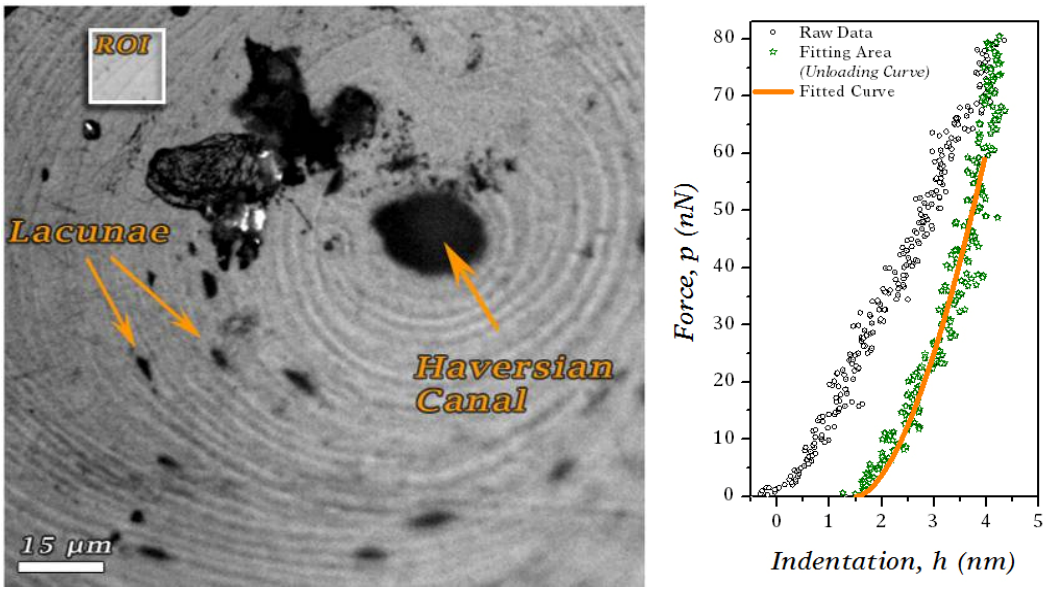

Figure 4-4: Optical microscopy image of a single osteon and localisation of the ROI selected for the indentation experiments in respect to Haversian canal. The lamination structure, the Haversian canal as well as the lacunae are also pointed out. The load direction was parallel to the scale bar. A typical Force – Indentation curve obtained from the ROI is also presented. The unloading part (green stars) of the Force – Indentation curve (black circles) was selected for the analysis and the h_f for the calculation of E_r was approximated from the fitted curve (orange line) according to the Oliver-Pharr model.

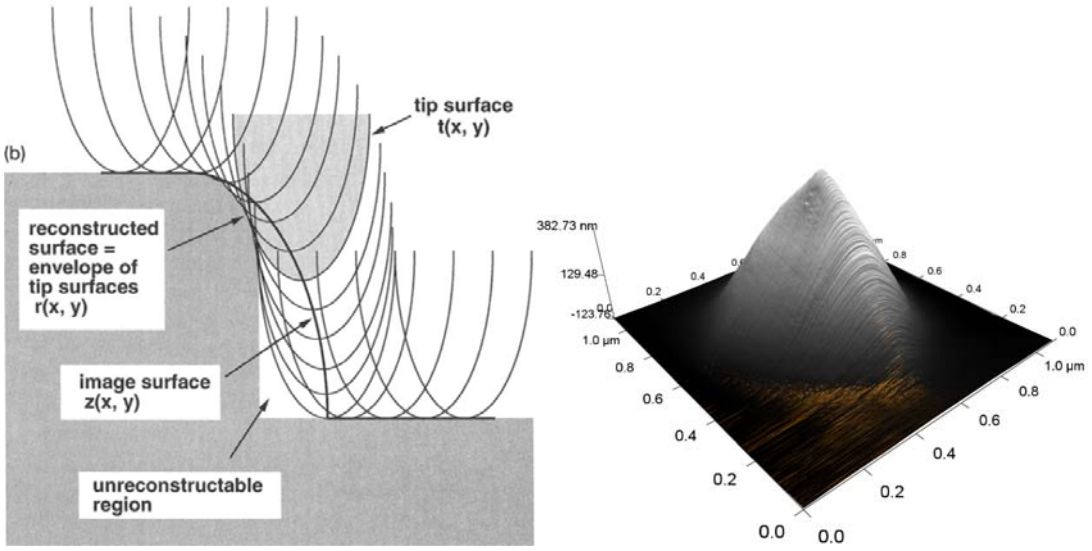

Figure 4-5: (left) tip-sample interaction and the resulting height image (adapted from [*Keller and Franke 1993*]); (right) 3D reconstruction of AFM cantilever's tip

The final calibration step involves the conversion of the deflection voltages measured from photodiode into a distance. In this case the "optical level" method was used to measure the deflection of the cantilever. The method's sensitivity can be determined by measuring the "Inverse Optical Level Sensitivity" or InvOLS. InvOLS is related with the needed "x" value as follows:

$$x = InvOLS \cdot \Delta V \tag{5.1}$$

where $\triangle$V is the voltage measured by a position sensitive detector.

The InvOLS value is usually measured by performing a force curve on a glass microscopy slide. The glass slide is considered as an infinitely hard surface and as such, no indentation depth is achieved and thus the deflection in volts is equal to the Z piezo sensor displacement. The slope of the resulting force curve (cantilever deflection vs. distance) is the actual InvOLS. For the determination of InvOLS value, five different force curves were obtained and the slope was measured for each one of them. The gradient of the linear region of the retract signal was measured and the mean value of the five gradients was set as the cantilever's InvOLS.

Statistical analysis was performed in each data set by Wilcoxon rank sum test and the normality of the distribution was assessed by means of Kolmogorov–Smirnov test in MATLAB. The frequency histogram of the calculated Er values was constructed for each sub-osteonal feature and a multi peak distribution (convolution of two Gaussian peaks) was fitted on the plotted data (Origin v8.1; Northampton, Massachusetts, USA; OriginLab Corporation).

The displacement map of a selected region of interest (ROI) was generated in order to visualise the strain field within the ROI where the indentation measurements were taking place. First, AFM height images were acquired from the ROI (Figure 4-4) in AC mode in the unloaded as well as in the loaded state, extracted in lossless (.tif) format and enlarged in Adobe Photoshop CS5 (v12 x64) using the bicubic interpolation algorithm (from initial image size 512x512 to 2000x2000 pixels). The strain map was then generated by feeding both images into commercial digital image correlation software (Vic-2D 2009, Correlated Solutions, Columbia, SC, USA) by setting the subset size at 101 pixels and the step size to 1.

4.1.6 Micro-Raman Microscopy of Bovine Osteon

Similarly to engineered "elastomeric bearing pads" [*Kelly 2002*], interlamellar areas act as energy absorbers and protect bone from catastrophic failure. Therefore, the hypothesis that the "lamellar | interlamellar | lamellar" deformation mechanism is the microstructural level equivalent of the "mineralized collagen fibril | interfibrillar "glue layer" | mineralized collagen fibril" mechanism found at the nanostructural level [*Gupta et al. 2007*] was formulated. If this was true, it should be reflected in the composition and structure of the interlamellar areas, *i.e.* being enriched in NCPs as previously suggested [*Derkx et al. 1998*].

Compositional analysis and imaging was performed by means of μ-Raman microscopy (inVia Raman microscope, Renishaw, New Mills, UK) using a 532 nm laser line. A computer controlled XYZ motorized stage moved the sample by 0.5 μm after every acquisition until the whole 20 μm x 20μm Region of Interest (ROI) (Figure 4-6) was measured. The spectra were acquired by focusing the laser beam on the sample's surface via a x50 objective lens resulting in a spot size of ~ 500 nm (tightest theoretical beam diameter, $D = 2 \cdot \lambda / \pi \cdot N.A. = 451$ nm;

where λ is the wavelength of the incident light = 532nm; N.A. is the lens Numerical Aperture = 0.75). An exposure time of 2 seconds and a spectral resolution of 1 cm^{-1} was used in all cases. A total of 1600 spectra were recorded from the selected ROI which were then further processed in order the final map to be obtained.

Fluorescent background was removed from raw spectra in MATLAB (version 7.10 Natick, Massachusetts: The MathWorks Inc., 2010) using a modified 5th order polynomial fit algorithm [*Lieber and Mahadevan-Jansen 2003*] spectra were then smoothed for noise reduction and the intensity or the ratio of user defined Raman peaks were measured for every one of them. Finally, μ-Raman compositional images were reconstructed by assigning a grey level value to the measured intensity or ratio value.

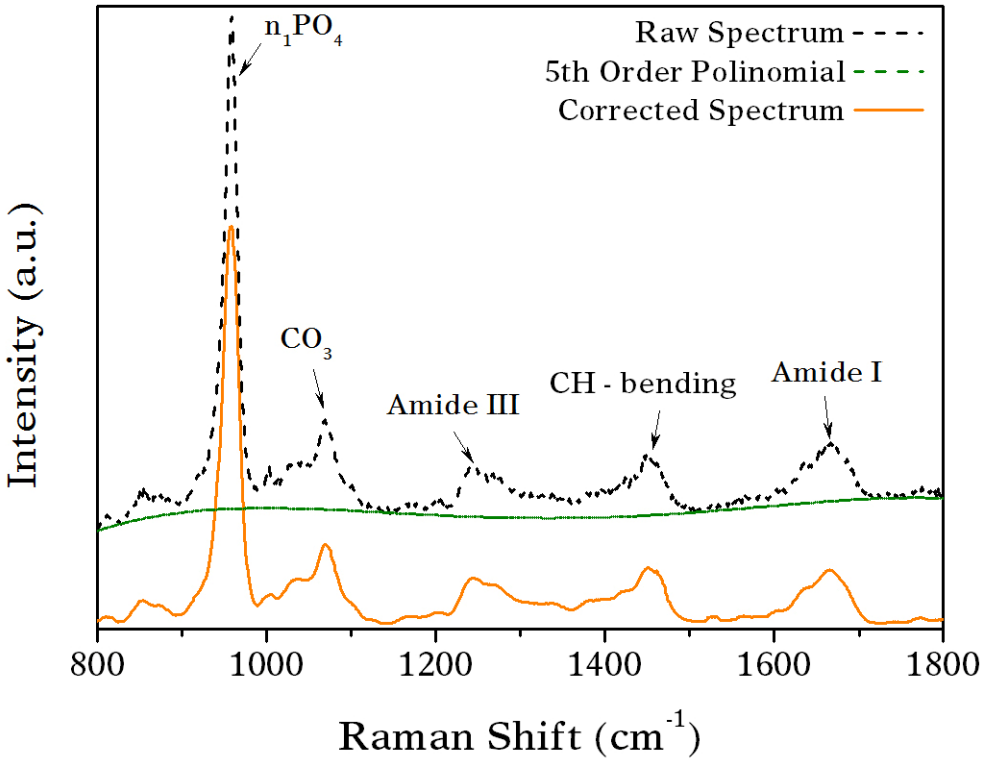

Figure 4-6: Typical spectrum obtained from the bone tissue. Black dashed line corresponds to raw spectrum while solid orange to the "corrected" one after the fluorescent background subtraction (green dashed line). The 5th order polynomial curve used as background was independently calculated for every single spectrum.

4.1.7 Surface demineralization

In addition to composition, orientation of mineralized collagen fibrils can also influence crack propagation. To uncover the underlying collagen structure polished bone surfaces were treated with 15 mmol EDTA[§§§] in 5 mmol, HEPES[****] buffer. EDTA dissolves the minerals that cover the collagen fibrils. The pH of the resulting solution was 9.5. A droplet of the solution was deposited on a sample surface where it was immobilized due to surface tension. After 360 s the sample was rinsed with ultrapure water and imaged with AFM in contact mode (Olympus - TR400PSA). Surface roughness was determined in regions of interest in the form of root mean square (R_{ms}) values using built in functions of the AFM control and analysis software (Asylum Research).

4.1.8 Statistical analysis

Statistical analysis was performed for each cantilever-based nanoindentation data set using a Wilcoxon rank sum test (significance threshold $p < 0.01$) and the normality of distributions was assessed by means of a Kolmogorov–Smirnov test in MATLAB® (version 7.10, The MathWorks Inc, Natick, Massachusetts).

Wilcoxon rank sum test, also referred to as Wilcoxon-Mann-Whitney rank test and Mann-Whitney U test, is a non-parametric, hypothesis test. It is commonly used for testing if two populations differ from each other by detecting differences between their median values. Wilcoxon rank sum test works by combining the data of the two populations and after shorting them rank them, i.e. replacing their numerical value with their rank. For two populations which come from the same underline population (null hypothesis) the rank values of each should spread throughout the range in a similar manner. If this is not the case, it means that the two populations come from different underline populations and the null hypothesis is rejected [*Roe 2001*]. In this study, Wilcoxon rank sum test was used because the moduli values were not normally distributed.

[§§§] Ethylenediaminetetraacetic acid

[****] (4-(2-hydroxyethyl)-1-piperazineethanesulfonic acid)

4.2 Results

4.2.1 Micromechanical Testing of Cortical Bone Samples Under Optical Microscope

Representative results of micromechanical test under the light microscope are presented in Figure 4-7. As it can be seen in these images, all the features of interest *i.e.* lamellas, interlamellar areas, Haversian canals and lacunae, are clearly evident. The initiation and the growth of the crack as well as its deflections onto the various osteonal features are also very well captured. The recorded Force – Displacement curve is dominated by the linear area (stage 4 – 9) which starts rising after the initial alignment area (Figure 4-7).

Images taken during the first seven steps showed that no crack initiation had taken place. The possibility of microcracking which is invisible under the optical microscope can not be secluded though. In fact, such a mechanism should be considered as a certainty [*O'Brien et al. 2003*]. At the final stages, the main crack starts from the weaker point of the notch (Figure 4-7- phase 9) where the stress concentration occurs, and grows perpendicularly to the loading direction. Also a crack within the bulk can be observed (Figure 4-7- Phase 9, white dot tailed arrow) indicating that the sample geometry does not cause stress concentration only on the notched point, but instead there are serious stresses concentrated close to the notch but within the bulk. Interestingly, the initial crack edge which was very close to a lacuna was "preferred" to deflect away from it and joined with the second crack instead of going through the lacunae. Also note that it didn't cross the previous lacuna (Figure 4-7– white hash) neither started by crossing the first one. In contrast, the preferable propagation path was almost from the middle of the two lacunae (Figure 4-7– dashed line). Finally, the crack is crossing almost all the lamellae vertically minimizing this way the crossing length. From the photographs one can safely state that the crack's preferable propagation path is from the interlamellar areas.

Unfortunately, the crack initiation and growth is too fast making impossible to capturing the deflection of the crack onto lamellas (Figure 4-7; white arrows) in a step-by-step basis. A much slower displacement rate could perhaps allow us to capture this phenomenon. Further displacement has caused unstable crack propagation (Figure 4-7; Phase 10).

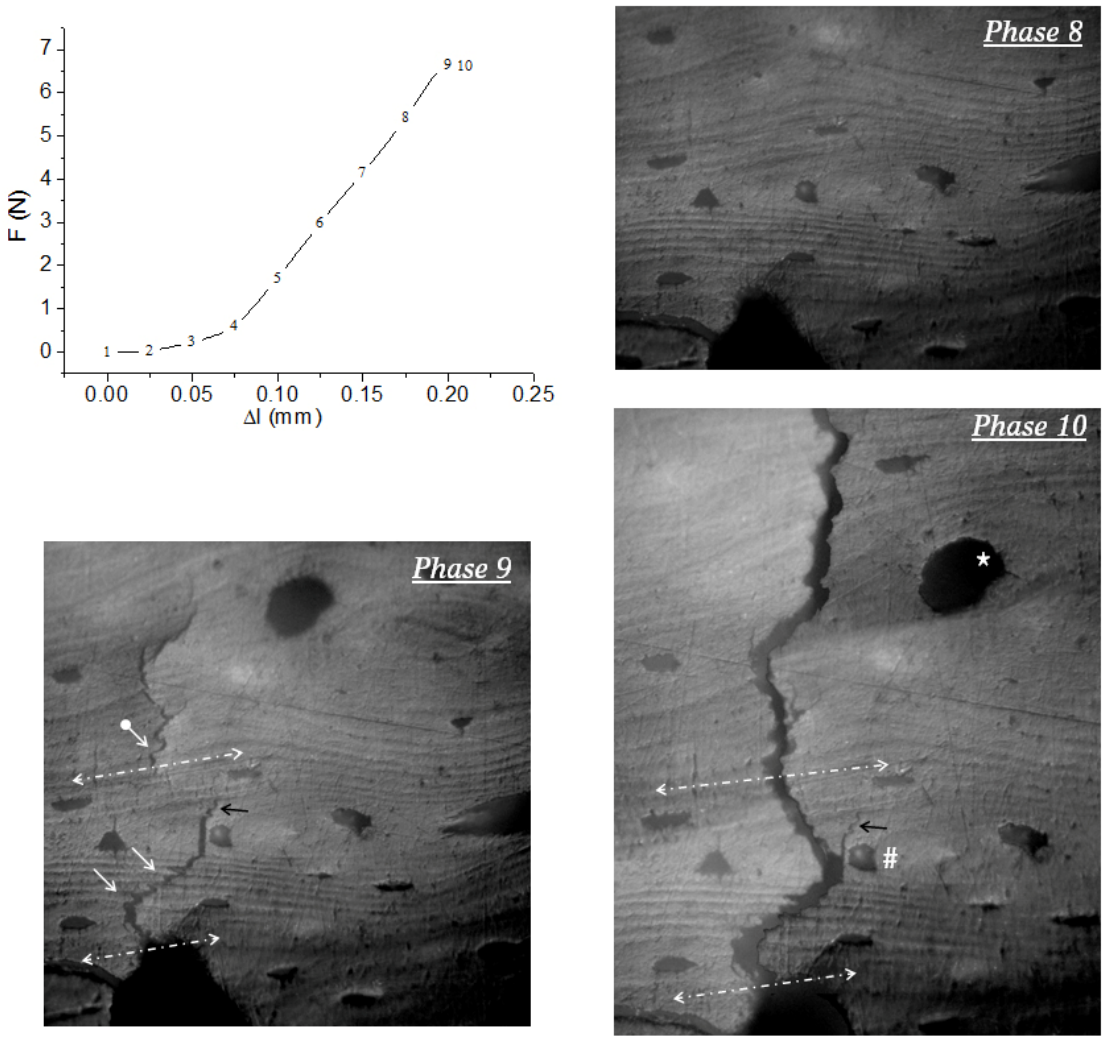

Figure 4-7: Representative results of micromechanical test under the light microscope. Phase numbers on the images correspond to the numbered points of the Force – Displacement graph. (top left) Force – Displacement curve recorded during the experiment. (top right) Loaded sample. No crack initiation observed (bottom left) Crack initiation. The crack starts from the notch where the stress concentration occurs, growing perpendicularly to the loading direction. (bottom right) Unstable crack propagation and failure of the specimen

4.2.2 In-Situ Micromechanical Testing of Cortical Bone Samples during AFM Imaging

The crack propagation within the osteonal features was imaged in a time-lapsed fashion by means of in-situ micromechanical testing during AFM imaging.

During the loading stages the samples' behaviour was identical to the ones presented in §4.2.1.

In contrast to the optical microscope images, AFM was able to detect the early micro-cracking (Figure 4-8 –bottom right) which developed vertically to the lamella's long axis like the previously described cracks in §4.2.1. Micro-cracking of bone under tensile loading (mode I) has previously been described by several authors [*Vashishth 2007*], and provides an energy dissipation mechanism which protects bone from catastrophic failure. This micro-cracking which for mode I loading takes the form of defuse damage, occurs at the level of mineralised collagen fibres in a length scale of ~1μm and involves the separation of these fibres under the effect of the load.

The assumption that lamellar interfaces provide a propagation path of least resistance have previously been reported [*Fratzl 2008a; Peterlik et al. 2005*], but to the best of my knowledge, this is the first time that stable crack propagation on this level (sub-osteonal, resolving bone micro- and nanostructure) has actually been captured.

Furthermore, at this level the glue-like NCP matrix located between these fibres is resisting the separation through the breakage of ion-mediated sacrificial bonds [*Fantner et al. 2007; Fantner et al. 2005a*].

These series of experiments reveal that cracks preferably propagate through interlamellar areas (Figure 4-8, Figure 4-9 and Supplementary Video 4-1), even when they are oriented perpendicularly to the principlal crack path and in-line with the crack-opening displacement. Once again, the crack is crossing almost all the lamellas vertically minimizing the crossing length (Figure 4-9). These results elucidate the important role of interlamellar areas for the fracture toughness of bone.

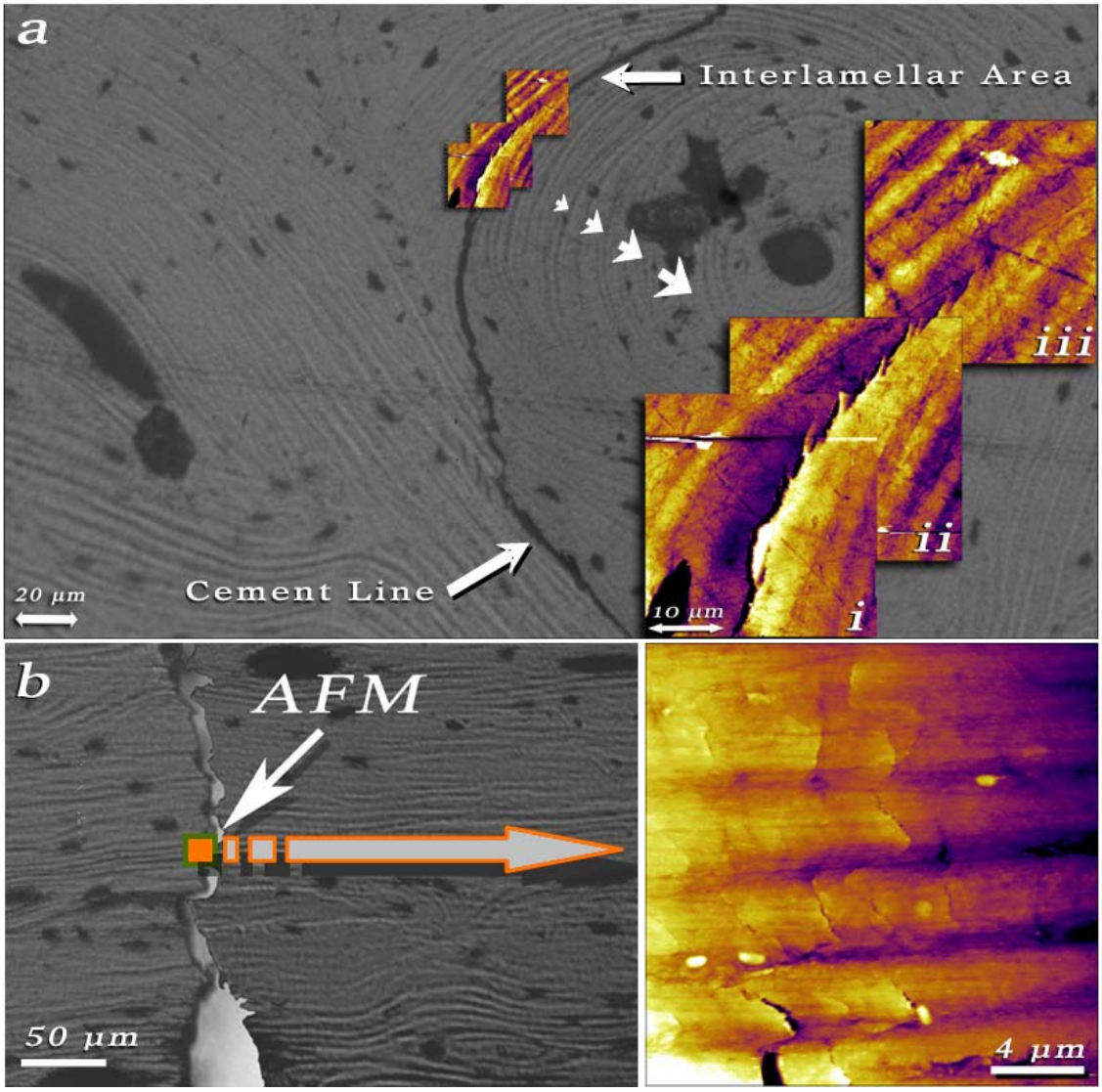

Figure 4-8: Cracks in cortical bone preferably propagate through cement lines and interlamellar areas (a & b). Inserts i, ii and iii in (a) are time-lapsed AFM images of stable crack propagation. Even when the orientation of the interlamellar areas is perpendicular to the principlal crack path and in-line with the crack-opening displacement (b), crack propagation through the interlamellar area requires less energy than crossing the lamella. As a result crack deflection patterns like the one depicted in picture (b) can be observed. Direction of the applied load is parallel to the horizontal edges of all figures

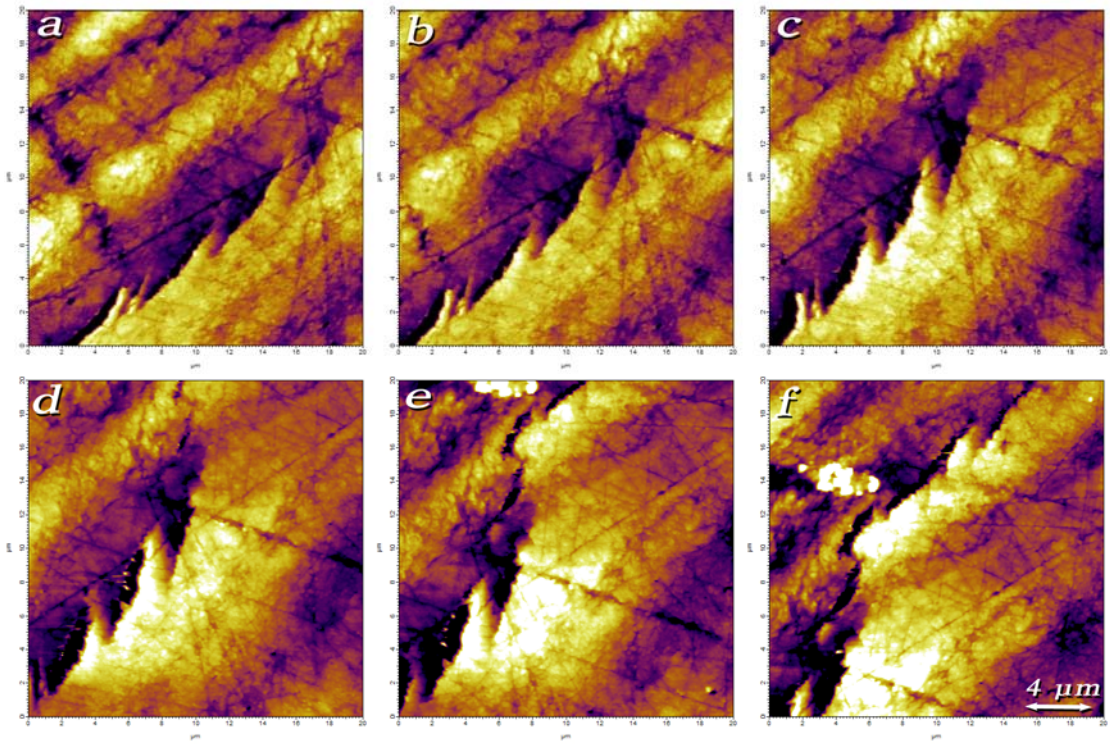

Figure 4-9: a – f time-lapsed AFM height images of crack propagation. a – c: the crack is opening; d: the crack is crossing the lamella perpendicularly minimizing the crossing path; e – f: the crack is deflecting on the subsequently lamella and continues its propagation through the interlamellar area.

4.2.3 Digital image correlation

Height (topographical) AFM images taken prior to- and at a loaded state were used to assess local strains by means of a digital image correlation (DIC) technique. As shown on the contour map of the principle strain 1 in Figure 3-10 and Figure 4-11, the interlamellar areas (noted with stars in Figure 4-11) take over a considerable amount of the applied strain. This phenomenon is presented in greater detail in Figure 4-10, where the different behaviour of lamellae and interlamellar areas under isostress and isostrain conditions are illustrated. In the first case (load perpendicular the long axis of the osteon), interlamellar areas gradually develop higher microstrains with increased load, while lamellae remain rather unaffected (Figure 4-10, Figure 4-11). This is not the case when loading is parallel to the osteons long axis (parallel plane). In this case, as the two microfeatures are under isostrain conditions, no difference in microstrain development can be seen between the lamellae and the interlamellar areas (Figure 4-10).

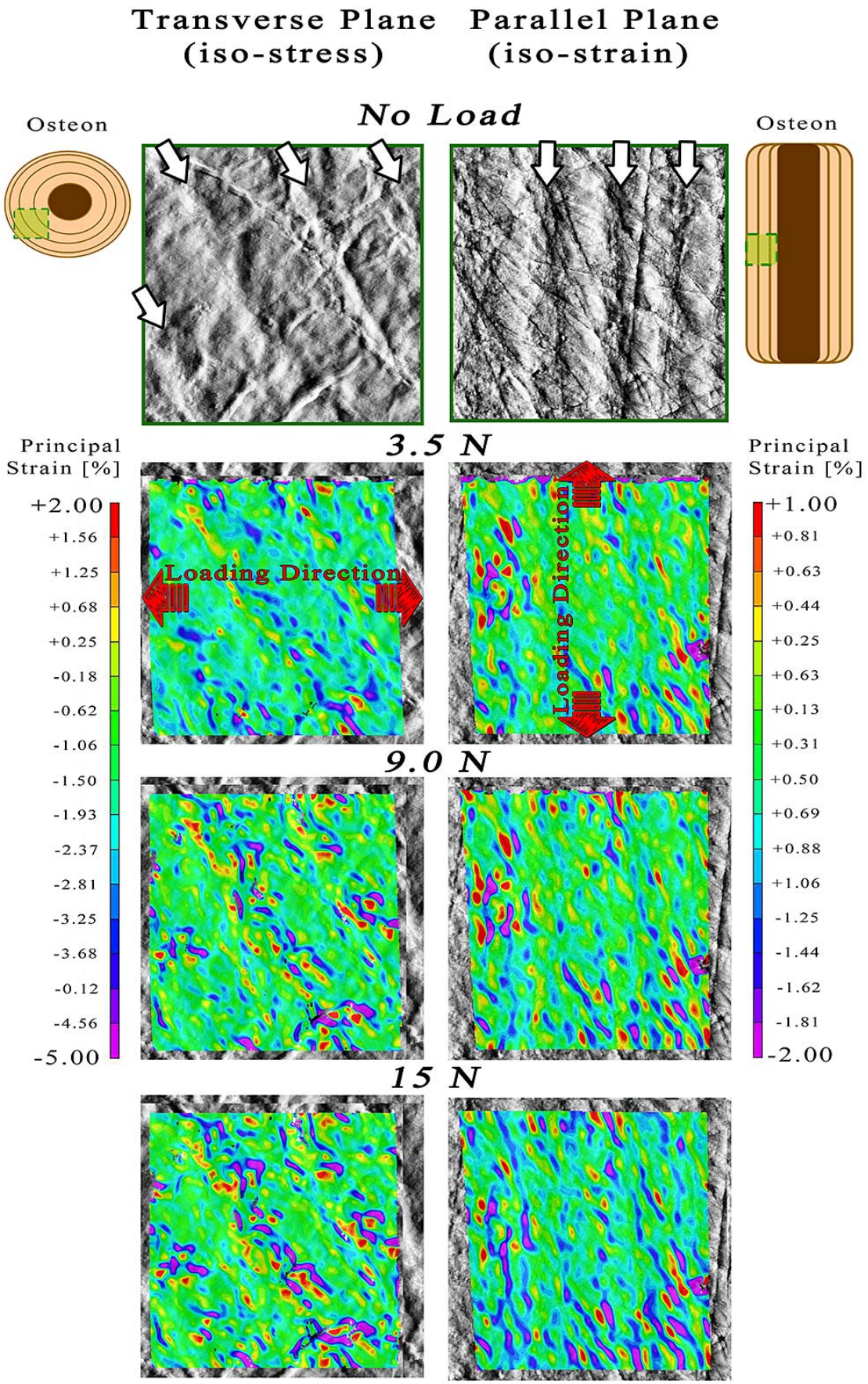
Transverse Plane
(iso-stress)
Parallel Plane
(iso-strain)
No Load
Osteon
Osteon
3.5 N
9.0 N
15 N
Loading Direction
Loading Direction
Principal
Strain [%]
+2.00
+1.56
+1.25
+0.68
+0.25
-0.18
-0.62
-1.06
-1.50
-1.93
-2.37
-2.81
-3.25
-3.68
-0.12
-4.56
-5.00
Principal
Strain [%]
+1.00
+0.81
+0.63
+0.44
+0.25
+0.63
+0.13
+0.31
+0.50
+0.69
+0.88
+1.06
-1.25
-1.44
-1.62
-1.81
-2.00

Figure 4-10: DIC analysis of bovine osteonal cortical bone for both isostress and isostrain conditions, with respect to lamellae and interlamellar areas. The specimen shown in the left column is cut in the transverse plane where the long axis of the osteon perpendicular to the specimen surface. The specimen shown in the right column is cut in the parallel plane with the long axis of the osteon parallel to the specimen surface. White arrows indicate the interlamellar areas and the red ones the load direction. In the case of isostress loading, higher strains are developed gradually on interlamellar areas with increasing load. This is not evident in isostrain loading where there is a more homogenous strain distribution along the lamellae and interlamellar areas. Window size 15 x 15 μm; resolution of AFM images 29 nm/pixel.

4.2.4 Cantilever-Based Nanoindentation of Loaded and Unloaded Bone Osteons and Digital Image Correlation studies

Cantilever-based nanoindentation measurements were carried out on lamellae and interlamellar areas in unloaded and tensile loaded conditions. The statistical analysis of the nanoindentation moduli revealed a selective stiffening of interlamellar areas when loaded, which was not evident in lamellae. Measured modulus values are presented in Table 4-1 and Figure 4-11.c. It is important to note that the reduced modulus reported here are obtained at only a few nanometers depth and hence reflect the properties of individual collagen fibrils, nanocrystals and NCPs rather than bulk bone properties.

Table 4-1: Reduced modulus of lamellae and interlamellar areas in both loaded and unloaded conditions determined from cantilever-based nanoindentation

		Reduced Modulus (GPa)		
		Median	*Mean*	*SE of Mean*
Unloaded	*Lamella*	1.89	2.13	0.05
	Interlamellar Area	1.47	1.79	0.06
Loaded	*Lamella*	1.95	2.67	0.09
	Interlamellar Area	2.10	2.79	0.08

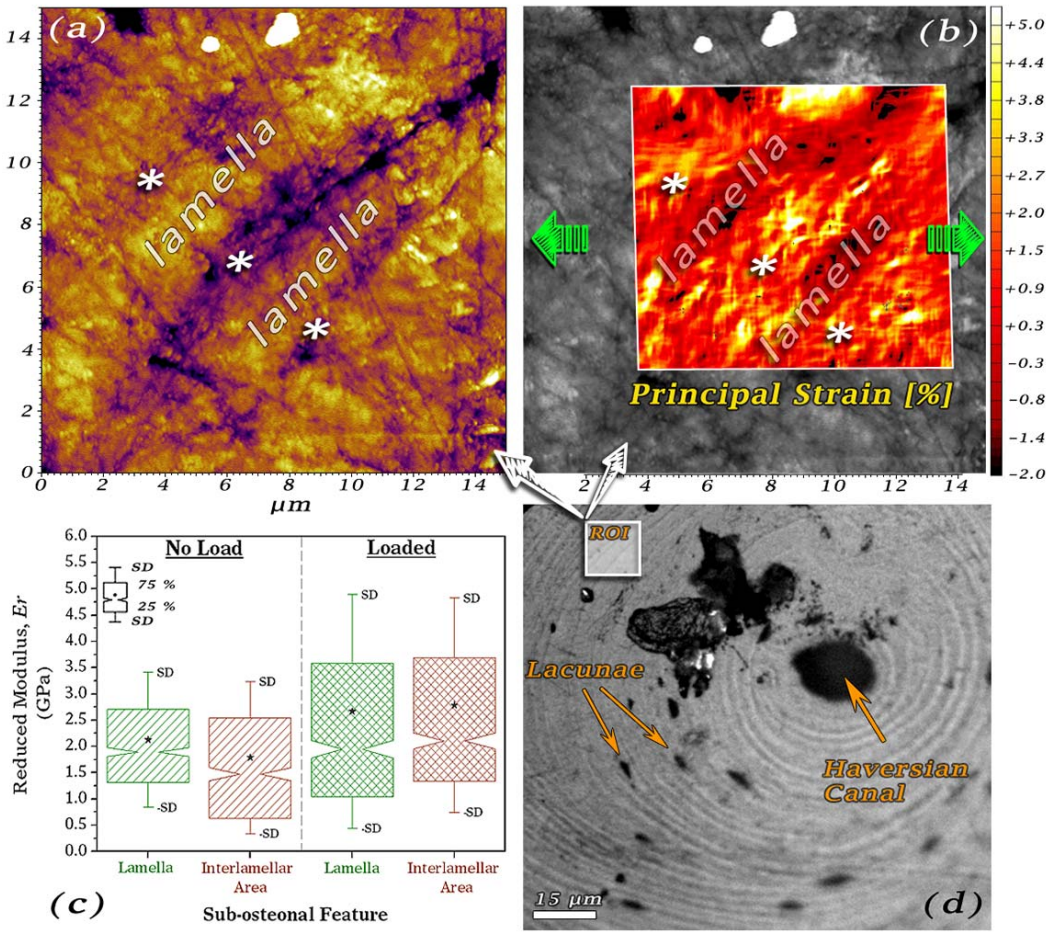

Figure 4-11: (a) AFM height image of part of an osteon where indentation measurements were carried out. Interlamellar areas are denoted with stars (*); resolution 29 nm/pixel (b) Contour map of principle microstrains (e_1) induced by loading the bone sample, the loading direction is indicated by the green arrows. Higher microstrains appear upon the interlamellar areas revealing their elastomeric bearing–like behaviour under tension. (c) Reduced moduli obtained from the force/indentation curves for the two sub-osteonal features. With no load present, lamellae exhibit significantly higher modulus (*Er*) than interlamellar areas (p-value <0.01). Loading the tissue eliminated the difference between the moduli (*Er*) of lamellar and interlamellar areas with interlamellar areas being marginally stiffer than lamellae, i.e. resulting in a selective stiffening of the latter during loading. (d) Optical microscopy image of a single osteon and localization of the ROI selected for the indentation experiments.

Without any load acting on the sample, lamellae showed a significantly higher reduced modulus in comparison to interlamellar areas (p-value <<0.01). Applying a tensile load resulted in a significant increment of the measured reduced modulus (E_r) of interlamellar areas (p-value <<0.01), while the modulus of lamellae showed a similar but insignificant trend (p-value > 0.01). Loading also reversed the significant difference between the two moduli (p-value >0.01); with interlamellar areas being stiffer than lamellae, revealing a selective stiffening of interlamellar areas.

Due to the nanometre-size tip radius and the shallow indentation depths applied, the cantilever-based nanoindentation experiments probe the mechanical behaviour of mineralized collagen fibrils and their surrounding mineralized NCP matrix. Under load, mineralized collagen fibrils are pulled apart, exposing the stretched NCP matrix to the tip. Consequently, a longer tail towards higher *Er* values appears in both lamellar and interlamellar area distributions, which causes the stretching of the corresponding box plots (Figure 4-11.c).

At this point it is important to note that the moduli reported here are obtained at only a few nanometres depth (~ 3 –7 nm) and hence reflect the properties of individual mineralised collagen fibrils and mineralised NCP matrix. Nevertheless, to ensure that the values measured by the technique are not under- or overestimations of the actual values of these components, two more experiments were conducted to serve as "controls". For this purpose two well characterised materials, that is Poly(methyl methacrylate) -(PMMA) and Polystyrene –(PP), were measured and analysed with the exact same experimental procedure used during the bone sample experiments. The analysis of the results for both materials returned values very close to the typical values reported in the literature for both PP [*Pukánszky et al. 1997*] and PMMA [*Jee and Lee 2010*]. These results are presented in Figure 4-12.

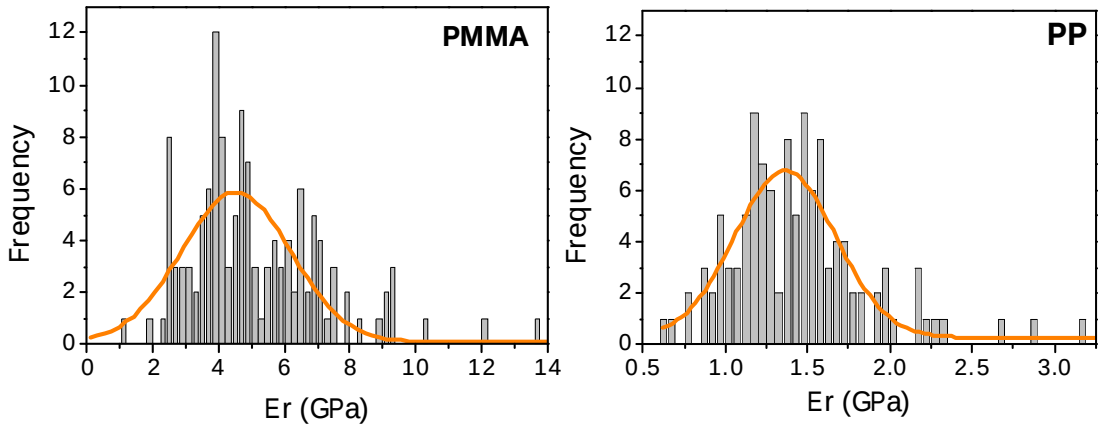

Figure 4-12: Results of control AFM cantilever-based nanoindentation experiments on PMMA and PP. A mean reduced modulus of (4.5 ±0.14) GPa and (1.36 ±0.02) GPa was obtained for PMMA and PP respectively.

4.2.5 Micro-Raman Microscopy of Bovine Osteon

μ-RAMAN microscopy revealed that, in fact, interlamellar areas are collagen-deficient and NCP-rich. Figure 4-14 shows the peak intensity maps of (a) the Amide I (C = O stretching vibration) [*Movasaghi et al. 2007b*] which mainly corresponds to the collagenous matrix [*Kazanci et al. 2007*], (b) the ν1PO4 vibrational mode of the mineral compound, (c) the C-H – bending which corresponds to both collagen and NCPs [*Kazanci et al. 2007*] and finally (d) the ratio of Amide I / C-H – bending. Given that Amide I is almost exclusively due to the collagenous matrix, while both collagens and NCPs are contributing to the C-H – bending intensity [*Kazanci et al. 2007*], the ratio value of these peaks serves as a measure of their relative concentrations. Higher ratio value means higher collagen or lower NCP concentration and vice versa. Importantly the results presented here show that interlamellar areas exhibit both a decrease in Amide I intensity as well as in the Amide I / C-H – bending ratio implying that they are collagen deficient and NCP-rich. A rather surprising fact is that no difference was detected on the degree of mineralisation between lamellae and interlamellar areas, meaning that, in this level, mineral concentration is not the influencing factor in guiding crack propagation. Interestingly, μ-RAMAN maps also uncover underlying canalicular structures, not visible using the optical microscope.

At this point it is important to note that the Amide I peak is not only dependent on collagen concentration but also orientation [*Kazanci et al. 2006; Kazanci et al. 2007*]. Lying or standing of collagen fibrils could modulate the signal intensity especially when a polarized laser is used. Figure 4-13 depicts the chemical structure of a collagen molecule. As previously mentioned, Amide I band is mainly due to C = O - stretching vibration. Looking at the scheme of Figure 4-13 one can see that C = O and C-H bonds are oriented perpendicularly to the long axis of the molecule result higher scattering intensity in this orientation.

Nevertheless, it should be mentioned that (a) to minimize any orientation effect at the signal intensity a non-polarised laser light was used for these experiments; (b) any orientation artefact should be affecting equally Amide I and C-H vibration modes as they are both oriented perpendicularly to the collagen's backbone; and (c) any contribution from the NCP residuals should be orientation independent as these proteins are randomly oriented in a mesh-like matrix.

However, control experiments, in which μ-RAMAN imaging was done on a parallel section with respect to osteon long axis, were also conducted to account for any orientation artefacts. In these samples the collagen fibrils located in interlamellar areas were rather standing than lying. The results are presented in Figure 4-15 and revealed a similar drop in intensity in the interlamellar areas.

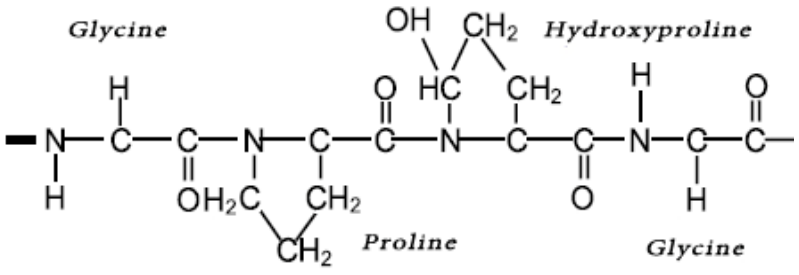

Figure 4-13: Chemical structure of collagen molecule. C = O and C -H bonds are oriented perpendicularly to the long axis.

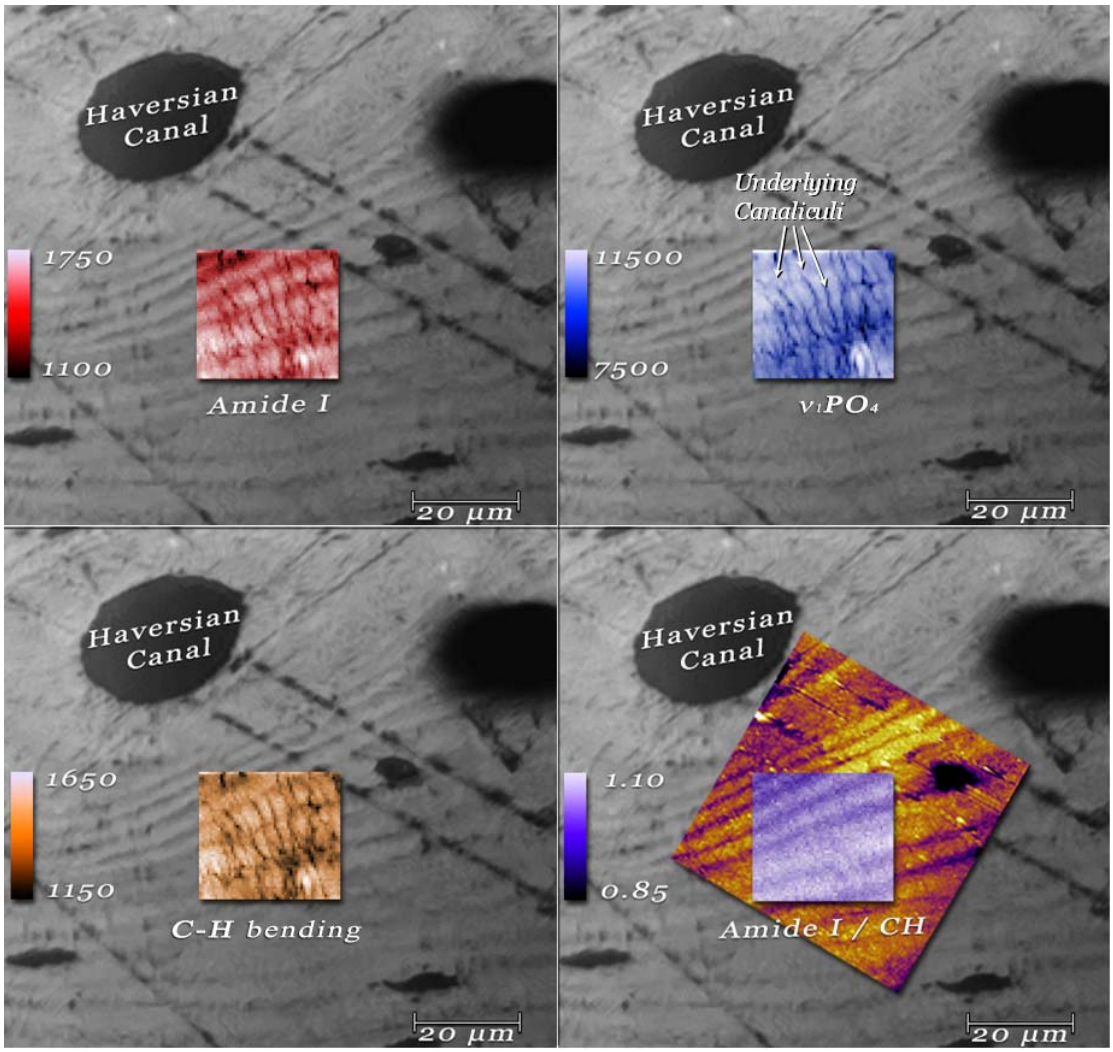

Figure 4-14: Superposition of µ-RAMAN intensity maps of Amide I , v1 PO4, C-H –bending and Amide I / C-H – bending ratio on light microscopic images. Superposition of AFM image is also presented in Figure (d). The lamellar structure is clearly visible on µ-RAMAN maps of both (a) and (d) demonstrating collagen deficiency in interlamellar areas. The intensity variation/contrast between lamellae and interlamellar areas of C-H –bending in picture (c) is less vivid. This implies that despite the collagen deficiency in interlamellar areas other biomolecules (i.e. NCPs) with C-H bounds are present in these areas giving rise to the C-H –bending vibration mode intensity. This is better denoted in picture (d) which maps the ratio of Amide I over C-H – bending. Most importantly no significant difference on degree of mineralisation between lamella and interlamellar areas can be seen in picture (b). The only contrast present is the one which corresponds to the underlying canaliculi.

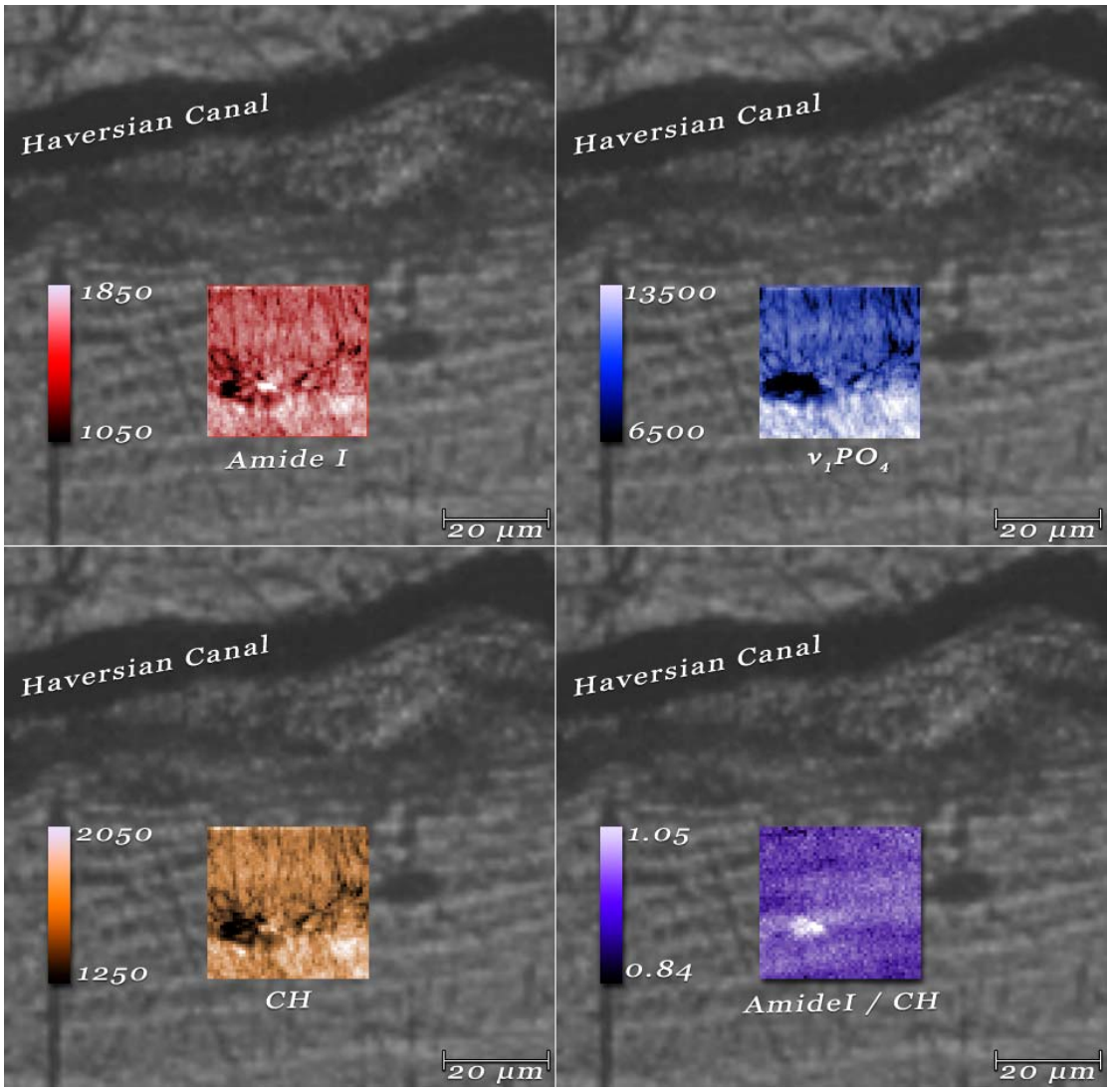

Figure 4-15: Superposition of μ-RAMAN intensity maps of Amide I, v_1PO_4, C-H –bending and Amide I/C-H –bending ratio on light microscopic images for a longitudinally cut sample. Despite the increased intensity due to collagen orientation, the lamellar structure of osteon is apparent in Amide I over C-H -bending map. Same as before, the lamination is less vivid in C-H –bending and no difference can be noted in the v_1PO_4 maps

4.2.6 Surface demineralization

In addition to composition, the orientation of mineralized collagen fibrils can also influence crack propagation. To uncover collagen fibril orientation, samples were treated with ethylene-ediaminetetraacetic acid* (EDTA). AFM imaging of EDTA-treated surfaces revealed the underlying microstructure, i.e. osteocyte lacunae, the canalicular network, as well as the interlamellar areas, as shown in Figure 4-16. These experiments show that interlamellar areas are clearly distinct features compared to lamellae, in terms of structure and morphology. In these areas collagen fibrils appear to develop circumferentially around the Haversian canal in contrast to the lamellae where the fibrils have been reported to be arranged in cholesteric layers with respect to osteon long axis [*Wagermaier et al. 2006*]. Furthermore, lamellae appeared rougher than interlamellar areas after EDTA treatment (cf. Figure 4-16), due to predominantly vertical or standing orientation of collagen fibrils. Average roughness R_{ms} analysis on EDTA treated bone sample revealed a difference of 48.4% between lamellae and interlamellar areas, with lamellae being rougher ($R_{ms\_Lamellae}$ =66.2 ±9.3 nm / $R_{ms\_InterlamellarArea}$ =34.2 ±1.9 nm). Mineral removal in the interlamellar areas uncovered lying (rather than standing) collagen fibrils.

* $C_{10}H_{16}N_2O_8$

2-({2-[Bis(carboxymethyl)amino]ethyl}(carboxymethyl)amino) acetic acid

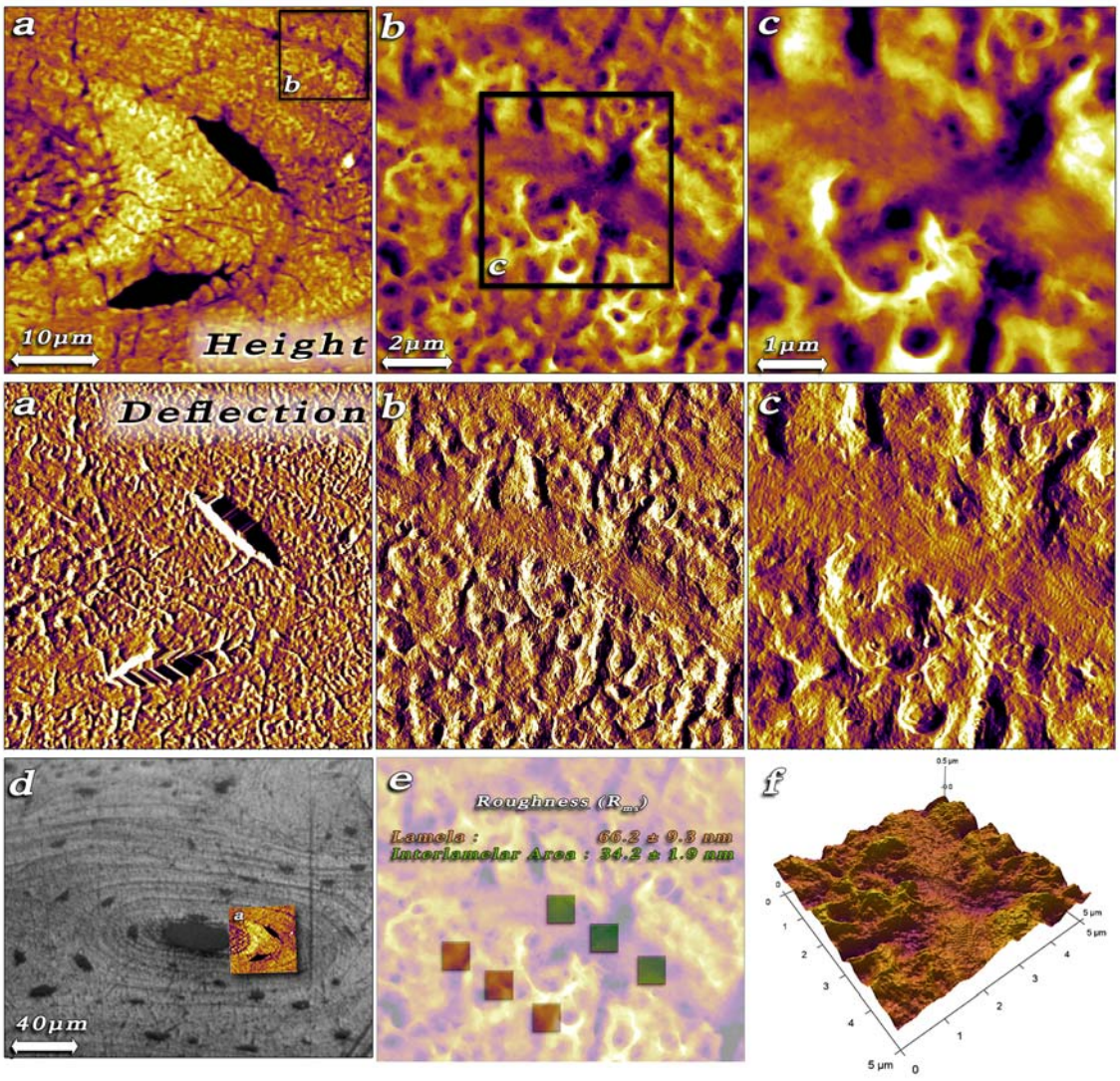

Figure 4-16: (a–c top: height channel, a–c middle: amplitude channel) AFM images of the EDTA-treated osteon reveal micro-structural features such as osteocyte lacunae, the canalicular network and lamellar interfaces. (d) Localisation of the AFM imaged area with respect to osteonal canal. (e) Roughness analysis of lamella (red boxes) and interlamellar areas (green boxes). Rougher lamellar surface is most likely due to predominantly vertical or standing orientation of collagen fibrils. In contrast, collagen fibrils appear lying circumferentially with respect to the long axis of the osteon within the interlamellar areas. (f) 3D reconstruction of c. On the interlamellar area, note the absence of crater-like structures present in lamellae which correspond to standing fibrils from which the interfibrillar mineralised matrix have been removed. Also note the lying collagen fibrils, with the characteristic 67 nm banding

4.3 Discussion

Here, via *in situ* mechanical testing during AFM and light microscopy, it was shown that crack propagation in cortical bone preferentially occurs in interlamellar areas (Figure 4-8, Figure 4-9). The assumption that lamellar interfaces provide a propagation path of least resistance has previously been reported [*Fratzl 2008a; Jepsen et al. 1999; Peterlik et al. 2005*]. However, to the best of my knowledge, stable crack propagation on the sub-osteonal / lamellar level, resolving bone micro- and nanostructure, has not been captured so far. Cantilever-based nanoindentation experiments revealed that these interlamellar areas are more compliant compared to lamellae, and stiffen selectively under tensile load as shown in Figure 4-11. Image analysis (DIC) revealed that there is higher deformation accompanying this stiffening process (Figure 4-10). Chemical treatment and AFM imaging revealed a change in collagen orientation in the interlamellar areas (Figure 4-16), where fibrils are developed circumferentially around the Haversian canal. This is in contrast with the lamellae, where the fibrils have been reported to be arranged in cholesteric layers with respect to the osteon long axis [*Wagermaier et al. 2006*]. Furthermore, a lower content of collagen and/or a higher content of NCPs is determined by means of μ-Raman imaging (Figure 4-14 and Figure 4-15) on these areas.

Bone toughening mechanisms have been the focus of bone research for many years. To date, the remarkable fracture resistance of bone tissue has been attributed to numerous toughening mechanisms, load bearing and energy dissipation mechanisms among them, spanning all bone hierarchical levels [*Gupta et al. 2006b; Peterlik et al. 2005*]. On the molecular level, stretching of the NCP meshworks results in the breakage of ion-mediated bonds between the NCP molecules [*Gupta et al. 2006b*]. Zappone et al. show that this mechanism can dissipate considerable amount of energy [*Zappone et al. 2008*]. This mechanism is also present in bone on the nanoscale; the NCP meshwork/matrix acts as an adhesion medium between mineralized collagen fibrils dissipating energy in a similar manner, and facilitating load transfer between the subsequent fibres [*Gupta et al. 2006b; Gupta et al. 2005*]. It has been estimated that less than 1% per weight of this matrix ("glue") is enough to provide bone with its known yield strength (~150 MPa) [*Fantner et al. 2005a*]. From the fractographic standpoint, it has been shown that cracks are

formed when these interfaces fail [*Thurner et al. 2009*]. Crack propagation, and consequently the fracture toughness of the tissue, is to a large extent affected by features of higher hierarchical levels, such as lamellae, interlamellar areas as well as cement lines and osteons. These features are responsible for a multitude of toughening mechanisms which include crack deflection and microdamage formation [*Peterlik et al. 2005*]. While the importance of load transfer mechanisms has been studied and discussed for the nanoscale, such mechanisms have not been reported or discussed for the osteonal and sub-osteonal level, which largely influence crack propagation [*Fratzl 2008a; Vashishth 2007*].

This study brings to light a load transfer mechanism between the sub-osteonal features of bone, which involves the cooperative deformation of "softer" interlamellar areas and "harder" lamellae and thereby dissipation of energy in a reversible manner. Sequential combination of hard and soft phase has previously been proven to reinforce toughness and strength of both nature and engineering materials [*Espinosa et al. 2011; Naraghi et al.*]. Similar structures, combining soft deformable materials with hard and rigid ones, can also be found in civil engineering structures. Elastomeric seismic isolation bearing pads are commonly used to protect structures, like buildings or bridges, from catastrophic failure when relative translation and/or rotation of the structure/deck against the ground are needed. The deformation of the elastomeric bearing pads protects the structure by accommodating movement while also dissipating energy [*Kelly 2002; Nakashima et al. 2004*]. In an analogous way, the NCP-rich interlamellar areas -*soft phase*- assist the transfer of load between sequential lamellae acting as elastomeric, or perhaps even as, "elasto-plastic" bearing interfaces. Obviously the effect in bone is much less dramatic compared to a combination of concrete and rubber – yet it is very likely to be an important contributor to toughness. We propose that the "lamella | interlamellar area | lamella" deformation mechanism is the microstructural level equivalent of the "mineralized collagen fibril | interfibrillar "glue layer" | mineralized collagen fibril" mechanism found at the nanostructural level [*Gupta et al. 2007*]. It is important to note that the microscale mechanism relies on the combination of changes in composition as well as structure in interlamellar areas and depends on the properties and interplay of all constituents of bone matrix, i.e. mineral, collagen and NCPs. The induced strain is taken over by the NCP-rich (and collagen-deficient)

interlamellar areas, by means of a multilevel mechanism, and it is transferred along the sequential lamellae. In the sub-osteonal level, the looser packing of mineralized collagen fibrils allows interlamellar areas for larger deformations (Figure 4-10) and is also the reason why these interfaces are found to be more compliant than the lamellae [*Gupta et al. 2006a*]. On the nanoscale, the interfibrillar NCP meshwork between the loosely-packed collagen fibrils are stretched apart, also stretching the interfibrillar NCP matrix (Figure 4-17).

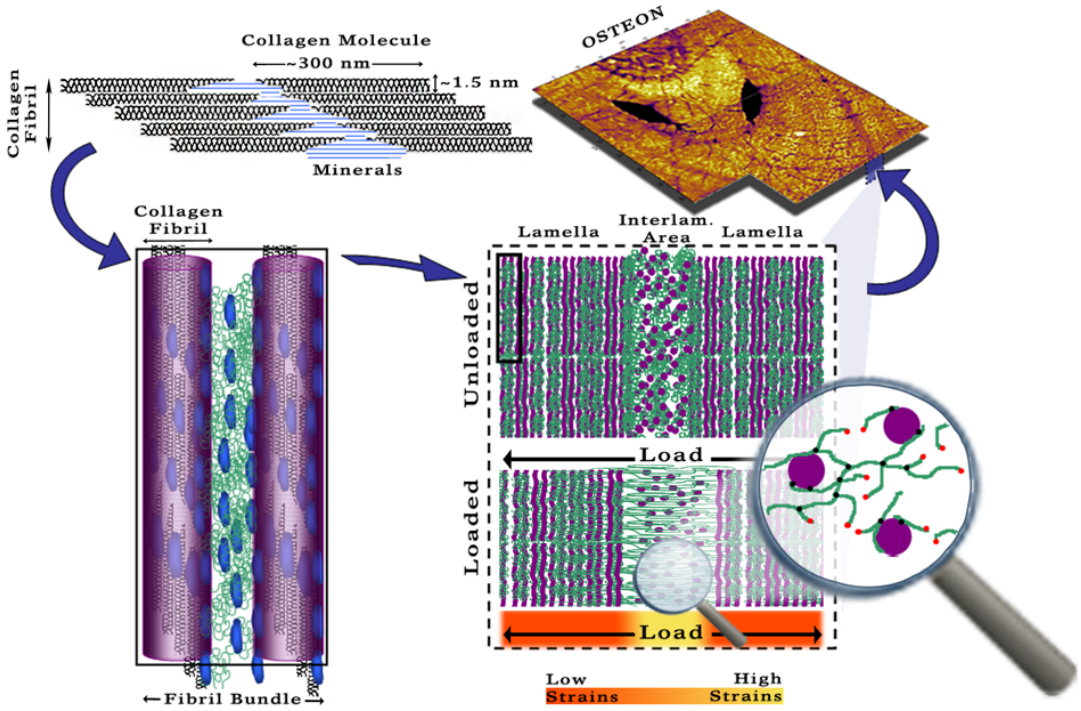

Figure 4-17: Proposed bottom-up model of a mammalian osteon. Mineralized collagen fibrils, glued together via a mineralized NCP "glue layer", are the building block of both lamellae and interlamellar areas. Upon tension, interlamellar areas are taking over a larger amount of the applied strain. There, the NCPs, filling the space between the loosely packed collagen fibrils, are stretched apart and sacrificial bonds (black dots - magnifying glass) start breaking (red dots - magnifying glass), releasing more hidden length. This mechanism (a) could dissipate significant amount of energy, (b) allow small deformation between lamellae and (c) is reversible. This would allow osteons to withstand various modes of micro-deformation, without crack formation, propagation or failure, while at the same time dissipating energy via a reversible mechanism.

This "lamella | interlamellar area | lamella" deformation mechanism and its compositional and structural origin also explains why interlamellar areas appear to have a lower reduced modulus (E_r). This difference becomes marginal when bone is under load, i.e. when pulling apart the mineralized collagen fibrils, "exposing" the stretched inter-fibrillar NCP meshwork to the tip (supplementary Figure S5). Thus, a higher reduced modulus, in comparison to the unloaded case, is observed. During the stretching of the interlamellar areas, likely sacrificial bonds within the NCP meshwork are breaking, exposing hidden length [*Fantner et al. 2005a*]. This would aid in dissipation of energy, based on entropic elasticity rather than elastic energy, in the stretched interlamellar areas (Figure 4-17). After the elimination of the applied load, or upon crack closure, the NCP meshwork is relaxed and intra- and intermolecular NCP bonds could reform [*Fantner et al. 2007*], restoring the mechanical integrity of interlamellar area partly or even in full. This might be a way for osteons to allow and withstand various modes of micro-deformation without inducing damage.

Like articular cartilage [*Loparic et al. 2010*], bone is a nanocomposite material built from components with different mechanical properties (i.e. individual mineralized collagen fibrils and mineralized non-collagenous protein matrix). The nanometer-size tip radius (~7 –15 nm) of the AFM probes, used for cantilever-based nanoindentation, allows probing the mechanical behaviour of fundamental components of lamellae and interlamellar areas. This also explains why the moduli values reported here are an order of magnitude smaller than ones previously reported on the tissue level [*Szabó et al. 2011*]. Conventional nanoindentation assesses the overall feature behaviour of, for example, a lamella and its vicinity to the applied load [*Loparic et al. 2010*].

These results support the hypothesis that the increased bone fragility found in NCP deficient bones [*Thurner et al. 2010b*] could be due to the lack of such dissipation mechanisms; during failure, crack propagation is influenced by the laminated structure of the osteon [*Koester et al. 2008*] or lamellar bone, similar to hybrid composite materials [*Ming-Yuan and Hutchinson 1989*]. In tensile loading, crack growth predominantly occurs within the "soft" interlamellar areas. The concentric arrangement of "hard" lamellae into an osteonal structure deflects the transverse cracks from their path, in this way protecting the nerve and vessels enclosed in the Haversian canal [*Gupta et al. 2006a*]. Under

transverse compression (with respect to Haversian canal) extensive cross-hatched damage has been observed in the osteonal level, which at the single-osteon level consists of groups of intralamellar arc-shaped microcracks. These microcracks develop in areas of high shear, at approximately – 45^{o} and + 45^{o} from loading direction, and follow the curvature of lamellae [*Ebacher et al. 2011; Ebacher and Wang 2009*]. The softer and more deformable interlamellar areas appear to be able to withstand the introduced shear, maintaining their structural integrity and transferring load from one lamella to the other. Furthermore, while the less stiff interlamellar areas widen or are sheared upon complex load modes, they might also serve as a "shock absorbing" mechanism, storing elastic energy during impact via compression of the NCP meshwork.

With regards to the μ-RAMAN results presented, it is important to note that the Amide I peak is not only dependent on collagen concentration, but also orientation [*Kazanci et al. 2006*]. Lying or standing of collagen fibrils could modulate the signal intensity. However, control experiments, in which μ-RAMAN imaging was done on a parallel section with respect to osteon long axis, where the collagen fibrils are standing rather than lying, revealed a similar drop in intensity on the interlamellar areas (cf. Figure 4-15). Furthermore, it is known that Raman scattering intensity of hydroxyapatite is dependent on the c-axis orientation of the crystal [*Tsuda and Arends 1994*] and that the mineral crystals mainly lie with their c-axis parallel to the collagen fibrils [*Sasaki et al. 1989*]. Thus, if the observed intensity-drop was only dependent on collagen orientation, a similar drop should have been observed in v_1PO_4 vibrational mode of the mineral compound which is known to be highly sensitive to orientation direction [*Kazanci et al. 2006; Kazanci et al. 2007*]. Such a drop is not evident in the v_1PO_4 mode intensity maps suggesting that the drop observed in Amide I, is mainly due to concentration difference.

There are a few further experimental limitations of this study. In the case of micro-tensile experiments, bone samples were dry, which is known to significantly affect the elastic modulus and the stiffness of the tissue [*Hengsberger et al. 2002; Rho and Pharr 1999*]. However, bone failure behaviour has been reported to be governed by the same mechanisms in both dry and wet samples [*Braidotti et al. 2000a; Braidotti et al. 1997a*]. In more detail, despite the differences in energy absorption and ductility, both conditions exhibit fibre/matrix debonding and delamination-like failure. The

microtensile experiments presented here capture this very delamination phenomenon and confirm, in a time-lapsed fashion, that interlamellar areas indeed provide a preferential crack propagation path [*Peterlik et al. 2005*]. A similar argument could also be raised with respect to the cantilever-based nanoindentation results. I believe, though, that it is reasonable to consider the sample surface to be only partially dehydrated as (a) samples were immersed in PBS until the time when the experiments were conducted and (b) due to the presence of a water-film (condensed from the atmosphere) on the sample's surface. In addition, as interlamellar areas are NCP-rich, it should be expected that under physiological conditions they are more hydrated than lamellae [*Braidotti et al. 2000a*]. Thus, it may be that dehydration partially masks their selective stiffening behaviour, which may be more vivid under physiological conditions. The same stands for the Digital Image Correlation study as it is known that dehydration affects the "weak" lamellar interfaces which are playing a crucial role in the deformation mechanism [*Seto et al. 2008*]. The DIC results presented above only provide qualitative information about the strain distribution. Nevertheless, they confirm higher strain in interlamellar areas, which is also evident from displacement fields; further, more sophisticated experiments are required to reduce inherent issues such as scanner drift in the slow scan axis. Also, higher resolution and contrast AFM images could improve the resulted strain maps as they would enhance the salient features of the image used for the DIC analysis.

It is known, that apart from the hydration, that the mechanical properties of the bone also depend upon temperature [*Lakes et al. 1979; Smith and Walmsley 1959*]. Smith and Walmsley showed that in the temperature range between 10 - 43 ^{o}C the compliance of bone increases linearly with increasing temperature while Lakes and co-workers showed similar dependence of its viscoelastic properties. In this study, all bone samples where tested in ambient conditions at 25 ^{o}C. This is lower than the body temperature in which the bone is designed to operate and may affect the measured moduli of both lamellae and interlamellar areas. Yet this study focused on the related differences between the mechanical properties of lamellae and interlamellar areas and not on the absolute modulus value of these areas. Finally, it is important to note once more that this study was conducted on bovine cortical bone samples the microstructure of which is known to differ from human bone by being highly laminated with smaller amount of secondary osteons [*Smith 1960*]. None the

less, it should be stressed that all the experiments presented here were conducted on secondary osteons which is a feature that is similar on both human and bovine cortical bone. Further to this point, studies show that the deformation of long bones across species is not differing considerably [*Liebschner 2004*] thus it is reasonably one to expect analogous mechanical behaviour across the different mammalian species.

In summary, this study shows that lamellar interfaces, i.e. interlamellar areas, are features with compositional and structural differences from lamellae; they are collagen-deficient, NCP-rich and have different collagen fibril orientation in comparison to lamellae. Interlamellar areas act as crack guidance zones and deflectors. Additionally, they allow for micromotion in bone likely without permanent damage formation, partly similar to mechanisms found on the nanoscale. Structurally, from the nanoscale through the microscale and all the way up to the macroscale, bone adaptation to the complex biological loading conditions seems governed by hard/soft phase interaction, to achieve reversible elasto-plastic deformation prior to true damage formation. Small changes on the nano- or microstructural level disturbing the hard/soft phases, such as NCP deficiency in the bone tissue, due to age or disease could affect bone ability to propagate such mechanisms. This could lead to lowered fracture toughness and overall mechanical competence of bone.

Chapter 5

A Novel Videography Method for Generating Crack Extension Resistance Curves in Small Bone Samples

The study presented in this chapter has been submitted for publication in the Public Library of Science one (PLOS ONE) and it is currently under review. Preliminary results obtained from it have also been presented in the following conferences:

- ✓ Annual Meeting of the Orthopaedic Research Society (ORS), San Antonio TX, January 26 – 29, 2013 *(accepted abstract)*
- ✓ 20th Annual Meeting of European Orthopaedics Research Society (EORS), Amsterdam September 26-28, 2012

The interest in measuring fracture toughness behaviour of bone tissue is increasing within the bone research community as it is a quantitative way to evaluate an important bone quality parameter. Fracture toughness measurement techniques have been used in an increasing number of studies to quantify the fracture resistance of bone [*Malik et al. 2003; Nalla et al. 2005; Phelps et al. 2000; Vashishth 2004; Wang et al. 2002; Yan et al. 2007; Zimmermann et al. 2010; Zioupos and Currey 1998a*]. While these studies were able to provide a good estimate of bone fracture toughness in terms of the critical stress intensity factor (K_c) and/or the critical strain energy release rate (*J-Integral*), they were also pushing fracture toughness testing to the limit.

The method presented here, was developed to overcome the problem of measuring fracture toughness and crack propagation toughness in small bone samples. The need of such technique arose when a correlation study between

the properties measured at the osteonal level with and the ultimate toughness behaviour of the tissue was attempted on human bone samples. Due to the small cortical size of the human bone, samples cut perpendicularly to bones long axis were considerably small (typical dimension ~1mm x 1mm x 8-10mm) and as a result conventional fracture toughness measurements requiring tracking of the crack propagation were not applicable.

The experimental procedure for determining the crack extension resistance (*R*-curve or *J-R* curve) of a material requires the measurement of crack extension (Δa; $\Delta a = a_{(i)} - a_0$) that occurs during loading of a pre-cracked specimen [*ASTM 2004*]. In the case of sub-millimetre sized samples this is a very difficult task. To deal with this problem, two studies have used *in-situ* environmental scanning electron microscopy (ESEM) during three-point bending but these, to the best of our knowledge, where the only studies which were able to generate crack extension resistance curves for short (<600μm) crack propagations [*Koester et al. 2008; Nalla et al. 2003*].

In the next sections a new method for generating crack extension resistance curves in small bone samples, i.e. with cross-sectional dimensions of 1 mm x 1 mm or less, tested in three-point bending combined with videography will be presented. This approach is based on tracking crack front propagation via monitoring of the so-called "whitening zone", which develops in front of the crack tip. This approach tracks the crack propagation in an indirect fashion. Microcracking, is one of the intrinsic toughening mechanisms acting in front of the crack-tip during crack propagation in quasi-brittle materials like bone [*Evans and Faber 1984; Ritchie et al. 2009; Vashishth et al. 1997*]. The "whitening effect" is the result of increased light reflection on the surfaces of the newly formed microcracks within this damage zone [*Thurner et al. 2007*]. As the strain increases, some of the microcracks within the damage zone (also called frontal process zone [*Vashishth et al. 1997*]) join together and the main crack propagates. Subsequently, a new frontal process zone is developed ahead of the propagated crack-tip and the procedure repeats until the specimen fails [*Evans and Faber 1984; Vashishth et al. 1997*].

The main objectives of this study were (i) to quantify the correlation between the "whitening effect" and the crack propagation and (ii) to develop a computer-aided methodology to generate crack propagation resistance curves for fracture toughness evaluation of small bone specimens.

5.1 Material and Methods

5.1.1 Specimen preparation and testing

5.1.1.1 Rat tibiae (whole bone) samples:

The applicability of the method on small animal model studies was tested using two whole tibiae harvested from 28 day old rats. At this age, the tibia is approximately 2 - 3 mm in diameter and about 20 - 25 mm long. After removal of soft tissue using tissue tweezers and a scalpel, bones were mounted on a low-speed saw and both the distal and proximal ends were removed. Subsequently, bone marrow was removed and the posterior surface of the midshaft was notched using firstly a low-speed saw (IsoMet, Buehler, Lake Bluff, IL, USA) and secondly a razor blade and diamond suspension, as described by Kruzic et al [*Kruzic et al. 2005*]. The pre-notched samples were loaded in a three-point bending rig with a 10 mm span and submerged in Hanks' Balanced Salt Solution (HBSS) of pH ≈ 7.4. Force was applied at 0.01 mm/s to failure by the mechanical tester (ElectroForce3200, Bose, Eden Prairie, MN, USA) with the posterior, notched surface of the bone in tension Crack propagation was recorded using a high-speed camera (Ultima 512, Photron, San Diego, CA, USA) operated at 60 fps with two fibre optic lights (DC-950H, Dolan-Jenner, Boxborough, MA, USA) illuminating the specimen from approximately + 45^{o} and – 45^{o} from the camera field axis. The camera started recording simultaneously with the loading test initiation by the use of an external trigger. During the experiment "Force - Displacement" and "Force - Elapsed Time" channels were recorded. The "Force - Elapsed Time" channel was used to synchronize the high-speed video with the "Force - Displacement" using the Force as the reference point between the two channels. In more detail, as bending and videography experiments started simultaneously, the first point of the Force - Displacement curve corresponds to the first point of the Force – Elapsed Time. Since the recording frame rate is known the elapsed time for every subsequent frame can be calculated, thus associating it to the corresponding F, v of the event.

5.1.1.2 Human cortical bone samples

Four human femora (females; aged 43, 47, 80 and 83) were obtained from the International Institute for the Advancement of Medicine (IIAM) and stored at -

80 °C. A butcher's bandsaw (BG 200, Medoc, Logrono, Spain) and a low speed precision saw were used to cut the femora into single-edge notched three-point bend SE(B) specimens [*ASTM 2004*] (n = 10) of 0.8 - 0.9 mm width and height and 10 mm length oriented in the antiplane longitudinal orientation [*Launey et al. 2010*] (Figure 5-1). Toughness experiments were conducted using three-point bending as described above except that a bending rig with a span of 6.15 mm instead of 10 mm was used due to sample size limitations, and the tests were conducted using fully hydrated samples in air. To ensure hydration (i) all samples were submerged in HBSS for four hours before the experiments and only removed just prior to testing (ii) test time was kept in all cases at less than 1 min to prevent samples from drying out.

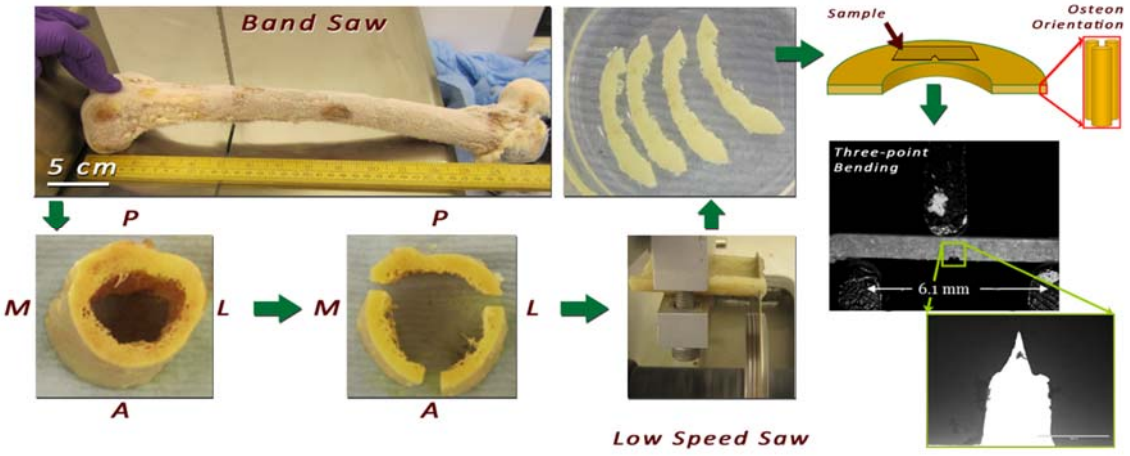

Figure 5-1: Miniature SE(B) sample preparation from a human femur

5.1.2 Whitening front propagation tracking

5.1.2.1 Calibration and pre-processing

To reduce the computational power required, one sample for every 15 frames is extracted from the video. After loading the frames and load-time-displacement data, the first video frame is used for interactive pixel size calibration. This is achieved by selecting the contact points of the bottom (left and right) supports to the sample surface. The distance between these points corresponds to a known distance of 6.15 mm (cf. Figure 5-1) and this process allows calculating displacement values independent of the video camera to sample distance. Next, a rectangular Region of Interest (ROI) surrounding the sample notch is selected for processing. Gamma correction and windowing is applied for video pre-

processing aiming to standardize the image appearance across the different frames.

5.1.2.2 Registration and Subtraction

A subtraction method is used to enhance the whitening effect on the video. This method works on a frame-by-frame basis. First the 1st image frame is registered to the current frame using a normalized cross-correlation method introduced by Guizar et al. [*Guizar-Sicairos et al. 2008*]. This is a rigid registration method which provides sub-pixel image registration without deforming the sample geometry. Next the difference image is calculated by subtracting the registered 1st frame from the current frame. The same process is then repeated for all frames and the propagation of whitening across the sample can be seen in the resulting subtraction video (Video 6-1, 6-2 and 6-3).

5.1.2.3 Whitening front propagation

The whitening front for each frame is automatically calculated from the corresponding difference image. The whitening region is identified by thresholding, while morphological opening with a structural element of 2 pixels in diameter is used to join neighbouring whitening regions together by removing small dark islands. The whitening front is defined as the maximum of the top-left and top-right extrema of the whitening region; that is the uppermost left and the uppermost right pixel of the binarised whitening area. The front displacement is calculated as the distance between the whitening front and the initial tip of the notch. The whitening front propagation-tracking algorithm is outlined in Figure 6-2 and an example dataset showing whitening progression is presented in Figure 5-4.

5.1.2.4 Quantification of correlation between whitening front- and crack propagation

The correlation between whitening- and crack-propagation was quantified using the whole rat tibiae. The notched midshafts were loaded in the three point bending configuration until the crack propagation became unstable and resulted in catastrophic failure, as described above. The whitening front propagation was evaluated using the described algorithm. Subsequently, each frame of the video was played back and the user was asked to manually select the beginning (i.e. pre-notched point) and the ending of the developed crack, which was much

better visible in recorded videos (cf. Figure 5-3 and video 6-3) compared to the small bone samples. Using this input the crack extension Δa_{crack} was calculated for each frame. The measurements were repeated five (5) times to account for intra-observer variability and the correlation of the resulting mean propagation values for both whitening front- and crack-propagation was tested using Pearson's correlation coefficient.

5.1.2.5 Calculation of J-integral and K_{eff}

The fracture behaviour of bone should ideally be evaluated using non-linear fracture mechanics, as extensive plastic deformation is taking place in front of the crack tip [*Ritchie et al. 2008; Yang et al. 2006*]. Especially for millimetre- and sub-millimetre-sized bone samples, this inelastic zone is often comparable to the sample size. The phenomenon is known as large-scale yielding [*Yang et al. 2006*]. In such a case the specimen's fracture toughness is best assessed by means of the J-integral [*Ritchie et al. 2008*]. Nevertheless, in the bone mechanics community it is more common to express bone fracture toughness in terms of the stress-intensity factor (K_c) [*Koester et al. 2008*], which is the equivalent toughness parameter for a linear elastic material [*Ritchie et al. 2008*]. K_{eff} can be calculated from *J-integral values* as described below.

For the human SE(B) specimens, fracture toughness was determined using the *J-integral* and K_{eff} using nonlinear-elastic fracture mechanics as described by Ritchie et al. [*Ritchie et al. 2008*] and ASTM standard E 1820 -01 [*ASTM 2004*]. In brief, *J* was given by:

$$J = J_{el} + J_{pl} = \frac{K^2(1-\nu^2)}{E} + \frac{2A_{pl}}{Bb} \tag{5-1}$$

where J_{el} and J_{pl} are the contributions of the elastic and plastic regions, respectively, *K* is the stress-intensity factor as defined in E 1820 -01 [*ASTM 2004*], ν =0.33 is the Poisson's ratio, *B* the specimen's thickness, *b* the uncracked ligament and A_{pl} the area under the force (N) *vs* plastic load-line displacement (mm) curve. *E* is the flexural modulus given by:

$$E_f = \frac{S^3 \cdot m}{4 \cdot B \cdot (W - a_0)} \tag{5-2}$$

Where S is the support span, B,W and a_0 the width, depth and the length of the notch respectively, and m the slope of the linear part of the load – displacement curve. The equivalent (effective) stress intensity was calculated from J using [11]:

$$K_{eff} = \sqrt{JE} \tag{5-3}$$

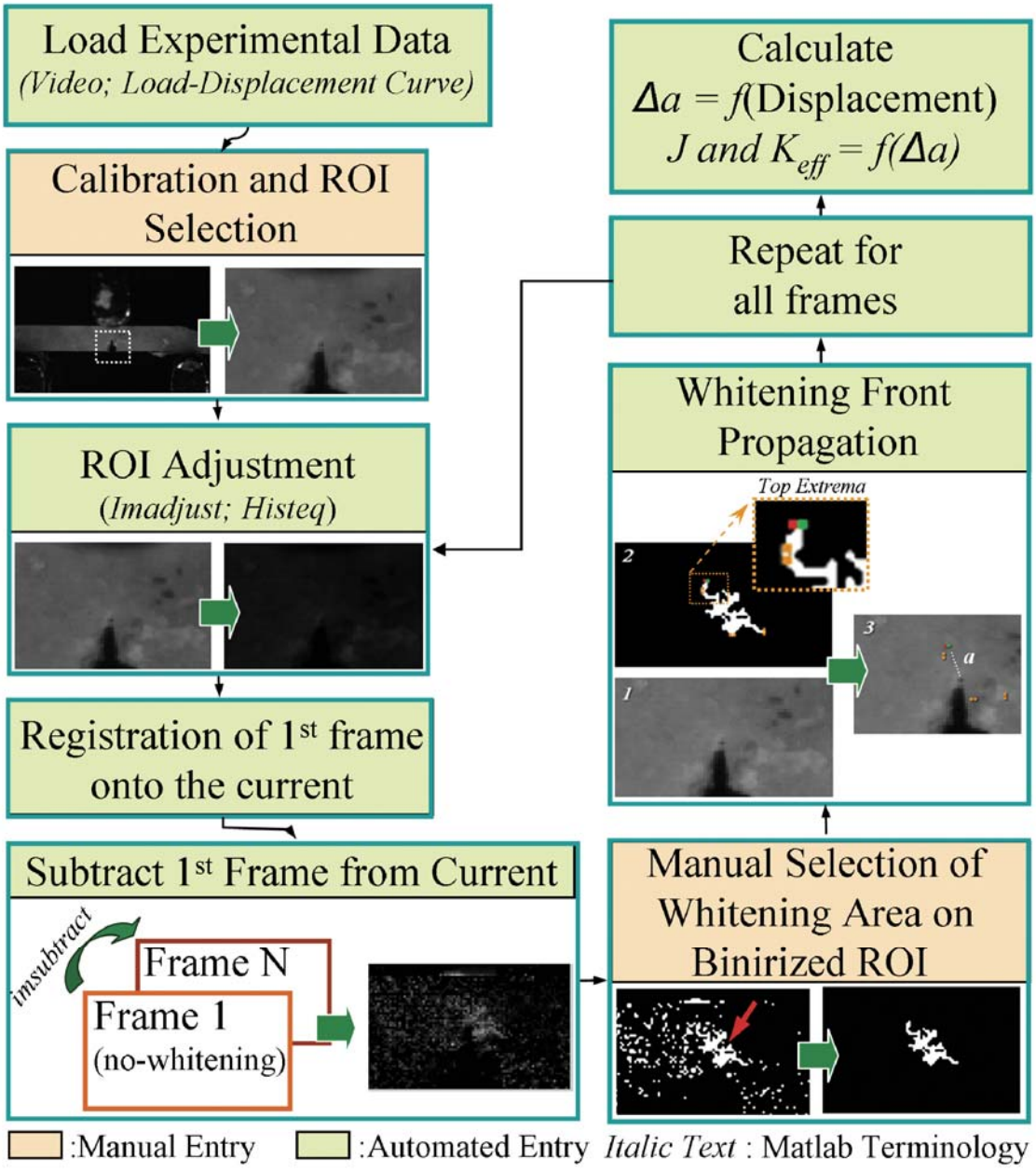

Figure 5-2: Outline of the "Whitening Front Tracking" algorithm.

5.2 Results

5.2.1 Whitening front- and crack propagation association

Figure 5-3 presents the detected whitening front and crack propagation for the rat tibia sample. As expected [*Leng et al. 2008; Sun et al. 2010*], the whitened area, corresponding to the damage zone, runs ahead of the crack tip during the whole experiment and is developing with the same rate as the growing crack (Figure 5-3 and video 6-1). The distance between the crack- and the whitening-front varied from 300 – 400 μm from sample to sample, but this distance was constant during the whole experiment. Pearson's coefficient used for testing the association between the whitening front propagation and the crack-propagation was $r = 0.97$; $p < 0.001$ indicating that the two phenomena are positively linearly correlated.

5.2.2 Determination of crack extension resistance curve

Crack extension resistance curves where recorded from tests on miniature human cortical bone samples using the SE(B) specimen setup. Analyzing the data collected from these samples, it was noticed that, in all cases, failure (i.e. the point of maximum load) was achieved when the whitening front reached the top surface of the sample, even when the visible crack was just at the beginning of the notch and far from the top surface (Video 6-2 and Video 6-3). Figure 5-4 shows the evolution of the damage zone during the three-point bending for a human cortical bone sample along with a schematic representation of the whitening area. Note that the "whitening" starts around the pre-notch and expands upwards, while no visible crack (in images recorded with the specified camera and lens setup) has been formed. Importantly, the moment that the whitening effect appears at the sample's surface, coincides with the moment that the load-displacement curve diverges from linearity and enters the plastic deformation area (Video 6-2, Video 6-3 and Figure 5-5). Finally, no instability fracture was observed on any of the samples even when the load bearing capacity of the specimen had completely vanished.

Determination of crack or more accurately "damage" extension resistance curves were achieved for the above specimens by using the whitening-front

propagation values generated by the algorithm developed as part of this study. The calculated resistance curves, expressed in terms of J and K_{eff} are presented in Figure 5-6.

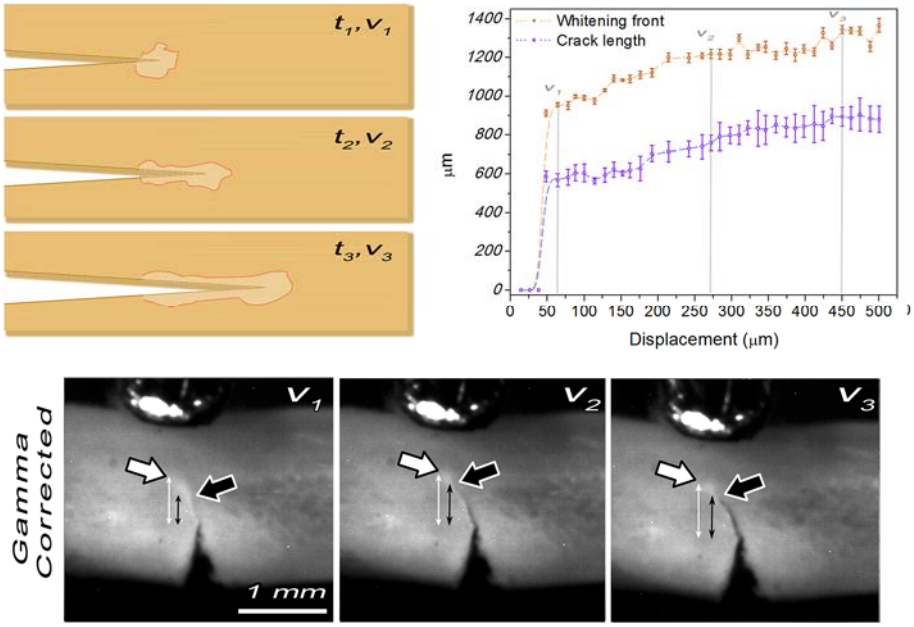

Figure 5-3: Crack- and Whitening Front- propagation relationship; (top left) Schematic representation of crack- and whitening front- propagation for three arbitrary time – displacement points ($t_{1,2,3}$,$v_{1,2,3}$). (*top right*) whitening front- and crack propagation relationship. Intraobserver variability is visualised on the plot by error bars indicating the standard deviation across the five repetitions. Note that both crack tip and whitening front are propagating in sync with the whitening front being constantly ~400 μm ahead of the crack tip. (bottom) Gamma corrected frames of a rat tibia sample showing the crack tip (black arrow) and the whitening front (white arrow) propagation during three point bending for the displacement points v_1, v_2 and v_3. Double arrowed lines represent the distance of the crack tip and the whitening front from the pre-notch.

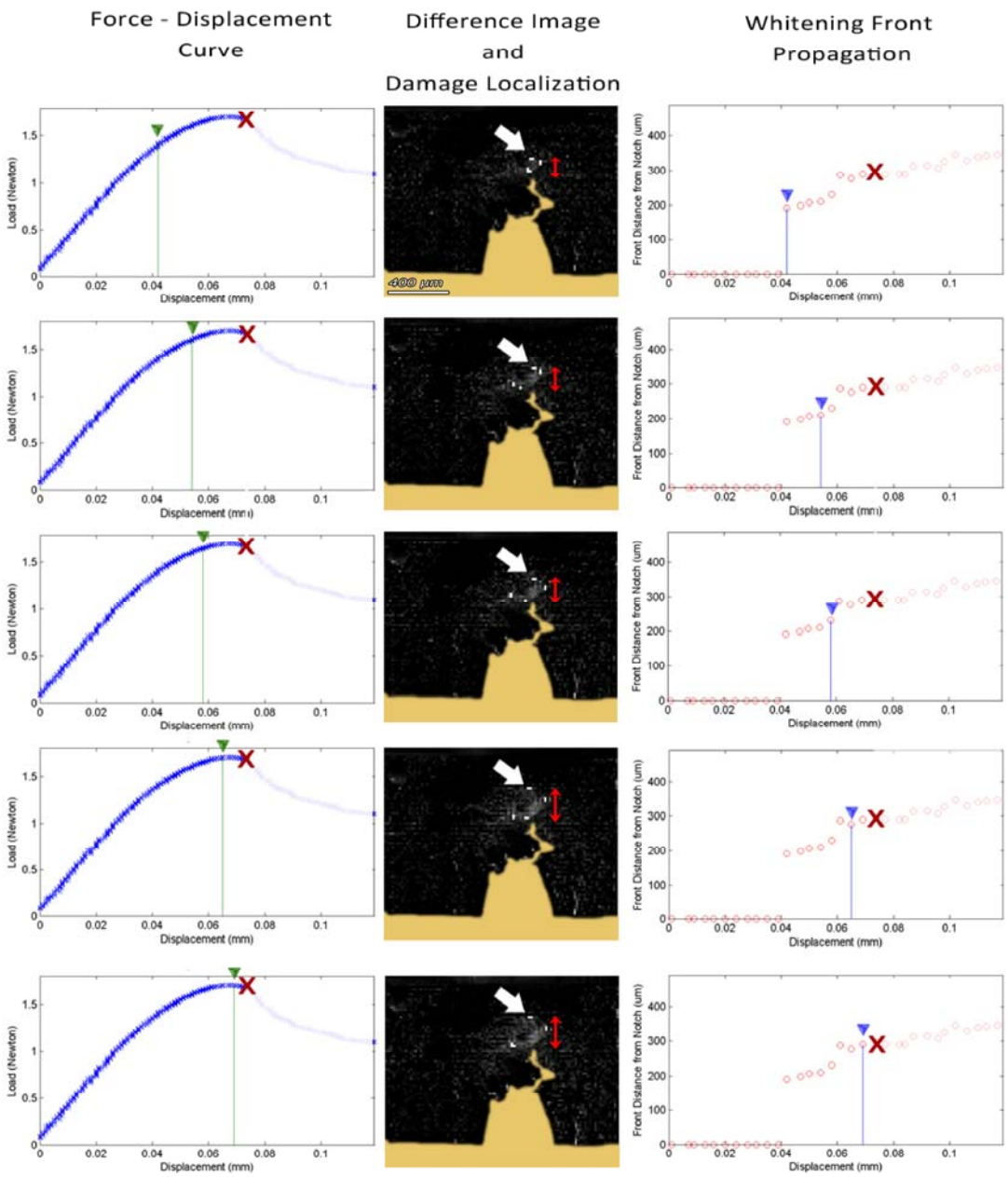

Figure 5-4: Time-lapsed snapshots of the fracture toughness experiment on an SE(B) sample also presented in video 6-2. (left) Force – Displacement curve; (middle) damage localisation on the calculated difference image; (right) Calculated whitening front propagation top-most white localiser pixel pointed by the white arrow on damage localisation picture red X represents point of failure.

5.3 Discussion

It is well accepted that bone, as a hierarchically structured material [*Rho et al. 1998b*], employs a range of toughening mechanisms at different length scales [*Launey et al. 2010*]. Hence, the nature of failure at different length scales should be also governed by the presence or the absence of some of the toughening mechanisms. In the macro-scale, cortical bone toughness is highly affected by crack deflections and twist on the different structural features of the bone tissue (namely bone lamellae, osteons, cement lines and osteocytes lacunae) [*Koester et al. 2008*] while at the smaller scales, bridging and micro-cracking are of higher importance [*Ritchie et al. 2009; Vashishth 2007*].

The latter are deemed for the whitening effect during bone failure which has previously been reported [*Leng et al. 2008; Thurner et al. 2007*], but to the best of my knowledge it has not been used for studying bone toughness behaviour.

The results of this study show a positive correlation between the whitening front- and the crack-tip propagation. In this study, the property of whitening was exploited for the determination of "crack" extension resistance curves in sub-millimetre samples. For this purpose miniature SE(B) cortical bone samples were prepared and their toughness behaviour was defined by tracking the whitening front propagation. Interestingly, in all SE(B) samples failure occurred due to the propagation of the damage zone. This can be explained as follows. As the specimens height (W) never exceeded 900μm and the pre-notch (a_0) was around 300 - 350 μm the available un-cracked ligament (W-a_0) left for testing was ~ 400 - 500 μm. From the experiments studying the correlation between the whitening effect and the crack propagation in rat samples, it was shown that the whitening front is always about 300 - 400 μm ahead of the crack-tip. In fact, the total length of the damage zone in human cortical bone can be as much as 5 mm [*Yang et al. 2006*]. Thus, the moment when the whitening front approaches the specimen's top surface the crack has just started forming on the edge of the notch. This was consistent on all specimens and brings back the question of crack-tip definition on bone samples. Today the common view is that the intrinsic toughening mechanisms, such as micro-

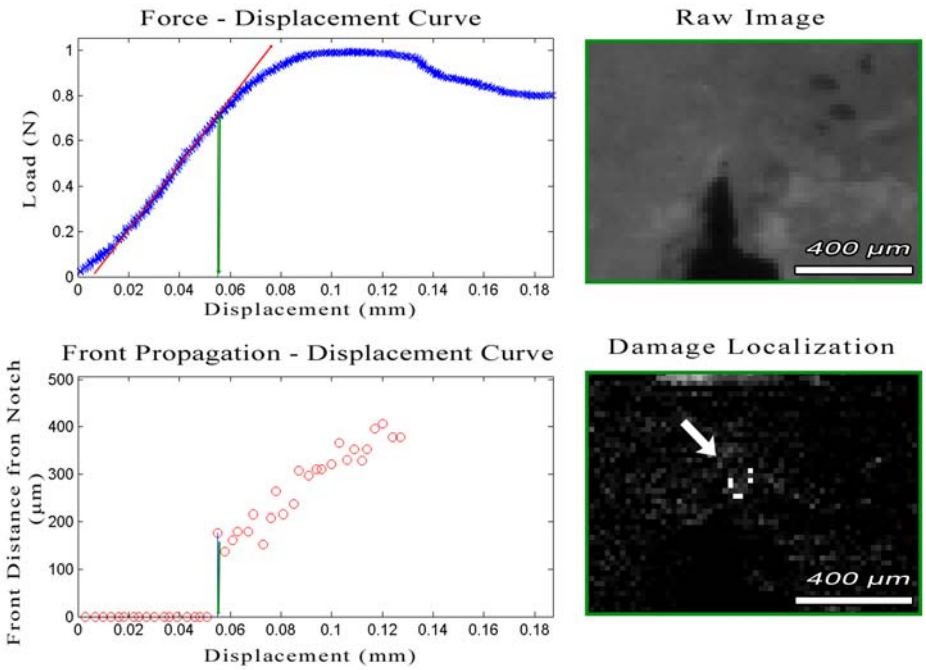

Figure 5-5: Initiation of the whitening effect at the initial notch; (top left) Load – displacement curve of a human sample under three point bending. The green line corresponds to the point when the whitening effect is first detected. Top right and bottom right images show the raw and the difference image of this point. Initiation of the whitening effect is localized at the difference image. Note that whitening effect appears on the surface of the sample when the Load-displacement curve diverges from linearity (red line) and enters the plastic deformation area

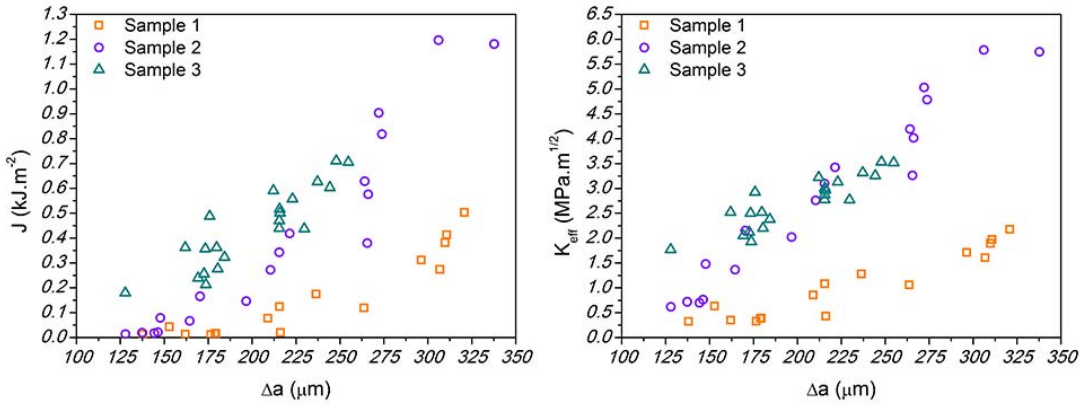

Figure 5-6: Representative "crack" resistance curves of three human bone samples expressed in terms of *J* and *K*

cracking, are acting "in front" of the crack-tip obstructing crack development by dissipating energy and reducing local strain concentration [*Ritchie et al. 2009; Ritchie et al. 2005*]. This observation confirms it in the basis that the damage propagation prevented the crack formation. However, for the given sample size, this propagation resulted in the failure of the sample. The latter is not surprising since diffuse damage growth has been shown to correlate with fatigue [*Leng et al. 2008*]. Consequently, in terms of failure resistance, when an apparent crack is not present (or visible) the whitening front propagation can be used as the "crack-tip".

By using the "Whitening Front Tracking" method fracture toughness curves similar to the ones reported in literature have been reproduced [*Koester et al. 2008; Ritchie et al. 2008; Vashishth 2004; Zimmermann et al. 2011; Zioupos and Currey 1998a*]. Koester *et al.* for example, using *in situ* environmental scanning electron microscopy managed to determine the fracture toughness resistance curves for the transverse and the longitudinal orientation of the human bone [*Koester et al. 2008*]. They reported significant difference between "breaking" (i.e. propagation of the crack perpendicularly to the osteons) and "splitting" (i.e. propagation of the crack parallel to the osteons) with "breaking" being tougher. K_{eff} curves for the two modes, for crack extension up to 950 μm, raised from 0 to 25 MPam$^{0.5}$ and 0 –2.5 MPam$^{0.5}$ respectively. The present study used samples oriented in the antiplane longitudinal orientation which is the third possible breaking orientation in respect to osteon's long axis (Figure 5-8). This cracking mode (we call it "separation") is similar to the "splitting" but because of the higher amount of deflections (cf. Figure 5-8) toughness is expected to be higher than "splitting" but much lower than "breaking". The K_{eff} curve determined by this new method for the same crack extension length exhibited rising behaviour with values ranging from 0 – 6 MPam$^{0.5}$ (Figure 5-6 and Figure 5-8) capturing this difference between "splitting" and "separating" mode.

Most importantly, this method overcomes the singe-value K_c approach [*Ritchie et al. 2008*] used for small samples and allows for the generation of "crack" extension resistance curves in a simple and fast manner. Finally, the "Whitening Front Tracking" method could also find applications on other materials exhibiting the stress-whitening effect during fracture like polymers, composites and resins.

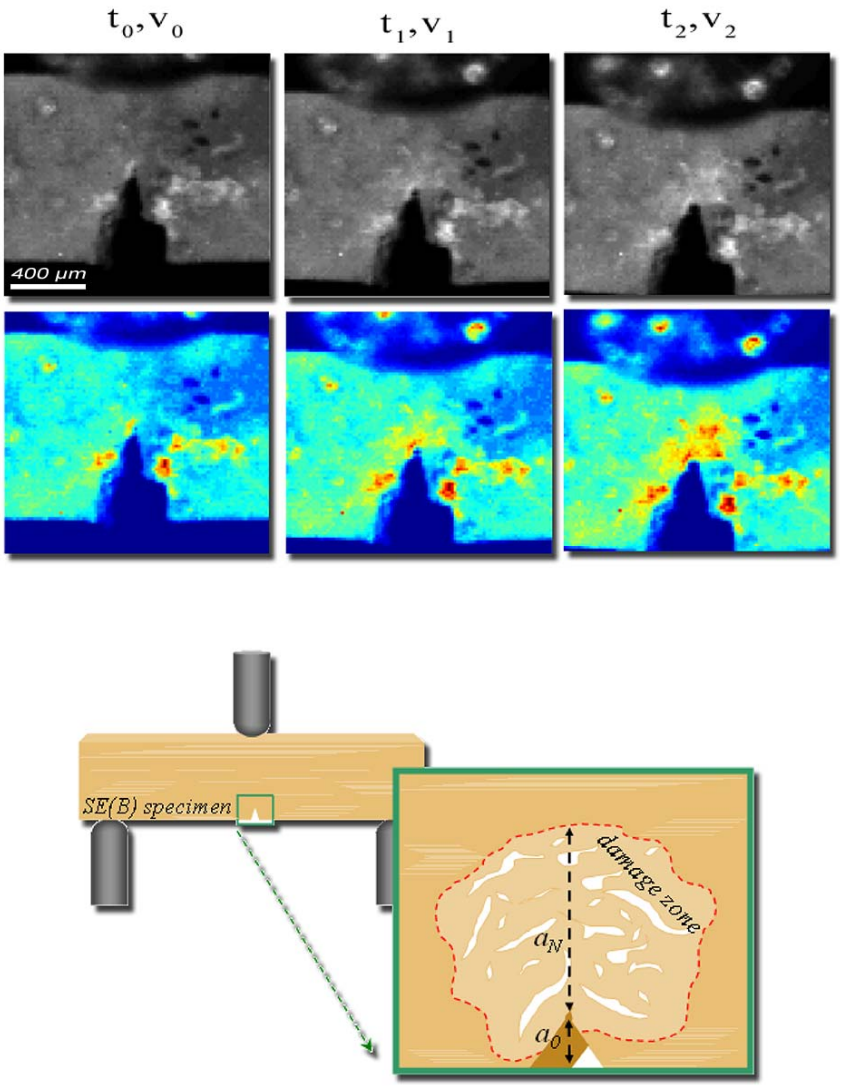

Figure 5-7: Evolution of damage zone (whitening) during the three-point bending test of an SE(B) specimen; (top) Gamma-corrected and false-coloured frames of a human cortical bone sample showing the sample at the beginning of the test (first frame), at the appearance (second frame) and the propagation (third frame) of the whitening front during three point bending at different time – displacement points. Sample width (W) is 930 µm and the pre-notch (a0) is 450 µm. t_0,v_0 correspond to the point where load and displacement equals 0, t_1… t_2…. (bottom); Schematic representation of the damage zone formed when bridging and microcracking initiate in front of the crack tip as a result of local stress and strain concentration. The "whitening effect" is deemed to be the result of increased light reflection on the surfaces of the newly formed micro-cracks within this damage zone.

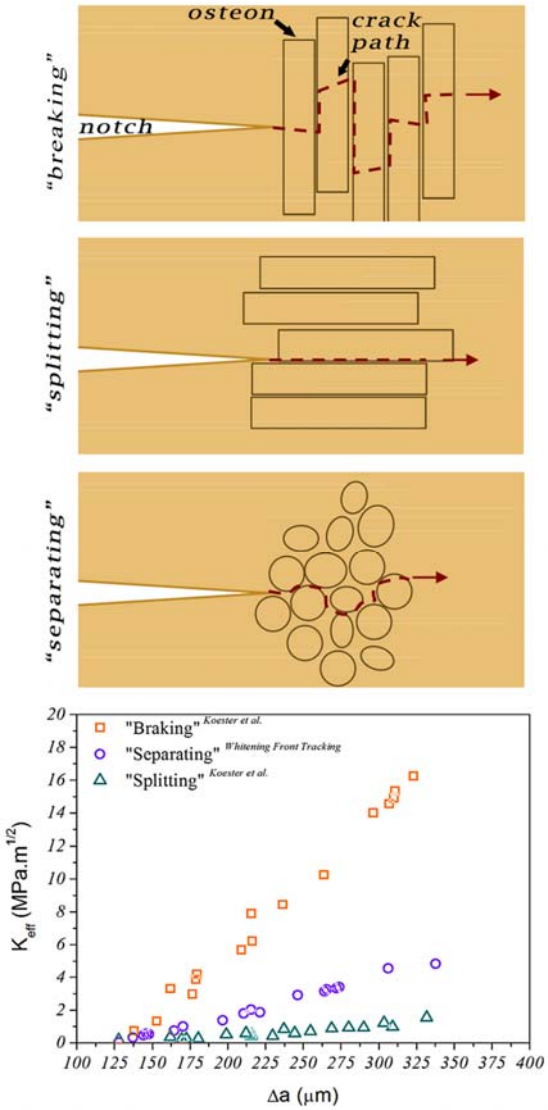

Figure 5-8: Schematic representation of the three possible cracking orientations of bone; In the "breaking" configuration, the notch is oriented perpendicularly to the long axis of the osteons, breaking through them during the propagation. This is the most energy consuming mode resulting in a steeply rising fracture resistance curves as shown by Koester et al. [Koester et al. 2008]. In the "splitting" configuration, the notch is oriented parallel to the long axis of the osteons, splitting them apart during propagation. In this mode the crack is mainly thought to follow the osteonal cement lines and a very small amount of deflection takes place. This results in significantly lower "crack" resistance behaviour in comparison to the "breaking" mode [*Koester et al. 2008*]. Finally in the "separating" configuration the notch is oriented perpendicularly to the osteons long axis, as in the "breaking" but this time, because of the anti-plane orientation, the crack is thought to be mainly propagating around the osteons following the cement lines instead of breaking thorough them. This results in resistance behaviour between the two "extreme" modes closer to the "splitting" one.

In summary, this study show that measurement of toughness of small cortical bone samples on which conventional fracture toughness analysis cannot be applied due to the difficulty of measuring the crack propagation, can be achieved by means of the “whitening-front tracking” method. This technique combines mechanical testing with videography and makes use of the stress-induced whitening effect for indirectly tracking the crack propagation. The technique provides sufficient resolution for the generation of crack-extension resistant curves from which both fractures toughness and crack-growth toughness can be assessed overcoming the single-value approach which was used to date in similar cases.

Chapter 6

Multiscale Experimental Analysis of Human Bone Fracture Toughness: from the Osteonal up to the Tissue Level

A journal publication based on the study presented in this chapter is currently in preparation. Preliminary results of this study have been/ are to be presented in:

- ✓ 18th Congress of the European Society of Biomechanics (ESB), Lisbon, Portugal, July 1-4, 2012
- ✓ Annual Meeting of the Orthopaedic Research Society (ORS), San Antonio TX, January 26 – 29, 2013

This study investigates the fracture resistance of human cortical bone at the tissue level and its relationship with the properties measured at lower hierarchical levels, namely the osteonal, and the micro level. The results show an association of bone fracture toughness and crack growth toughness at the tissue level measured by beans of fracture toughness experiments, with crack initiation resistance at the micro level assessed by reference point indentation (RPI) and energy storage and dissipation at the sub-osteonal level.

6.1 Materials and Methods

6.1.1 Cortical bone specimens preparation

Four human femora (females; aged 43, 47, 80 and 83) were obtained from the International Institute for the Advancement of Medicine (IIAM) and stored at -

80 ^{o}C. A butcher's bandsaw (BG 200, Medoc, Logrono, Spain) and a low speed precision saw (IsoMet, Buehler, Lake Bluff, IL, USA) was used for cutting the femora into single-edge notched three-point bend SE(B) specimens [*ASTM 2004*] (n = 20) of 0.8 - 0.9 mm width and height and 10 mm length oriented in the antiplane longitudinal orientation [*Launey et al. 2010*] (Figure 5-1). A low-speed saw and a razor blade along with a diamond suspension where used for notching the sample as described by Kruzic et al. [*Kruzic et al. 2005*]. During this process, care was taken to ensure that the notch-length was always kept shorter than the one third of the height of the specimen ($a_0 < 0.33 \cdot h$) in compliance with the ASTM E1820-01 standard [*ASTM 2004*].

6.1.2 Fracture toughness and crack growth toughness

Toughness experiments were conducted in three-point bending using the "Whitening Front Tracking" method described in chapter Chapter 5. In this study, 3-point bending tests were conducted using the Electro Force 3200 (Bose, Eden Prairie, MN, USA). A bending rig with a span of 6.15 mm was used and the force was applied at 0.01 mm/s. The development and the propagation of the whitening front was recorded using a high-speed camera (Ultima 512, Photron, San Diego, CA, USA) operated at 60 fps with two fibre optic lights illuminating the specimen from approximately + 45^{o} and – 45^{o} from the camera field axis. Finally, damage propagation resistance curves (R-curves) were generated by analysing the mechanical and the videography data using the "Whitening Front Tracking" algorithm (analytically described in chapter Chapter 5).

The strain energy release rate (*J-Integral*) was expressed in terms of *K-effective* (K_{eff}) using nonlinear-elastic fracture mechanics as described by Ritchie et al. [*Ritchie et al. 2008*] and ASTM standard E 1820 - 01 [*ASTM 2004*]. "Fracture resistance" was defined as the slope of the generated R-curve ($K_{eff} = f(\Delta a)$; with Δa being the propagation of the whitening front) while "fracture toughness" as the K_{eff} value at the point of maximum load. To ensure that all bone samples where fully hydrated they were submerged in Hank's balanced salt solution (HBSS) for four (4) hours before the experiments and only removed just prior to testing. Testing time, including positioning of the sample on the bending rig, alignment and loading, was in all cases kept under 1

minute to prevent the sample from drying. Upon measurement completion the fractured samples were put back into the HBSS solution.

6.1.3 Reference point indentation (RPI)

Reference point indentation measurements were conducted by means of BioDent^{TM} reference point indenter right after the fracture toughness experiments. The sample were loaded onto the force plate and the measurement head unit adjusted via the stand to apply a given reference force to the sample via the probe assembly. For these experiments, the reference force was set to 2N. Prior to testing on bone, the probe assembly was tested in air to ensure friction is less than 0.1 N then tested on PMMA to ensure the correct touch down distance (TDD) and peak force was achieved. The measurement cycle ramped up to a maximum force of 1.2 N, held at that maximum force for 2 sec then retracted, repeating the cycle 10 times at 2 Hz. As before, hydration was ensured by keeping the samples immersed in HBSS solution before the indentations and the measurement duration was kept under 1 minute.

6.1.4 Cantilever-based nanoindentation

6.1.4.1 Sample preparation

At the osteonal-level, cantilever-based nanoindentation was employed for measuring the modulation of the elastic properties between the lamellae and interlamellar areas (also referred to as thin lamellae). The experiments where conducted on the second half of the SE(B) samples as follows. Right after the videography fracture toughness experiments, the SE(B) specimen fragments were wrapped in HBSS soaked gauze and immediately stored in -80 ^{o}C until further preparation. At the day of the nanoindentation experiments the samples were left at room temperature until fully defrosted. When defrosted, one of the sample's faces (i.e. the surfaces which rest perpendicularly to the osteon's long axis) was polished using sandpapers and diamond suspensions until a final surface roughness of ~1 μm was achieved. The protocol involved initial polishing of the surface using a grit-1200 sandpaper (Buehler - Carbimet® Paper Disks) until a smooth surface could be observed followed by a three-step wet polishing procedure using polishing microcloths (Buehler) and a sequence

of 6 μm, 3 μm and 1 μm diamond suspension polishing solutions (Buehler MetaDi® Monocrystalline Diamond Suspension). After each polishing step the samples were immersed in an ultrasonic bath for two (2) minutes to remove any powder and diamond crystal residuals. Finally, the samples were glued on glass slides with their polished surface on the top using 2-component epoxy glue.

6.1.4.2 Instrument calibration

Cantilever-based nanoindentation was conducted in air by means of atomic force microscope (AFM) (Asylum Research, Santa Barbara, CA, USA) using conical shape silicon etched AFM probes (NCS15, Mikromasch, Tallinn, Estonia). The sensitivity of the cantilever was determined from the slope of the contact region of a force curve performed against an "infinitely" indeformable surface (glass slide) and the spring constant was then calculated from the thermal noise spectrum by means of equi-partition theorem [*Sader et al. 1999*]. Spring constant values were found to not vary significantly from those reported by the manufacturer being typically around 40 N/m.

The shape of each tip, required for the calculation of the projected contact surface area function, was assessed by means of numerical deconvolution in Matlab (version 7.10.0.4999, The MathWorks Inc, Natick, MA, USA) as described by Keller and Franke [*Keller and Franke 1993*]. The algorithm works by comparing an AFM height image of a subject with known geometry imaged using the "unknown" shaped tip (experimental image) against the numerically calculated image of the same object. Given that the experimental image is a convolution of the object and the tip shape, the tip can be reconstructed using the difference between the experimental and the calculated images using numerical deconvolution [*Keller and Franke 1993*]. Here, a spike with a cone angle of 50° (TGT-1 calibration grating, NT-MDT Tips, Wilsonville, OR, USA), was used as the calibration object. Finally, the projected area function was calculated from the reconstructed tip image using a built-in function of the AFM control and analysis software.

6.1.4.3 Nanoindentation measurements

Initially, imaging of the bone sample in AC-mode in air, allowed the localisation of the secondary osteons on which the nanoindentations took place. Approximately 400 ($300 \leq n \leq 625$) force-controlled (maximum load =80 nN;

indentation rate =45 nm/s) force-indentation curves where acquired from lamellae and the process was repeated for the interlamellar areas. Cement lines were considered separate osteonal features and they were not included in this analysis.

6.1.4.4 Data and statistical analysis

The nanoindentation curves recorded during the experiments were used for the determination of the reduced modulus, E_r. All curves were individually analysed using a custom made Matlab™ algorithm according to the Oliver-Pharr method [*Oliver and Pharr 2004*]. In more detail, using the approaching data each curve was offseted to the point of the first contact with the surface and the power low function of Eq. 7-1 was fitted to the unloading part of the curve (Figure 6-1).

$$P = a(h - h_f)^m \tag{6-1}$$

where *a* and *m* are the power law fitting constants.

The elastic unloading stiffness, $S = dP/dh$, was defined as the slope of the upper portion of the fitted curve and subsequently the E_r was estimated from:

$$E_r = \frac{S\sqrt{\pi}}{2\beta\sqrt{A}} \tag{6-2}$$

where *S* the unloading stiffness, *A* the projected contact area for the given contact depth (h_c) and $\beta = 1$ a correction factor (cf. §3.1.2).

The calculated moduli for of each osteonal feature of each sample were pooled together and statistical analysis was run on each one of these data sets in MATLAB®. Specifically, a Kolmogorov–Smirnov test was employed to test the normality of distributions and a Wilcoxon rank sum test with a significance threshold of $p = 0.01$ was used to test the significance of the difference of the measured E_r values between the two osteonal features, namely lamellae and interlamellar areas, of each sample. As before (cf. §4.1.8) Wilcoxon rank sum test was selected because the moduli values distribution measured on each

osteonal feature were not normally distributed and thus a non-parametric test was required. Finally, as there was no reason to assume only linear relationship between the different measures, Spearman's correlation analysis was selected to analyse the relationship among the various parameters measured in the different hierarchical levels.

Fracture toughness (tissue level)

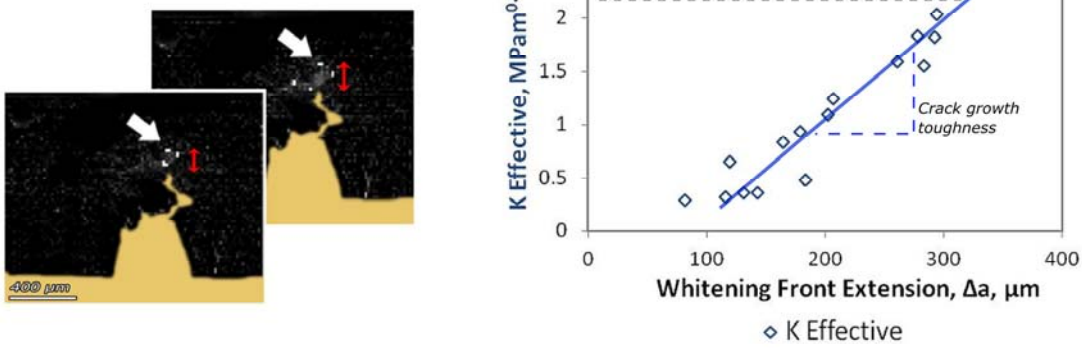

Reference point indentation (micro-level)

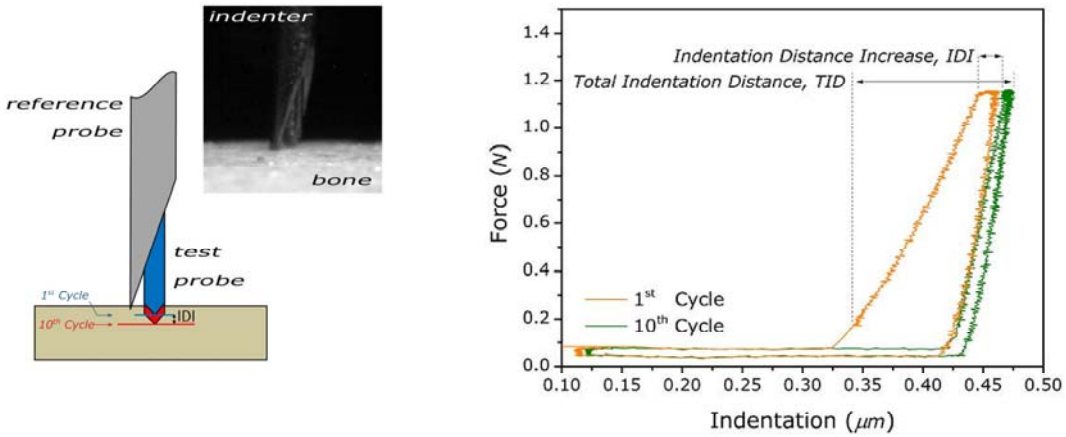

Nanoindentation (osteonal level)

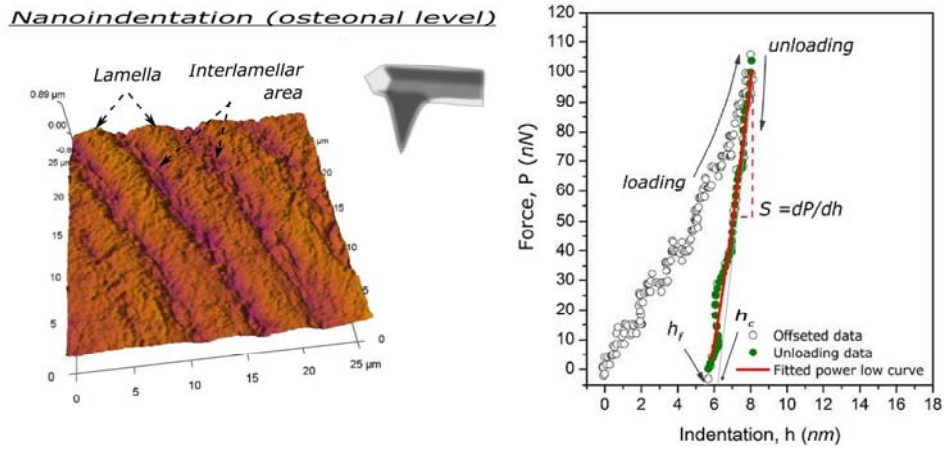

Figure 6-1: Experimental techniques used for the characterisation of the mechanical properties of the tissue in the tree different hierarchical levels and representative measurement for each one them. (Top) tissue-level; Fracture toughness and crack growth toughness measurements by means of "whitening front tracking" method describer in chapter Chapter 5. (middle) micro-level: damage resistance evaluation by means of RPI. (bottom) osteonal-level: characterisation of the elastic properties of lamellae and interlamellar areas by means of AFM cantilever-based nanoindentation.

6.2 Results

6.2.1 Expression of age-related degradation in tissue-, micro- and osteonal-level

Specimens from elderly donors (age: 80, 83; n =8) exhibited different behaviour in comparison to the younger ones (age: 43, 47; n =9) in all three different hierarchical levels examined in this study (Figure 6-2). In the tissue level, elderly group exhibited, on average, a 58.9% lower fracture toughness and a 60.3% lower crack growth toughness than young group. Similarly in the micro-level, RPI measurements showed that elderly group had, on average, a 15.1% higher "*indentation distance increase, IDI*" and a 13.0% higher "*total indentation distance, TID*" value. As a result, during indentation experiments 7.4% more energy was dissipated (*Mean ED*) in elderly specimens (Figure 6-2). Finally, on the osteonal level elderly group exhibited lack of elasticity inhomogeneity within osteons with lamella and interlamellar areas having similar reduced moduli (E_r) values while the younger group showed a mean difference of 21.4% between these two osteonal features with lamellae being less compliant that interlamellar areas.

6.2.2 Correlation analysis of the properties measured at the different hierarchical levels

The results of the correlation analysis among all features are presented in Table 6-1. As it can be seen the mechanical behaviour of the bone at the tissue level is correlated with its micro- and osteonal-level behaviour. The *crack growth toughness* at the tissue-level shows a negative correlation with both *IDI* and *TID*. Accordingly, *crack growth toughness* appears positively correlated with increased elasticity inhomogeneity between lamella and interlamellar areas

within single osteons at the osteonal level. That is, the higher the difference between the measured reduced moduli (E_r) between lamellae and interlamellar areas, i.e the more inhomogeneous in terms of elasticity the osteons are, the lower the *IDI* and *TID* appear to be and the higher the crack growth toughness. Interestingly, while fracture toughness (tissue level) is strongly correlated with the elasticity inhomogeneity at the osteonal level it is weakly, and not significantly, correlated with *IDI* and *TID* at the micro-level. Finally, a negative correlation appears between the elasticity inhomogeneity at the osteonal level and both the *TID* and the *Mean energy dissipation* during RPI.

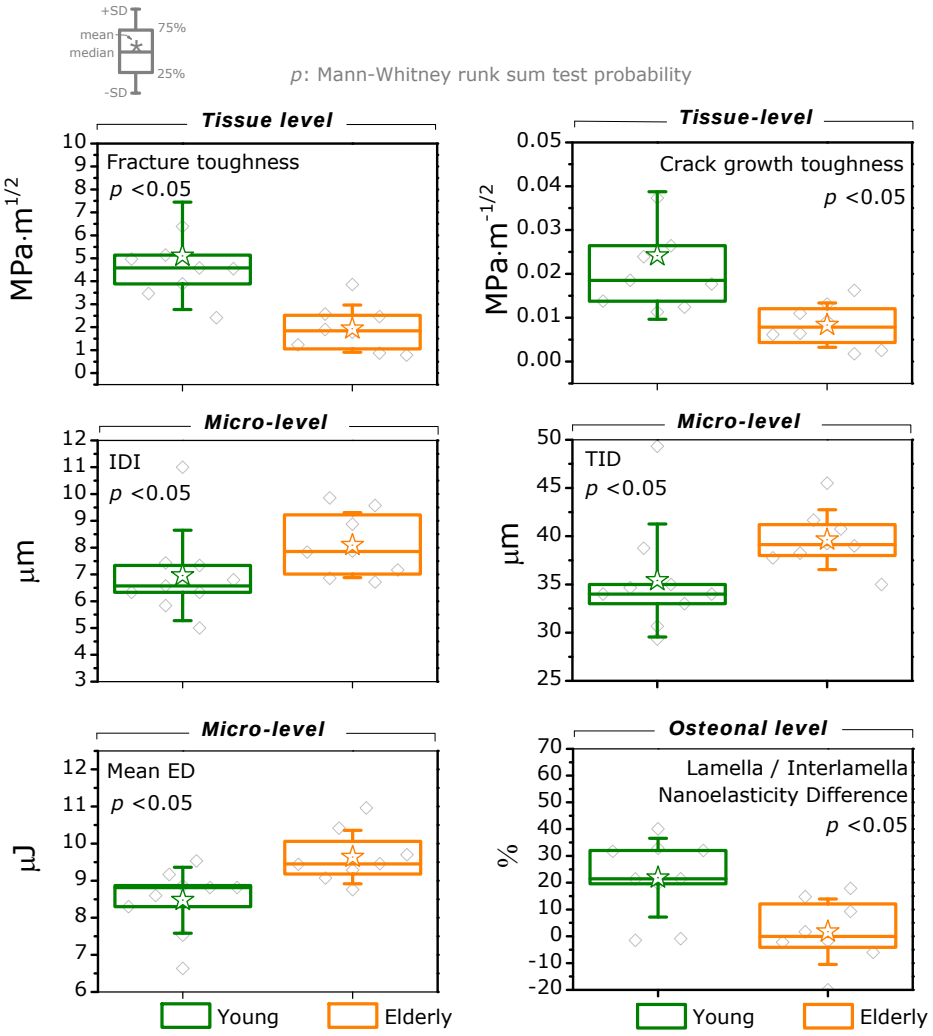

Figure 6-2: Measured properties of Young vs Elderly group at the different hierarchical levels.

Table 6-1: Spearman's rank correlation coefficient (ρ) for the different measures

	Tissue level		**Micro-level**			**Osteonal level**
	Crack growth toughness	Fracture toughness	IDI	TID	Energy Dissipated	$Er_{Lamella}$ – $Er_{Interlamella}$ Difference
Crack growth toughness	1	**0.84**	**-0.56**	**-0.58**	-0.46; p =0.06	**0.51**
Fracture toughness	0.84	1	-0.3; p =0.19	-0.45; p =0.06	-0.42; p =0.09	**0.80**
IDI	**-0.56**	-0.33	1	**0.85**	**0.67**	-0.32 p =0.21
TID	**-0.58**	-0.45	0.84733	1	**0.73**	**-0.50**
Energy Dissipation	-0.46	-0.42	**0.67**	**0.73**	1	**-0.55**
$Er_{Lamella}$ – $Er_{Interlamella}$ Difference	**0.51**	**0.80**	-0.32	**-0.50**	**-0.55**	1

p >0.05 unless otherwise stated

6.3 Discussion

Bone is a complex, hierarchically structured, nanocomposite material comprised of more than four different hierarchical levels spanning from the nanoscale to the tissue level. As such, the ultimate mechanical behaviour of the tissue should depend on the mechanical behaviour of each one of these levels as well as on their collective behaviour. This study investigated the correlation of the fracture toughness and the crack growth toughness measured at the tissue-level to properties like *IDI*, *TID* and elastic inhomogeneity measured at the micro- and the osteonal-levels. It was demonstrated that in all three levels examined there is an age-related degradation of the quality of the bone matrix suggesting a direct relationship of these measures to the ultimate mechanical behaviour of the tissue. This relationship was further investigated by correlation analysis revealing a direct correlation of the crack growth toughness and the fracture toughness (tissue level properties) with the mechanical properties of the tissue in the micro- and the osteonal-level. In more detail, higher fracture toughness and crack growth toughness was correlated with higher modulation in elasticity within osteons, and lower *IDI*, *TID*, and *Mean ED* at the micro-level.

The negative correlation between toughness and the tree RPI measures (Table 7-1; *IDI*, *TID* and *Mean ED*) is consistent with the resent studies by Diez-Perez et al. [*Diez-Perez et al. 2010*] and is attributed to the susceptibility of the bone matrix to microcracking. As RPI induces microcracks, *IDI* and *TID* directly assess the ability of the bone to resist crack initiation and propagation. Older bone is know to be more susceptible to develop microcracks [*Courtney et al. 1996*] a reasonable consequence of which is that the elderly group exhibits higher *IDI* and *TID*. The fact that in the elderly group there is a higher degree of microcracking also means that a higher amount of energy is consumed during RPI which in turn explains the higher *Mean ED* value measured for this group as compared to the young one (Figure 6-2).

Most interesting is the correlation between toughness and nanoelasticity inhomogeneity of the osteons. To the best of my knowledge this is the first time such a correlation is being reported. According to the data presented here, high fracture toughness and crack growth toughness correlate with high degree of nanoelasticity inhomogeneity between osteonal lamellae and interlamellar areas ($\rho = 0.51$ and $\rho = 0.80$ respectively). That is, the higher the difference of the reduced modulus (E_r) between lamellae and interlamellar areas the higher the fracture- and the crack growth toughness. As shown and discussed in chapter Chapter 4, the elasticity inhomogeneity between lamellae and interlamellar areas is related to compositional and structural differences between these two features and serves as an energy storage mechanism which allows osteons for non-destructive micro-movements. Digital image correlation (*DIC*) experiments showed that, during loading, the NCP-rich (and collagen deficient) interlamellar areas take-over a higher amount of strains compared to lamellae which results in strain redistribution within the osteon preventing damage formation. It is thus not surprising that in this study, the higher the degree of nanoelasticity inhomogeneity of the osteons appears to be, the lower the *Mean ED* measured by RPI is ($\rho = -0.55$). It seems that this mechanism of reversible energy storage acts during RPI preventing the formation of microcracks and upon unloading returns the energy stored as elastic deformation on the interlamellar areas back to the system. On the tissue level, this difficulty of microcrack formation is reflected as elevated toughness.

Age-related degradation of bone mechanical properties -including toughness- is a well known phenomenon [*Wang and Puram 2004*] which has been related to

changes in bone mass [*Boyce and Bloebaum 1993; Currey et al. 1996*], porosity [*McCalden et al. 1993*], microdamage accumulation [*Schaffler et al. 1995*], collagen degradation [*Wang and Puram 2004*], etc. All these studies have contributed to the current understanding of bone mechanics providing valuable information regarding bone's fracture behaviour. Nevertheless, it is still poorly understood how these changes affect the behaviour of the bone at the different hierarchical levels and how they associate with each other. How do the intrinsic toughening mechanisms propagate from the lower to the higher hierarchical levels and which features are responsible for this propagation?

From the fracture mechanics view point, it is well accepted that during failure osteons play a major role on the fracture behaviour of the bone and their importance has been mainly attributed to their crack deflection/trapping ability [*Koester et al. 2008*]. The data presented here suggest that osteons could play an equally important role on preventing microcrack formation by acting as "dampers" embedded in the bone matrix which, during loading, store energy on the stressed interlamellar areas. For this mechanism to work without diminishing the osteon's ability to carry loads the nanoelasticity inhomogeneity between the two osteonal features, i.e. lamellae and interlamellar areas, is necessary. This way, the less-compliant lamellae carry the higher amount of the applied load while the interlamellar areas take-over the exceeded strains. It is worth noting that this is not a new concept of load bearing in bone, as similar mechanisms have been proposed to be acting on the nanoscale [*Deymier-Black et al. 2011; Gupta et al. 2007*].

Vice versa, equalisation of the elastic properties of osteonal features diminishes the ability of the osteon to store elastic energy during loading (e.g. during RPI) resulting in earlier damage formation. Thus, specimens with more homogenous osteons with regards to nanoelasticity appear to be weaker than the inhomogeneous ones. This also seems to be the case for the elderly group where decreased toughness associates with decreased osteonal nanoelasticity inhomogeneity (Figure 6-2). At the moment, the reason behind this equalisation is not known but it would be reasonable to speculate that change in the quality of the collagen which is responsible for the ductility of the matrix [*Garnero et al. 2006*] and/or alternation of the NCP concentration in the interlamellar areas play a role in this process.

It is nowadays becoming more and more clear that the bone fragility of the individual does not solely depend on the loss of the bone mineral density (BMD) [*Marshall et al. 1996*] but is also associated to changes in content and biochemistry of bone matrix [*Paschalis et al. 2004*]. For example, patients with normal BMD experiencing spontaneous fractures showed altered ratio of mature (non-reducible) to immature (reducible) collagen cross-links compared to non-fractured young, age-matched controls [*Paschalis et al. 2004*]. Alteration of the intermolecular cross-linking of the collagen fibres is known to affect its shear modulus [*Yang et al. 2008*] which in turn would affect the viscoelastic behaviour and load bearing capacity of the tissue. Furthermore, a recent study by Thurner and co-workers [*Thurner et al. 2010b*] showed that changes in the bone matrix in the content of the non-fibrillar proteins like Ostopontin can also lead to increased bone fragility independently of BMD.

In chapter Chapter 4 it has been shown that the two osteonal features, i.e. the lamellae and the interlamellar areas, differ in terms of structure and composition of the organic matrix but appear similar in inorganic/mineral content. In fact, interlamellar areas were found to be NCP-rich and collagen deficient compared to lamellae, while the collagen fibrils were developed circumferentially around the Haversian canal in contrast to lamellae where the fibrils were rather "standing" in parallel to the canal. Changes in the organic matrix, like the ones mentioned, induced by age and/or pathology could affect the ability of the interlamellar areas to deform in a non-catastrophic fashion making the osteon more susceptive to microcrack formation. Hence, reducing bone fracture toughness.

In summary, this study has demonstrated that the decrease of the elasticity inhomogeneity between osteonal lamellae and interlamellar areas can be directly correlated with diminished fracture- and crack growth toughness, and diminished resistance to crack-initiation. This experimental investigation complements existing computational studies on multiscale modelling of the mechanical properties of bone and adds to the effort the bone research community is putting into the quest for uncovering the structure-function relationship of bone.

Chapter 7

Discussion and Conclusion

The present chapter summarises the outcomes of this study, the limitations and the issues which remain to be answered in the future.

7.1 Summary of the thesis outcomes

The aim of this study was to improve the understanding of the contribution of cortical bone's micro- and nano-structural features to its ultimate mechanical properties; and especially its fracture resistance and toughness behaviour.

Starting from the osteonal-level, the load transfer was studied in relation to the measured structural and compositional differences of the sub-osteonal features of cortical bone, namely lamellae and interlamellar areas, using bovine bone. This series of experiments revealed evidence of a previously unknown load-transfer mechanism which transfers load and movement between lamellae and interlamellar areas in a manner analogous to the engineered "elastomeric bearing pads" used in large engineering structures.

With the next step being the study of the correlation of the fracture toughness with the micro- and nano-mechanical properties of cortical bone, a method able to generate full fracture-resistance curves in small bone samples where crack propagation cannot typically be observed had to be developed. The resulting "whitening front tracking" method achieves this by tracking the damage zone front propagation formed around the crack tip.

Finally, the correlation of the fracture toughness and the crack growth toughness with the mechanical behaviour of the tissue at the micro- and the osteonal-level was studied on human cadaveric samples. The results showed that the ultimate toughness properties of the tissue correlate positively with the

elastic inhomogeneity between the sub-osteonal features and negatively with the indentation distance increase, *IDI*, the total indentation distance, *TID*, and the mean energy dissipation, *Mean ED,* parameters measured at the micro-level. Moreover, the age-related degradation of the properties measured at all three levels; that is tissue- micro- and osteonal level, further suggest a direct relationship of these measures to the ultimate mechanical behaviour of the tissue.

The present study offers a novel insight upon bone's mechanical behaviour associating its ultimate toughness with a previously unknown mechanism acting at the osteonal-level. The results presented herein provide strong evidence that osteons are much more than structural components. Osteons are also important functional elements which contribute to the fracture toughness and the crack growth toughness of the tissue. Besides being just obstacles to the crack propagation, osteons significantly contribute to the intrinsic toughness of bone tissue through an energy storage and dissipation mechanism deriving from the elastic inhomogeneity between subsequent lamellae and the interlamellar areas. This nanoelasticity inhomogeneity allows osteons to adapt to high stresses via stretching the more compliance interlamellar areas increasing this way the amount of energy that can be stored on the structure without damage formation. As shown in human bone samples, absence or decrement of the nanoelasticity inhomogeneity of lamellae and interlamellar areas was correlated with lower fracture toughness and crack growth toughness. Similarly, absence or decrement of the nanoelasticity inhomogeneity of osteons was also correlated with reduced damage resistance as measured by RPI in the micro-scale. Table 7-1 summarises the outcomes of this study with respect to each series of experiments.

Further to this we can speculate that these compliant interfaces in bone microstructure could also serve as mechanotransducers. Osteocytes are generally believed to require much larger strains than the ones experienced in bulk bone; hence such "soft" interfaces could be of high mechanobiological importance.

Table 7-1: Outcomes

Elasto-plastic regions in the micro-structure of cortical bone for energy storage and dissipation

A compositional, structural and mechanical characterisation study of osteonal lamellae and interlamellar areas was accomplished:

- μ-RAMAN microscopy showed that interlamellar areas are collagen-deficient and NCP-rich.

- In-situ AFM imaging during micromechanical testing showed that the NCP-rich interlamellar areas are relevant for fracture toughness by being favourable crack propagation paths.

- For the first time such propagation within the interlamellar areas was captured in a time-lapsed fashion by means of AFM.

- AFM studies of partially demineralised osteons showed that interlamellar areas are structurally distinct features compared to lamellae comprised of circumferentially arranged collagen fibres.

- AFM cantilever-based nanoindentation studies showed selective deformation and stiffening of interlamellar areas under load.

- DIC studies of osteons in the loaded and unloaded state revealed higher strain concentration in the interlamellar areas under isostress loading conditions.

- A previously unknown toughening mechanism was proposed to be acting in the osteonal-level of cortical bone which transfers load and movement in a manner analogous to the engineered "elastomeric bearing pads".

"Whitening front tracking" method: A novel videography method for generating crack extension resistance curves in small bone samples

A novel computer-aided videographic analysis method for generating crack extension resistance curves in small bone samples was developed and tested:

- The new technique provides fast and accurate generation of full crack extension resistance curves of small bone samples by means of videography.

- The "whitening effect" which appears in front of the crack-tip can be used to consistently and accurately generate "crack" extension resistance curves in small bone samples.

- This method overcomes the small size limitations and the single value approach as well as the need for expensive equipment such as ESEM.

- The "whitening-tracking method" can also be used in other research fields as many materials show stress-whitening effect during fracture. Polymers, composites and resins are characteristic examples of such materials.

Multiscale experimental analysis of human bone fracture toughness

A correlation analysis study between tissue-, micro- and osteonal-level measures of human cortical bone was successfully carried out:

- Comparison between tissue- and osteonal-level properties showed that the tissue-level properties namely fracture toughness and the crack growth toughness, positively correlate with the measured elastic inhomogeneity between lamellae and interlamellar areas. That is, higher fracture toughness and crack growth toughness correlated with higher elasticity inhomogeneity between lamellae and interlamellar areas.

- Comparison between tissue- and micro-level properties were in-line with previously published studies showing that higher fracture toughness and crack growth toughness correlate with lower *IDI*, *TID*, and *Mean ED*.

- The osteons' contribution to the fracture toughness and the crack growth toughness of cortical bone goes above their ability to deflect/trap cracks. They could also play an equally important role on preventing microcrack formation by acting as "dumpers" embedded in the bone matrix which, during loading, store energy on the stressed interlamellar areas

7.2 Experimental Limitations and Optimisation

As with every study a number of limitations exist and this is also the case for this thesis. Highlighting the most profound ones for every study one should stand on (a) the condition of bovine bone samples used for the in-situ AFM analysis during the micro-tensile test and especially for the nanoelasticity characterisation; (b) the effect of the user-tuned parameters on the accuracy and reproducibility of the results of the "whitening-front tracking" method and (c) the number of donors which were analysed in the multiscale experimental analysis of the human bone samples. In more detail:

The mechanical characterisation measurements of the bovine cortical bone specimens, i.e. the in-situ AFM imaging during micro-tensile experiments, the DIC and the AFM cantilever-based nanoindentation, were conducted on dry or partially-hydrated samples. This was due to the incompatibility of the NanoRack® with the currently available fluid-cell setups. Nonetheless, dehydration is known to affect the elastic properties of bone and thus repetition of these experiments on fully hydrated samples would be desirable. It is likely that fully hydrated osteons would demonstrate stronger elasto-plastic behaviour during loading and higher strains could be developed on the interlamellar areas.

With regards to the "whitening-front tracking" method it is important to note that just like with any other semi-automated algorithm the results are subject to manual tuning of the various parameters. In the current version, parameters such as the gamma correction, the thresholding and the morphological opening have been chosen on a *trial and error* basis. Furthermore the manual selection of the whitening region is also subject to interobserver variability the effect of which has not been quantified.

Finally, the multiscale experimental analysis of human bone fracture toughness was based on samples derived from four (4) donors and as such it should not be considered as an epidemiological study. Even though results regarding the differences found between "young" and "aged" sample groups are presented it should be stressed that these "groups" consist of samples derived from two patients / "group". Repetition of these experiments on samples retrieved from a

larger population is needed in order to draw safer conclusions regarding the effect of aging on the properties measured in these experiments.

Apart from these, Table 7-2 presents a number of other less profound but important limitations which should be stressed out with respect to each series of experiments.

Table 7-2: Limitations and optimisation options

Elasto-plastic regions in the micro-structure of cortical bone for energy storage and dissipation
• The compositional results of this study are predominantly qualitative. Further work should be carried out in order to quantify the compositional difference between lamellae and interlamellar areas by using, for example, complementally analytical techniques such as Fourier transform infrared spectroscopy (FT-IR) or perhaps X-ray photoelectron spectroscopy (XPS / XPS-imaging).
• The experiments were conducted on bovine bone samples derived from the mid-shaft of the femur of a single animal. No information regarding any cross-anatomical location, cross-individual or cross-species variation is available. Furthermore, age- and/or pathology dependent variation of these properties is also unknown.
• In this study, cement lines were considered distinct structural features and were not included in the analysis. Yet, these features are known to affect crack propagation contributing to the fracture toughness behaviour of the tissue. Characterisation of these features similar to this conducted form lamellae and interlamellar areas is needed for the competition of the proposed model.
"Whitening front tracking" method: A novel videography method for generating crack extension resistance curves in small bone samples
• *Gamma correction* is done manually in a "trial and error" basis. This procedure is time consuming and could potentially affect the outcome of the results if the correct value of gamma is not selected.

- The *histogram equalisation* which is applied on every single frame is sensitive to high intensity pixels such as those that appear as a result of reflection of light on to the metallic component of the loading rig. When this happens, the less-intense "whitening effect" on the surface of the sample is masked by the high intensity reflection. Thus, manual segmentation of the ROI in such a way that no reflection appears in it during the whole experiment is necessary.

- The algorithm is based on the subtraction of the 1st frame where no whitening has been developed yet, from the N^{th} frame where the whitening has appeared. For this the registration of the 1st frame onto the N^{th} is necessary as the latter has been translated with respect to its initial position as the result of the loading. To make sure than the whitening area is not distorted during the registration, the algorithm assumes that this is a pure translation and "*rigidly*" registers the 1st frame onto the N^{th}. This can be considered a valid approach only for small displacements. For larger ones a semi-rigid approach should be used instead.

- The threshold, as well as, the structural element pixels size used for *thresholding* and *morphological opening* of the frame resulted from the subtraction mention above are also selected manually in a "trial and error" basis.

- Because the "whitening effect" is a low intensity phenomenon *thresholding* and *binarisation* of the frame results in small, few pixels wide areas not related to whitening effect to appear along the surface of the sample (cf. Figure 5-2: Manual selection of whitening area on binarised ROI). These areas are excluded by manually selection of the whitening area. While this is a straight forward task when the whitening has been developed, in the initial stages where the whitening area is also a few pixels wide is difficult to be distinguished. This forces the user to wait until the whitening area gets wider loosing the initial stages of whitening development. A backwards tracking of the whitening effect could potentially resolve this issue and even make possible the automatisation of this procedure.

- Automatisation of tracking procedure will also allow faster and higher resolution tracking which is time consuming at the moment. In such a case a high-speed camera could be used to analyse, not only the stable but also the unstable crack propagation.

- No information regarding the inter-user variability which could potentially derive from the manual setting of the analysis parameters has been analysed.

Multiscale experimental analysis of human bone fracture toughness

- In contrast to the fracture toughness and RPI measurements AFM cantilever-based nanoindentation measurements were conducted on dry samples. This affects the elastic behaviour of the tissue and for this reason only the relative difference between lamellae and interlamellar areas were measured.

- No compositional information was obtained from these specimens.

7.3 Open questions and future work

In this section some of the questions which have arisen as a result of this thesis and remain to be answered in the future will be discussed. From this perspective potential future research steps will be proposed.

As discussed in the previous chapters, this work revealed an unknown mechanical function of the osteon which originates from the elasticity inhomogeneity of its lamellar components; that is, osteon lamellae and interlamellar areas. It further showed that lack of such inhomogeneity correlates with lower fracture toughness and crack growth toughness as well as with lower resistance to damage. Yet, the following questions remain:

- Which are the properties of cement lines within this context?

- It is still unknown which is the origin of this inhomogeneity. It is not clear for example if this is a result of the different arrangement of the collagen fibrils, the difference in composition between the lamellae and the interlamellar areas or a combination of both.

- How does this mechanism affect the ductility and the viscoelastic behaviour of the bone matrix?

- What is the role of the NCPs in this mechanism and how it is affected by their presence or absence?

With regards to the multiscale experimental analysis presented in chapter 0 the following questions arise:

- What is the composition of lamellae and interlamellar areas of the samples exhibiting low inhomogeneity and how does this differ from the higher inhomogeneity ones?
- What is the composition of lamellae and interlamellar areas of "young" samples and how it differs from the "elderly" ones?
- Is the elastic inhomogeneity affected by pathology? If yes, in which way?
- If the inhomogeneity associates with the toughness and the resistance to damage can we intervene at the level of inhomogeneity in order to reduce fracture risk?

From my perspective the most important next step should involve a study similar to the one presented in chapter Chapter 4, which along with the lamellae and the interlamellar areas will also include the cement lines. As mentioned earlier in §0, from the materials science and the fracture mechanics point of view cement lines are very important features and it is well known they affect bone fracture behaviour. Nevertheless, and despite the fact that cement lines have been intensively studied, their composition seems to be a matter of an ongoing debate. In addition, cement lines are interfacial features of level 5 that separate the osteon from the interstitial bone and in this context their function could be similar to the function of the interlamellar areas at level 4. Uncovering the composition and the mechanical behaviour of the cement lines would then allow for the implementation of these properties into novel, more advanced, models of the osteonal cortical bone.

Additional future work aiming to address some of the remaining open questions mentioned at the beginning of this section could then include a compositional analysis study of samples with different osteonal-nanoelasticity inhomogeneity. This study could focus on variations of the NCP content among osteons with different nanoelasticity inhomogeneity aiming to uncover the relationship between NCP-content and nanoelasticity inhomogeneity. Such a study could be further supported by in-situ spectroscopic analysis, e.g. Raman or FTIR microscopy, during micro-tensile experiments which will reveal how the various

components of the bone, i.e. collagen / NCPs / minerals, respond when subjected to various loading conditions.

7.4 Epilogue

Since Hippocrates (460 – 377 BC) took the very first steps on a long journey for exploring human anatomy up to our days, bone has always been in the epicentre of scientific research. It has been studied out of scientific curiosity, as a blueprint for novel biomimetic materials but most importantly in an effort to understand its structure, behaviour and pathology so that we can intervene when needed to relief pain and improve the life quality of the humanity. As science and technology advanced we were able to see deeper and deeper into bone's complex hierarchical structure and further our understanding on one of the nature's most complex designs.

This thesis took its place alongside numerous other studies in this ongoing quest and shed light onto osteons' contribution to the intrinsic toughening mechanisms of bone. This previously unknown function supplies bone with an additional optimal load transfer and energy dissipation mechanism in which the NCP-rich interfaces (interlamellar areas) play a vital role. Compositional and/or structural changes lead to an optimized system with a capacity of reversible elasto-plastic deformation prior to true damage formation. The stretching and relaxation of NCP-rich areas, when the tissue is under load, could serve as an important energy dissipation mechanism to delay crack initiation and increase fatigue life. These results highlight the importance of NCPs on the mechanical properties and fracture behaviour of bone and suggest that NCP deficiency in the bone tissue due to age or disease should be considered as an important indicator of diminished bone toughness.

Uncovering the structure-function relationship on every hierarchical level of a material as complex as bone is undoubtedly an extremely challenging task. Nonetheless, deep knowledge and understanding of these relationships and the structural and compositional parameters which steer them would lay the foundations for the development of better diagnostic tools and treatments.

Appendices

Appendix 1 – Supplementary materials

Electronic material is accompanying this thesis. Specifically:

- Video 5-1: Time lapsed AFM imaging of stable cracks propagation in bovine cortical bone
- Video 6-1: Composition showing the Whitening front propagation method in action. (top-left) force – displacement curve recorded during the three point bending experiment; (centre) Raw videography image of the ROI as recorded during the three point bending experiment; (top right) Enhanced difference image. Note the artefact strip which appears at the top of the frame as the result of the registration of the 1^{st} frame onto the moving N^{th} frame; (bottom right) the resulted localization of the "whitening area" after the manual; (bottom left) appearance and propagation of the whitening front. Example 1
- Video 6-2: Same as Video 6-1. Example 2
- Video 6-3: Three point bending of whole rat bone sample. Note the self-similar propagation of the whitening and the crack.

Appendix 2 – Publications

Refereed Articles

1. **Katsamenis, O. L.**, Chong, H.M.H., Andriotis, O.G., Thurner, P.J., 2012. "*Load-Bearing in Cortical Bone Microstructure: Selective Stiffening and Heterogeneous Strain Distribution at the Lamellar Level*". Journal of the Mechanical Behavior of Biomedical Materials.

2. Szabó, M., Zekonyte, J., **Katsamenis, O. L.**, Taylor, M., Thurner, P., 2011. "*Similar damage initiation but different failure behavior in trabecular and cortical bone tissue*". Journal of the Mechanical Behavior of Biomedical Materials.

3. **Katsamenis, O. L.**, Jenkins, T., Michopoulou, S., Sinclair, I., Thurner, P. J., "*A Novel Videography Method for Generating Crack Extension Resistance Curves in Small Bone Samples*". PLoS one (under review)

4. **Katsamenis, O. L.**, Jenkins, T., Thurner, P. J., "*Multiscale Experimental Analysis of Human Bone Fracture Toughness: from the Osteonal up to the Tissue Level*" (in preparation)

Conference Abstracts and Proceedings

1. **O. L. Katsamenis**, T. Jenkins, S. Michopoulou, I. Sinclair, P. J. Thurner, "*Multiscale Experimental Analysis of Human Bone Fracture Toughness: From the Osteonal up to the Tissue Level*", Annual Meeting of the Orthopaedic Research Society (ORS), San Antonio TX, January 26 – 29, 2013

2. T. Jenkins, **O. L. Katsamenis**, P. J. Thurner, N. C. Harvey, S. Michopoulou, I. Sinclair, "*Whitening Front Tracking: A High-Speed Videography Method for Assessing Fracture Toughness of Small Bone Samples*", Annual Meeting of the Orthopaedic Research Society (ORS), San Antonio TX, January 26 – 29, 2013

3. **O. L. Katsamenis**, T. Jenkins, S. Michopoulou, I. Sinclair, P. J. Thurner, "*A Novel Method for Generating Crack Extension Resistance Curves in Small Bone Samples using High-Speed Videography*", Abstract at the 20th Annual Meeting of European Orthopaedics Research Society (EORS), Amsterdam September 26-28, 2012

4. P. J. Thurner, **O. L. Katsamenis**, S. Nobakhti, O. Andriotis, H. M. H. Chong, G. Limbert, "*Microstructure, Interfaces, Composition - Towards Better Microscale Experimentation and Models of Bone*", Abstract at the 6th European Congress on Computational Methods in Applied Sciences and Engineering (ECCOMAS 2012), Vienna, Austria, September 10-14, 2012

5. **O.L. Katsamenis**, O.G. Andriotis and P.J. Thurner, "*Distribution of nanoelasticity in osteonal level affects bone fracture toughness behaviour*", Abstracts at 18th Congress of the European Society of Biomechanics (ESB), Lisbon, Portugal, July 1-4, 2012

6. **Katsamenis, O.L.**, Taylor M., Thurner, P.J. "*Probing Laminar Bone's Behaviour by Means of AFM with in-situ Sample Stretching*" 2011 Scanning Probe Microscopy Meeting of the Royal Microscopical Society (RMS), Edinburgh, UK, June 22-23 2011.

7. **Katsamenis, O.L**., Taylor M., Thurner P.J. "*Nano- and Microcracking in Cortical Bone Captured with Time-lapsed Atomic Force Microscopy*", Annual Meeting of the Orthopaedic Research Society (ORS), Long Beach, LA, USA, January 13-16, 2011

8. **Katsamenis O.L.**, Boughen T., Thurner P. J., "*Imaging of Crack Propagation in Bone with Atomic Force Microscopy*", Abstracts 17th Congress of the European Society of Biomechanics (ESB), Edinburgh, UK, July 5-8, 1058, 2010

Other publications/technical report

1. P. J. Thurner and **O. L. Katsamenis**, "*Measuring forces between structural elements in composites, from macromolecule to bone",* Invited chapter in BIOMINERALIZATION HANDBOOK: Characterization of Biominerals and Biomimetic Materials, Edited by Laurie Gower and Elaine DiMasi, Taylor & Francis (in preparation)

2. **Katsamenis, O**., Boughen, T., Thurner, P.J., 2010, "*Crack Propagation in Bone Captured with In-Situ Mechanical Testing During AFM*";Technical report, Asylum Research website, http://www.asylumresearch.com/Applications/Applications.shtml

In addition to the above, throughout the past three years I worked at the University of Southampton as part of bioengineering research group the following publications have been produced from collaborations and parallel research activity:

Refereed Articles

1. **Katsamenis, O. L.**, Karoutsos, V., Kontostanos, K., Panagiotopoulos, E. C., Papadaki, H., & Bouropoulos, N. (2012). *Microstructural characterization of CPPD and hydroxyapatite crystal depositions on human menisci*. Crystal Research and Technology; 1-9 (2012), DOI: 10.1002/crat.201200346

2. Bouropoulos N., **Katsamenis O.L**., Cox P. A., Norman Z., Kallinteri P., Farvetto M. E., Yannopoulos S.N., Bakandritsos A. and Fatouros D. G.; 2012; "*Probing the Perturbation of Lecithin Bilayers by Unmodified C_{60} Fullerenes Using Experimental Methods and Computational Simulations*". The Journal of Physical Chemistry; 116 (6), pp 3867–3874

3. Capretto, L., Cheng, W., Carugo, D., **Katsamenis, O.L**., Hill, M., Zhang, X., 2012. "Mechanism of co-nanoprecipitation of organic actives and block copolymers in a microfluidic environment". Nanotechnology 23, 375602.

Conference Abstracts and Proceedings

1. J. Knychala, N. Bouropoulos, **O.L. Katsamenis**, B.G. Sengers, "Interaction between tissue growth, pore geometry and cell mechanics", Abstracts at 3rd *TERMIS World Congress, Vienna, September 5-8, 2012.*

2. S. Michopoulou, **O. L. Katsamenis**, R. Juliana, K. Venables, C. Hardiman, "Mechanical Isocentre Checks with Gantry Rotation Using a Mirror Jig", European Medical Physics and Engineering Conference (EMPEC) 2011, Dublin, Ireland, September 1-3, 2011

3. O. Andriotis, W. Manuyakorn, **O. Katsamenis**, P. H. Howarth, D. E. Davies, and P. J. Thurner. "*Structural and Mechanical Investigation of Human and Murine Collagen*" – 2011 Scanning Probe Microscopy Meeting of the Royal Microscopical Society (RMS), Edinburgh, UK, June 22-23 2011.

4. W. Manuyakorn, **O. Katsamenis**, T. Li, P. Thurner, D. Davies, P. Howarth. "*The structure and cross-linking of collagen in asthma*", Abstracts Congress of European Academy of Allergy and Clinical Immunology (EAACI), Istanbul, Turkey, June 11-15 2011

List of References / Bibliography

Adams, J., Fantner, G., Fisher, L., Hansma, P., 2008. "Molecular energy dissipation in nanoscale networks of dentin matrix protein 1 is strongly dependent on ion valence". *Nanotechnology 19, 384008*.

Ager, J.W., Balooch, G., Ritchie, R.O., 2006. "Fracture, aging, and disease in bone". *Journal of Materials Research 21, 1878-1892*.

Ascenzi, A., Baschieri, P., Benvenuti, A., 1990. "The bending properties of single osteons". *Journal of biomechanics 23, 763-771*.

Ascenzi, A., Baschieri, P., Benvenuti, A., 1994. "The torsional properties of single selected osteons". *Journal of biomechanics 27, 875-877, 879-884*.

Ascenzi, A., Benvenuti, A., 1986. "Orientation of collagen fibers at the boundary between two successive osteonic lamellae and its mechanical interpretation". *Journal of biomechanics 19, 455-463*.

Ascenzi, A., Benvenuti, A., Bonucci, E., 1982. "The tensile properties of single osteonic lamellae: technical problems and preliminary results". *Journal of biomechanics 15, 29-37*.

Ascenzi, A., Bonucci, E., 1964. "The ultimate tensile strength of single osteons". *Cells Tissues Organs 58, 160-183*.

Ascenzi, A., Bonucci, E., 1967. "The tensile properties of single osteons". *The Anatomical Record 158, 375-386*.

Ascenzi, A., Bonucci, E., 1968. "The compressive properties of single osteons". *The Anatomical Record 161, 377-391*.

Ascenzi, A., Bonucci, E., 1972. "The shearing properties of single osteons". *The Anatomical Record 172, 499-510*.

ASTM, 2004. "E 1820-01". *Standard Test Method for Measurement of Fracture Toughness. Annual Book of ASTM Standards, Section 03.01, 1-46*.

Baht, G.S., Hunter, G.K., Goldberg, H.A., 2008. "Bone sialoprotein-collagen interaction promotes hydroxyapatite nucleation". *Matrix Biology 27, 600-608*.

Balooch, M., Habelitz, S., Kinney, J., Marshall, S., Marshall, G., 2008. "Mechanical properties of mineralized collagen fibrils as influenced by demineralization". *Journal of Structural Biology 162, 404-410*.

Bigley, R.F., Griffin, L.V., Christensen, L., Vandenbosch, R., 2006. "Osteon interfacial strength and histomorphometry of equine cortical bone". *J Biomech 39, 1629-1640*.

Binnig, G., Quate, C.F., Gerber, C., 1986. "Atomic force microscope". *Phys Rev Lett 56, 930-933*.

Bonar, L.C., Lees, S., Mook, H., 1985. "Neutron diffraction studies of collagen in fully mineralized bone". *Journal of molecular biology 181, 265-270*.

Bonfield, W., 1968. "The temperature dependence of the deformation of bone". *Journal of Biomechanics 1, 323-329*.

Bonfield, W., 1987. "Advances in the fracture mechanics of cortical bone". *Journal of Biomechanics 20, 1071-1081*.

Boyce, T., Bloebaum, R., 1993. "Cortical aging differences and fracture implications for the human femoral neck". *Bone 14, 769-778*.

Braga, P., Ricci, D., 2004. "Atomic force microscopy: biomedical methods and applications. Humana Pr Inc.

Braidotti, P., Bemporad, E., D'alessio, T., Sciuto, S., Stagni, L., 2000a. "Tensile experiments and SEM fractography on bovine subchondral bone". *Journal of Biomechanics 33, 1153-1157*.

Braidotti, P., Bemporad, E., D'Alessio, T., Sciuto, S.A., Stagni, L., 2000b. "Tensile experiments and SEM fractography on bovine subchondral bone". *Journal of Biomechanics 33, 1153-1157.*

Braidotti, P., Branca, F., Stagni, L., 1997a. "Scanning electron microscopy of human cortical bone failure surfaces". *Journal of biomechanics 30, 155-162*.

Braidotti, P., Branca, F.P., Stagni, L., 1997b. "Scanning electron microscopy of human cortical bone failure surfaces". *Journal of Biomechanics 30, 155-162*.

Bukhari, M., 2009. "The National Osteoporosis Guideline Group's new guidelines: what is new?". *Rheumatology*.

Burr, D.B., Schaffler, M.B., Frederickson, R.G., 1988. "Composition of the cement line and its possible mechanical role as a local interface in human compact bone". *J Biomech 21, 939-945*.

Butt, H.J., Jaschke, M., 1995. "Calculation of thermal noise in atomic force microscopy". *Nanotechnology 6, 1*.

Chang, S., Wang, C., Xiong, C., Fang, J., 2005. "Nanoscale in-plane displacement evaluation by AFM scanning and digital image correlation processing". *Nanotechnology 16, 344*.

Courtney, A.C., Hayes, W.C., Gibson, L.J., 1996. "Age-related differences in post-yield damage in human cortical bone. Experiment and model". *Journal of Biomechanics 29, 1463-1471.*

Cowin, S., Telega, J., 2003. "Bone mechanics handbook". *Applied Mechanics Reviews 56, B61*.

Cowin, S.C., 2001. "Bone mechanics handbook. CRC press USA.

Cowin, S.C., Corporation, E., 2001. "Bone mechanics handbook. CRC press Boca Raton, FL.

Currey, J., 1984. "Effects of differences in mineralization on the mechanical properties of bone". *Philosophical Transactions of the Royal Society of London. B, Biological Sciences 304, 509-518*.

Currey, J.D., Brear, K., Zioupos, P., 1996. "The effects of ageing and changes in mineral content in degrading the toughness of human femora". *Journal of biomechanics 29, 257-260*.

Deal, C.L., 1997. "Osteoporosis: prevention, diagnosis, and management". *The American journal of medicine 102, 35S-39S*.

Denhardt, D.T., Guo, X., 1993. "Osteopontin: a protein with diverse functions". *The FASEB journal 7, 1475-1482*.

Derkx, P., Nigg, A., Bosman, F., Birkenhäger-Frenkel, D., Houtsmuller, A., Pols, H., Van Leeuwen, J., 1998. "Immunolocalization and quantification of noncollagenous bone matrix proteins in methylmethacrylate-embedded adult human bone in combination with histomorphometry". *Bone 22, 367-373*.

Deymier-Black, A., Yuan, F., Singhal, A., Almer, J., Brinson, L., Dunand, D., 2011. "Evolution of load transfer between hydroxyapatite and collagen during creep deformation of bone". *Acta Biomaterialia*.

Diez-Perez, A., Güerri, R., Nogues, X., Cáceres, E., Peña, M.J., Mellibovsky, L., Randall, C., Bridges, D., Weaver, J.C., Proctor, A., 2010. "Microindentation for in vivo measurement of bone tissue mechanical properties in humans". *Journal of Bone and Mineral Research 25, 1877-1885*.

Dong, X.N., Zhang, X., Guo, X.E., 2005. "Interfacial strength of cement lines in human cortical bone". *Mechanics & chemistry of biosystems : MCB 2, 63-68*.

Donnelly, E., Baker, S.P., Boskey, A.L., van der Meulen, M.C.H., 2006. "Effects of surface roughness and maximum load on the mechanical properties of cancellous bone measured by nanoindentation". *Journal of Biomedical Materials Research Part A 77, 426-435*.

Eanes, E.D., 1992. "Dynamics of calcium phosphate precipitation". *Calcification in biological systems. CRC Press, Boca Raton, FL, 1-18*.

Ebacher, V., Guy, P., Oxland, T.R., Wang, R., 2011. "Sub-Lamellar Microcracking and Roles of Canaliculi in Human Cortical Bone". *Acta Biomaterialia*.

Ebacher, V., Wang, R., 2009. "A unique microcracking process associated with the inelastic deformation of Haversian bone". *Advanced Functional Materials 19, 57-66*.

Espinosa, H.D., Juster, A.L., Latourte, F.J., Loh, O.Y., Gregoire, D., Zavattieri, P.D., 2011. "Tablet-level origin of toughening in abalone shells and translation to synthetic composite materials". *Nature Communications 2, 173*.

Evans, A., Faber, K., 1984. "Crack - Growth Resistance of Microcracking Brittle Materials". *Journal of the American Ceramic Society 67, 255-260*.

Eyre, D., Dickson, I., Van Ness, K., 1988. "Collagen cross-linking in human bone and articular cartilage. Age-related changes in the content of mature hydroxypyridinium residues". *Biochemical Journal 252, 495*.

Fantner, G.E., Adams, J., Turner, P., Thurner, P.J., Fisher, L.W., Hansma, P.K., 2007. "Nanoscale ion mediated networks in bone: osteopontin can repeatedly dissipate large amounts of energy". *Nano Letters 7, 2491-2498*.

Fantner, G.E., Hassenkam, T., Kindt, J.H., Weaver, J.C., Birkedal, H., Pechenik, L., Cutroni, J.A., Cidade, G.A.G., Stucky, G.D., Morse, D.E., 2005a. "Sacrificial bonds and hidden length dissipate energy as mineralized fibrils separate during bone fracture". *Nature Materials 4, 612-616*.

Fantner, G.E., Hassenkam, T., Kindt, J.H., Weaver, J.C., Birkedal, H., Pechenik, L., Cutroni, J.A., Cidade, G.A.G., Stucky, G.D., Morse, D.E., Hansma, P.K., 2005b. "Sacrificial bonds and hidden length dissipate energy as mineralized fibrils separate during bone fracture". *Nature Materials 4, 612-616*.

Feldkamp, L.A., Goldstein, S.A., Parfitt, M.A., Jesion, G., Kleerekoper, M., 2009. "The direct examination of three - dimensional bone architecture in vitro by computed tomography". *Journal of Bone and Mineral Research 4, 3-11*.

Felsenberg, D., Boonen, S., 2005. "The bone quality framework: determinants of bone strength and their interrelationships, and implications for osteoporosis management". *Clinical Therapeutics 27, 1-11*.

Fisher, L., Torchia, D., Fohr, B., Young, M., Fedarko, N., 2001. "Flexible structures of SIBLING proteins, bone sialoprotein, and osteopontin". *Biochemical and biophysical research communications 280, 460-465*.

Franzoso, G., Zysset, P.K., 2009. "Elastic anisotropy of human cortical bone secondary osteons measured by nanoindentation". *Journal of Biomechanical Engineering 131, 021001*.

Fratzl, P., 2008a. "Bone fracture: When the cracks begin to show". *Nature Materials 7, 610*.

Fratzl, P., 2008b. "Collagen: structure and mechanics. Springer Heidelberg:.

Fratzl, P., Gupta, H., Paschalis, E., Roschger, P., 2004. "Structure and mechanical quality of the collagen–mineral nano-composite in bone". *Journal of Materials Chemistry 14, 2115-2123*.

Fratzl, P., Weinkamer, R., 2007. "Nature's hierarchical materials". *Progress in Materials Science 52, 1263-1334*.

Fujisawa, R., Kuboki, Y., 1991. "Preferential adsorption of dentin and bone acidic proteins on the (100) face of hydroxyapatite crystals". *Biochimica et Biophysica Acta (BBA)-General Subjects 1075, 56-60*.

Garnero, P., Borel, O., Gineyts, E., Duboeuf, F., Solberg, H., Bouxsein, M.L., Christiansen, C., Delmas, P.D., 2006. "Extracellular post-translational modifications of collagen are major determinants of biomechanical properties of fetal bovine cortical bone". *Bone 38, 300-309*.

Giraud-Guille, M., 1988. "Twisted plywood architecture of collagen fibrils in human compact bone osteons". *Calcified tissue international 42, 167-180*.

Goldberg, H.A., Warner, K.J., Li, M.C., Hunter, G.K., 2001. "Binding of bone sialoprotein, osteopontin and synthetic polypeptides to hydroxyapatite". *Connective tissue research 42, 25-37*.

Gray, H., Standring, S., 2005. "Gray's Anatomy: The Anatomical Basis of Clinical Practice, ed 39".

Greenspan, S.L., Myers, E.R., Maitland, L.A., Resnick, N.M., Hayes, W.C., 1994. "Fall severity and bone mineral density as risk factors for hip fracture in ambulatory elderly". *JAMA: the journal of the American Medical Association 271, 128-133*.

Grynpas, M.D., Tupy, J.H., Sodek, J., 1994. "The Distribution of Soluble, Mineral-Bound, and Matrix-Bound Proteins in Osteoporotic and Normal Bones". *Bone 15, 505-513*.

Guizar-Sicairos, M., Thurman, S.T., Fienup, J.R., 2008. "Efficient subpixel image registration algorithms". *Optics Letters 33, 156-158*.

Gupta, H., Stachewicz, U., Wagermaier, W., Roschger, P., Wagner, H., Fratzi, P., 2006a. "Mechanical modulation at the lamellar level in osteonal bone". *Journal of Materials Research 21, 1913-1921*.

Gupta, H.S., Fratzl, P., Kerschnitzki, M., Benecke, G., Wagermaier, W., Kirchner, H.O.K., 2007. "Evidence for an elementary process in bone plasticity with an activation enthalpy of 1 eV". *Journal of the Royal Society Interface 4, 277-282*.

Gupta, H.S., Seto, J., Wagermaier, W., Zaslansky, P., Boesecke, P., Fratzl, P., 2006b. "Cooperative deformation of mineral and collagen in bone at the nanoscale". *Proceedings of the National Academy of Sciences 103, 17741*.

Gupta, H.S., Seto, J., Wagermaier, W., Zaslansky, P., Boesecke, P., Fratzl, P., 2006c. "Cooperative deformation of mineral and collagen in bone at the nanoscale". *Proc Natl Acad Sci U S A 103, 17741-17746*.

Gupta, H.S., Wagermaier, W., Zickler, G.A., Aroush, D.R.B., Funari, S.S., Roschger, P., Wagner, H.D., Fratzl, P., 2005. "Nanoscale deformation mechanisms in bone". *Nano Letters 5, 2108-2111*.

Hamed, E., Lee, Y., Jasiuk, I., 2010. "Multiscale modeling of elastic properties of cortical bone". *Acta Mechanica 213, 131-154*.

Hang, F., Barber, A.H., 2011. "Nano-mechanical properties of individual mineralized collagen fibrils from bone tissue". *Journal of the Royal Society Interface 8, 500*.

Hansma, P., Turner, P., Drake, B., Yurtsev, E., Proctor, A., Mathews, P., Lelujian, J., Randall, C., Adams, J., Jungmann, R., 2008. "The bone diagnostic instrument II: Indentation distance increase". *Review of Scientific Instruments 79, 064303-064303-064308*.

Hansma, P.K., Turner, P.J., Fantner, G.E., 2006. "Bone diagnostic instrument". *Review of Scientific Instruments 77, 075105-075105-075106*.

Hengsberger, S., Kulik, A., Zysset, P., 2002. "Nanoindentation discriminates the elastic properties of individual human bone lamellae under dry and physiological conditions". *Bone 30, 178-184*.

Hiller, L., Stover, S., Gibson, V., Gibeling, J., Prater, C., Hazelwood, S., Yeh, O., Martin, R., 2006. "Osteon pullout in the equine third metacarpal bone: effects of ex vivo fatigue". *Journal of Orthopaedic Research 21, 481-488*.

Hofmann, T., Heyroth, F., Meinhard, H., Fränzel, W., Raum, K., 2006. "Assessment of composition and anisotropic elastic properties of secondary osteon lamellae". *Journal of biomechanics 39, 2282-2294*.

Hollinger, J., 2005. "Bone tissue engineering. CRC.

Hui, S.L., Slemenda, C.W., Johnston Jr, C.C., 1988. "Age and bone mass as predictors of fracture in a prospective study". *Journal of Clinical Investigation 81, 1804*.

Hunter, G.K., Goldberg, H.A., 1993. "Nucleation of hydroxyapatite by bone sialoprotein". *Proceedings of the National Academy of Sciences 90, 8562*.

Ilich, J.Z., Kerstetter, J.E., 2000. "Nutrition in bone health revisited: A story beyond calcium". *Journal of the American College of Nutrition 19, 715-737*.

Jee, A.Y., Lee, M., 2010. "Comparative analysis on the nanoindentation of polymers using atomic force microscopy". *Polymer Testing 29, 95-99*.

Jena, B., Hörber, J., 2006. "Force microscopy: applications in biology and medicine. John Wiley and Sons.

Jepsen, K.J., Davy, D.T., Krzypow, D.J., 1999. "The role of the lamellar interface during torsional yielding of human cortical bone". *Journal of biomechanics 32, 303-310*.

Jepsen, K.J., Pennington, D.E., Lee, Y.L., Warman, M., Nadeau, J., 2001. "Bone brittleness varies with genetic background in A/J and C57BL/6J inbred mice". *Journal of Bone and Mineral Research 16, 1854-1862*.

Kammers, A., Daly, S., 2011. "Small-scale patterning methods for digital image correlation under scanning electron microscopy". *Measurement Science and Technology 22, 125501*.

Kanis, J.A., 2002a. "Diagnosis of osteoporosis and assessment of fracture risk". *The Lancet 359, 1929-1936*.

Kanis, J.A., 2002b. "Diagnosis of osteoporosis and assessment of fracture risk". *Lancet (London, England) 359, 1929-1936*.

Kanis, J.A. 2007 Kanis, J.A., 2007. Assessment of Osteoporosis at the Primary Health Care Level. World Health Organisation Collaborating Centre for Metabolic Bone Diseases, University of Sheffield, p. 339.

Kanis, J.A., 2008. "Assessment of osteoporosis at the primary health care level. WHO Collaborating Centre for Metabolic Bone Diseases, University of Sheffield Medical School.

Kanis, J.A., Borgstrom, F., De Laet, C., Johansson, H., Johnell, O., Jonsson, B., Oden, A., Zethraeus, N., Pfleger, B., Khaltaev, N., 2005a. "Assessment of fracture risk". *Osteoporosis International 16, 581-589*.

Kanis, J.A., Johansson, H., Johnell, O., Oden, A., De Laet, C., Eisman, J.A., Pols, H., Tenenhouse, A., 2005b. "Alcohol intake as a risk factor for fracture". *Osteoporosis International 16, 737-742*.

Kanis, J.A., Johnell, O., Oden, A., Johansson, H., De Laet, C., Eisman, J.A., Fujiwara, S., Kroger, H., McCloskey, E.V., Mellstrom, D., Melton, L.J., Pols, H., Reeve, J., Silman, A., Tenenhouse, A., 2005c. "Smoking and fracture risk: a meta-analysis". *Osteoporosis International 16, 155-162*.

Kasas, S., Thomson, N., Smith, B., Hansma, P., Miklossy, J., Hansma, H., 1997. "Biological applications of the AFM: from single molecules to organs". *International journal of imaging systems and technology 8, 151-161*.

Katsamenis, O., Boughen, T., Thurner, P.J. 2010 Katsamenis, O., Boughen, T., Thurner, P.J., 2010. Crack Propagation in Bone Captured with In-Situ Mechanical Testing During AFM. Asylum Research, http://www.asylumresearch.com/Applications/Applications.shtml.

Katsamenis, O.L., Chong, H.M.H., Andriotis, O.G., Thurner, P.J., 2012. "Load-Bearing in Cortical Bone Microstructure: Selective Stiffening and Heterogeneous Strain Distribution at the Lamellar Level". *Journal of the Mechanical Behavior of Biomedical Materials*.

Kazanci, M., Roschger, P., Paschalis, E., Klaushofer, K., Fratzl, P., 2006. "Bone osteonal tissues by Raman spectral mapping: orientation-composition". *Journal of Structural Biology 156, 489-496*.

Kazanci, M., Wagner, H., Manjubala, N., Gupta, H., Paschalis, E., Roschger, P., Fratzl, P., 2007. "Raman imaging of two orthogonal planes within cortical bone". *Bone 41, 456-461*.

Keaveny, T.M., Morgan, E.F., Niebur, G.L., Yeh, O.C., 2001. "Biomechanics of trabecular bone". *Annual Review of Biomedical Engineering 3, 307-333*.

Keller, D., Franke, F., 1993. "Envelope reconstruction of probe microscope images". *Surface Science 294, 409-419*.

Kelly, J.M., 2002. "Seismic isolation systems for developing countries". *Earthquake spectra 18, 385*.

Kennedy, O.D., Lendhey, M., Basta-Pljakic, J., Schaffler, M.B. 2012 Kennedy, O.D., Lendhey, M., Basta-Pljakic, J., Schaffler, M.B., 2012. Reference Point Indentation in Bone Provides a Reliable Measure Related to Fracture Toughness. ORS 2012 Annual Meeting, San Francisco, California.

Khosla, S., Melton, L.J., Atkinson, E.J., O'fallon, W., Klee, G.G., Riggs, B.L., 1998. "Relationship of serum sex steroid levels and bone turnover markers with bone mineral density in men and women: a key role for bioavailable estrogen". *Journal of Clinical Endocrinology & Metabolism 83, 2266-2274*.

Kiel, D.P., Felson, D.T., Hannan, M.T., Anderson, J.J., Wilson, P.W.F., 1990. "CAFFEINE AND THE RISK OF HIP FRACTURE - THE FRAMINGHAM-STUDY". *American Journal of Epidemiology 132, 675-684*.

Kirkham, J., Zhang, J., Brookes, S., Shore, R., Wood, S., Smith, D., Wallwork, M., Ryu, O., Robinson, C., 2000a. "Evidence for charge domains on developing enamel crystal surfaces". *Journal of dental research 79, 1943-1947*.

Kirkham, J., Zhang, J., Brookes, S., Shore, R., Wood, S., Smith, D., Wallwork, M., Ryu, O., Robinson, C., 2000b. "Evidence for charge domains on developing enamel crystal surfaces". *Journal of Dental Research 79, 1943*.

Koester, K.J., Ager, J., Ritchie, R., 2008. "The true toughness of human cortical bone measured with realistically short cracks". *Nature Materials 7, 672-677*.

Kruzic, J.J., Kuskowski, S.J., Ritchie, R.O., 2005. "Simple and accurate fracture toughness testing methods for pyrolytic carbon/graphite composites used in heart-valve prostheses". *Journal of Biomedical Materials Research Part A 74A, 461-464*.

Lakes, R.S., Katz, J.L., Sternstein, S.S., 1979. "Viscoelastic properties of wet cortical bone—I. Torsional and biaxial studies". *Journal of biomechanics 12, 657-678*.

Landis, W., Song, M., Leith, A., McEwen, L., McEwen, B., 1993a. "Mineral and organic matrix interaction in normally calcifying tendon visualized in three dimensions by high-voltage electron microscopic tomography and graphic image reconstruction". *Journal of Structural Biology 110, 39-54*.

Landis, W.J., Song, M.J., Leith, A., Mcewen, L., Mcewen, B.F., 1993b. "Mineral and Organic Matrix Interaction in Normally Calcifying Tendon Visualized in 3 Dimensions by High-Voltage Electron-Microscopic Tomography and Graphic Image-Reconstruction". *Journal of Structural Biology 110, 39-54*.

Launey, M.E., Buehler, M.J., Ritchie, R.O., 2010. "On the mechanistic origins of toughness in bone". *Annual Review of Materials Research 40, 25-53*.

LeGeros, Z., 1981. "Apatites in biological systems". *Progress in Crystal Growth and Characterization 4, 1-45*.

Leng, H., Wang, X., Ross, R.D., Niebur, G.L., Roeder, R.K., 2008. "Micro-computed tomography of fatigue microdamage in cortical bone using a barium sulfate contrast agent". *Journal of the Mechanical Behavior of Biomedical Materials 1, 68-75*.

Lewis, I., Edwards, H., 2001. "Handbook of Raman spectroscopy: from the research laboratory to the process line. CRC.

Li, B., Aspden, R., 1997. "Material properties of bone from the femoral neck and calcar femorale of patients with osteoporosis or osteoarthritis". *Osteoporosis International 7, 450-456*.

Lieber, C.A., Mahadevan-Jansen, A., 2003. "Automated method for subtraction of fluorescence from biological Raman spectra". *Applied Spectroscopy 57, 1363-1367*.

Liebschner, M.A.K., 2004. "Biomechanical considerations of animal models used in tissue engineering of bone". *Biomaterials 25, 1697-1714*.

Linde, F., Sørensen, H.C.F., 1993. "The effect of different storage methods on the mechanical properties of trabecular bone". *Journal of biomechanics 26, 1249-1252*.

Liu, J., Iskander, M. 2010 Liu, J., Iskander, M., 2010. Digital Image Correlation. Modelling with Transparent Soils. Springer Berlin Heidelberg, pp. 137-164.

Loparic, M., Wirz, D., Daniels, A., Raiteri, R., VanLandingham, M.R., Guex, G., Martin, I., Aebi, U., Stolz, M., 2010. "Micro-and Nanomechanical Analysis of Articular Cartilage by Indentation-Type Atomic Force Microscopy: Validation with a Gel-Microfiber Composite". *Biophysical Journal 98, 2731-2740*.

Malik, C.L., Stover, S.M., Martin, R.B., Gibeling, J.C., 2003. "Equine cortical bone exhibits rising R-curve fracture mechanics". *Journal of Biomechanics 36, 191-198*.

Marcus, R., Feldman, D., ROSEN, C., NELSON, D., 2009. "Osteoporosis, (two-volume set)". *American Journal of Neuroradiology 30, E138*.

Marotti, G., 1993. "A new theory of bone lamellation". *Calcified tissue international 53, 47-56*.

Marshall, D., Johnell, O., Wedel, H., 1996. "Meta-analysis of how well measures of bone mineral density predict occurrence of osteoporotic fractures". *BMJ 312, 1254-1259*.

Martin, R., Gibson, V., Stover, S., Gibeling, J., Griffins, L., 1996. "Osteonal structure in the equine third metacarpus". *Bone 19, 165-171*.

McCalden, R., McGeough, J., Barker, M., 1993. "Age-related changes in the tensile properties of cortical bone. The relative importance of changes in porosity, mineralization, and microstructure". *The Journal of bone and joint surgery. American volume 75, 1193*.

McKee, M., Nanci, A., Landis, W., Gerstenfeld, L., Gotoh, Y., Glimcher, M., 1989. "Ultrastructural immunolocalization of a major phosphoprotein in embryonic chick bone". *Connective tissue research 21, 21-29*.

McKee, M.D., Farach - Carson, M., Butler, W., Hauschka, P., Nanci, A., 1993. "Ultrastructural immunolocalization of noncollagenous (osteopontin and osteocalcin) and plasma (albumin and α2HS - glycoprotein) proteins in rat bone". *Journal of Bone and Mineral Research 8, 485-496*.

Meyer, E., 1992. "Atomic force microscopy". *Progress in Surface Science 41, 3-49*.

Meyer, G., Amer, N., 1988. "Novel optical approach to atomic force microscopy". *Applied Physics Letters 53, 1045*.

Miller, S., Jee, W., 1987. "The bone lining cell: A distinct phenotype?". *Calcified Tissue International 41, 1-5*.

Minary-Jolandan, M., Yu, M.F., 2009. "Nanomechanical heterogeneity in the gap and overlap regions of type I collagen fibrils with implications for bone heterogeneity". *Biomacromolecules 10, 2565-2570*.

Ming-Yuan, H., Hutchinson, J.W., 1989. "Crack deflection at an interface between dissimilar elastic materials". *International Journal of Solids and Structures 25, 1053-1067*.

Morris, M.D., Finney, W.F., 2004. "Recent developments in Raman and infrared spectroscopy and imaging of bone tissue". *spectroscopy 18, 155-159*.

Movasaghi, Z., Rehman, S., Rehman, I., 2007a. "Raman spectroscopy of biological tissues". *Applied Spectroscopy Reviews 42, 493-541*.

Movasaghi, Z., Rehman, S., Rehman, I.U., 2007b. "Raman spectroscopy of biological tissues". *Applied Spectroscopy Reviews 42, 493-541*.

Nakamoto, K., 1986. "Infrared and Raman spectra of inorganic and coordination compounds". *Handbook of Vibrational Spectroscopy*.

Nakashima, M., Pan, P., Zamfirescu, D., Weitzmann, R., 2004. "Post-Kobe approach for design and construction of base-isolated buildings". *Journal of Japan Association for Earthquake Engineering 4*.

Nalla, R.K., Kinney, J.H., Ritchie, R.O., 2003. "Mechanistic fracture criteria for the failure of human cortical bone". *Nature Materials 2, 164-168*.

Nalla, R.K., Kruzic, J.J., Kinney, J.H., Ritchie, R.O., 2005. "Mechanistic aspects of fracture and R-curve behavior in human cortical bone". *Biomaterials 26, 217-231*.

Nalla, R.K., Kruzic, J.J., Ritchie, R.O., 2004. "On the origin of the toughness of mineralized tissue: microcracking or crack bridging?". *Bone 34, 790-798*.

Nanci, A., 1999. "Content and distribution of noncollagenous matrix proteins in bone and cementum: relationship to speed of formation and collagen packing density". *Journal of Structural Biology 126, 256-269*.

Naraghi, M., Filleter, T., Moravsky, A., Locascio, M., Loutfy, R.O., Espinosa, H.D., "A Multiscale Study of High Performance Double-Walled Nanotube- Polymer Fibers". *ACS Nano, 2212-2215*.

Nordin, M., Frankel, V., 2001. "Basic biomechanics of the musculoskeletal system. Lippincott Williams & Wilkins.

Nyman, J.S., Reyes, M., Wang, X., 2005. "Effect of ultrastructural changes on the toughness of bone". *Micron 36, 566-582*.

O'Brien, F., Taylor, D., Lee, T., 2003. "Microcrack accumulation at different intervals during fatigue testing of compact bone". *Journal of Biomechanics 36, 973-980*.

Oliver, W., Pharr, G., 2004. "Measurement of hardness and elastic modulus by instrumented indentation: Advances in understanding and refinements to methodology". *J. Mater. Res 19*.

Oliver, W.C., Pharr, G.M., 1992. "An Improved Technique for Determining Hardness and Elastic-Modulus Using Load and Displacement Sensing Indentation Experiments". *Journal of Materials Research 7, 1564-1583*.

Olszta, M.J., Cheng, X., Jee, S.S., Kumar, R., Kim, Y.Y., Kaufman, M.J., Douglas, E.P., Gower, L.B., 2007. "Bone structure and formation: A new perspective". *Materials Science and Engineering: R: Reports 58, 77-116*.

Pan, B., Qian, K., Xie, H., Asundi, A., 2009. "Two-dimensional digital image correlation for in-plane displacement and strain measurement: a review". *Measurement Science and Technology 20, 062001*.

Paschalis, E.P., Shane, E., Lyritis, G., Skarantavos, G., Mendelsohn, R., Boskey, A.L., 2004. "Bone Fragility and Collagen Cross - Links". *Journal of Bone and Mineral Research 19, 2000-2004*.

Pazzaglia, U.E., Congiu, T., Marchese, M., Spagnuolo, F., Quacci, D., 2012. "Morphometry and Patterns of Lamellar Bone in Human Haversian Systems". *The Anatomical Record: Advances in Integrative Anatomy and Evolutionary Biology*.

Pelker, R.R., Friedlaender, G.E., Markham, T.C., Panjabi, M.M., Moen, C.J., 2005. "Effects of freezing and freeze - drying on the biomechanical properties of rat bone". *Journal of Orthopaedic Research 1, 405-411*.

Peterlik, H., Roschger, P., Klaushofer, K., Fratzl, P., 2005. "From brittle to ductile fracture of bone". *Nature Materials 5, 52-55*.

Phelps, J., Hubbard, G., Wang, X., Agrawal, C., 2000. "Microstructural heterogeneity and the fracture toughness of bone". *Journal of Biomedical Materials Research 51, 735-741*.

Pidaparti, R., Chandran, A., Takano, Y., Turner, C., 1996. "Bone mineral lies mainly outside collagen fibrils: Predictions of a composite model for osternal bone". *Journal of biomechanics 29, 909-916*.

Pukánszky, B., Mudra, I., Staniek, P., 1997. "Relation of crystalline structure and mechanical properties of nucleated polypropylene". *Journal of Vinyl and Additive Technology 3, 53-57*.

Randall, C., Mathews, P., Yurtsev, E., Sahar, N., Kohn, D., Hansma, P., 2009. "The bone diagnostic instrument III: Testing mouse femora". *Review of Scientific Instruments 80, 065108-065108-065103*.

Reid, S.A., 1986. "A study of lamellar organisation in juvenile and adult human bone". *Anatomy and Embryology 174, 329-338*.

Reilly, D.T., Burstein, A.H., 1974. "Review article. The mechanical properties of cortical bone". *The Journal of bone and joint surgery. American volume 56, 1001*.

Rho, J., Kuhn-Spearing, L., Zioupos, P., 1998a. "Mechanical properties and the hierarchical structure of bone". *Medical Engineering & Physics 20, 92-102*.

Rho, J., Zioupos, P., Currey, J., Pharr, G., 1999. "Variations in the individual thick lamellar properties within osteons by nanoindentation". *Bone 25, 295-300*.

Rho, J.Y., 1996. "An ultrasonic method for measuring the elastic properties of human tibial cortical and cancellous bone". *Ultrasonics 34, 777-783*.

Rho, J.Y., Kuhn-Spearing, L., Zioupos, P., 1998b. "Mechanical properties and the hierarchical structure of bone". *Medical Engineering & Physics 20, 92-102*.

Rho, J.Y., Pharr, G.M., 1999. "Effects of drying on the mechanical properties of bovine femur measured by nanoindentation". *Journal of Materials Science: Materials in Medicine 10, 485-488*.

Riggs, B., Melton, L., 1995. "The worldwide problem of osteoporosis: insights afforded by epidemiology". *Bone 17, S505-S511*.

Riggs, B.L., Khosla, S., Melton, L.J., 2002. "Sex steroids and the construction and conservation of the adult skeleton". *Endocrine Reviews 23, 279-302*.

Ritchie, R., Koester, K., Ionova, S., Yao, W., Lane, N., Ager III, J., 2008. "Measurement of the toughness of bone: A tutorial with special reference to small animal studies". *Bone 43, 798-812*.

Ritchie, R.O., Buehler, M.J., Hansma, P., 2009. "Plasticity and toughness in bone". *Phys. Today 62, 41–47*.

Ritchie, R.O., Kinney, J.H., Kruzic, J.J., Nalla, R.K., 2005. "A fracture mechanics and mechanistic approach to the failure of cortical bone". *Fatigue & Fracture of Engineering Materials & Structures 28, 345-371*.

Roach, H., 1994a. "WHY DOES BONE MATRIX CONTAIN NON-COLLAGENOUS PROTEINS '? THE POSSIBLE ROLES or OSTEOCALCIN, OSTEONECTIN, OSTEOPONTIN AND BONE SIALOPROTEIN IN BONE MINERALISATION AND RESORPTION".

Roach, H., 1994b. "Why does bone matrix contain non-collagenous proteins? The possible roles of osteocalcin, osteonectin, osteopontin and bone sialoprotein in bone mineralisation and resorption". *Cell Biology International 18, 617-628*.

Robling, A.G., Castillo, A.B., Turner, C.H., 2006. "Biomechanical and molecular regulation of bone remodeling". *Annual Review of Biomedical Engineering 8, 455-498*.

Roe, B.P., 2001. "Probability and statistics in experimental physics. Springer.

Sader, J.E., Chon, J.W.M., Mulvaney, P., 1999. "Calibration of rectangular atomic force microscope cantilevers". *Review of Scientific Instruments 70, 3967*.

Sasaki, N., Matsushima, N., Ikawa, T., Yamamura, H., Fukuda, A., 1989. "Orientation of bone mineral and its role in the anisotropic mechanical properties of bone--transverse anisotropy". *Journal of biomechanics 22, 157-159, 161-164*.

Schaffler, M., Choi, K., Milgrom, C., 1995. "Aging and matrix microdamage accumulation in human compact bone". *Bone 17, 521-525*.

Schaffler, M.B., Burr, D.B., Frederickson, R.G., 1987. "Morphology of the osteonal cement line in human bone". *The Anatomical record 217, 223-228*.

Schuit, S.C.E., van der Klift, M., Weel, A.E.A.M., de Laet, C.E.D.H., Burger, H., Seeman, E., Hofman, A., Uitterlinden, A.G., van Leeuwen, J.P.T.M., Pols, H.A.P., 2004. "Fracture incidence and association with bone mineral density in elderly men and women: the Rotterdam Study". *Bone 34, 195-202*.

Seto, J., Gupta, H.S., Zaslansky, P., Wagner, H.D., Fratzl, P., 2008. "Tough lessons from bone: extreme mechanical anisotropy at the mesoscale". *Advanced Functional Materials 18, 1905-1911*.

Siris, E.S., Chen, Y.T., Abbott, T.A., Barrett-Connor, E., Miller, P.D., Wehren, L.E., Berger, M.L., 2004a. "Bone mineral density thresholds for pharmacological intervention to prevent fractures". *Archives of Internal Medicine 164, 1108-1112*.

Siris, E.S., Chen, Y.T., Abbott, T.A., Barrett-Connor, E., Miller, P.D., Wehren, L.E., Berger, M.L., 2004b. "Bone mineral density thresholds for pharmacological intervention to prevent fractures". *Archives of Internal Medicine 164, 1108*.

Skedros, J.G., Kiser, C.J., Keenan, K.E., Thomas, S.C., 2011. "Analysis of osteon morphotype scoring schemes for interpreting load history: evaluation in the chimpanzee femur". *Journal of Anatomy 218, 480-499*.

Skoog, D., Holler, F., Nieman, T., 2000. "Αρχές Ενόργανης Ανάλυσης". *Έκδοση 5η, εκδόσεις Κωσταράκη, 304-320*.

Smith, J., 1960. "Collagen fibre patterns in mammalian bone". *Journal of Anatomy 94, 329*.

Smith, J., Walmsley, R., 1959. "Factors affecting the elasticity of bone". *Journal of Anatomy 93, 503*.

Sun, X., Hoon Jeon, J., Blendell, J., Akkus, O., 2010. "Visualization of a phantom post-yield deformation process in cortical bone". *Journal of biomechanics 43, 1989-1996*.

Szabó, M., Zekonyte, J., Katsamenis, O., Taylor, M., Thurner, P., 2011. "Similar damage initiation but different failure behavior in trabecular and cortical bone tissue". *Journal of the Mechanical Behavior of Biomedical Materials*.

Tai, K., Dao, M., Suresh, S., Palazoglu, A., Ortiz, C., 2007. "Nanoscale heterogeneity promotes energy dissipation in bone". *Nature Materials 6, 454-462*.

Thurner, P., 2009. "Atomic force microscopy and indentation force measurement of bone". *Wiley Interdisciplinary Reviews: Nanomedicine and Nanobiotechnology 1, 624-649*.

Thurner, P., Chen, C., Ionova-Martin, S., Sun, L., Harman, A., Porter, A., Ager 3rd, J., Ritchie, R., Alliston, T., 2010a. "Osteopontin deficiency increases bone fragility but preserves bone mass". *Bone*.

Thurner, P., Lam, S., Weaver, J., Morse, D., Hansma, P., 2009. "Localization of phosphorylated serine, osteopontin, and bone sialoprotein on mineralized collagen fibrils in bone". *J. Adhes 85, 526–545*.

Thurner, P.J., Chen, C.G., Ionova-Martin, S., Sun, L., Harman, A., Porter, A., Ager III, J.W., Ritchie, R.O., Alliston, T., 2010b. "Osteopontin deficiency increases bone fragility but preserves bone mass". *Bone 46, 1564-1573*.

Thurner, P.J., Erickson, B., Jungmann, R., Schriock, Z., Weaver, J.C., Fantner, G.E., Schitter, G., Morse, D.E., Hansma, P.K., 2007. "High-speed photography of compressed human trabecular bone correlates whitening to microscopic damage". *Engineering fracture mechanics 74, 1928-1941*.

Tremollieres, F.A., Pouilles, J.-M., Drewniak, N., Laparra, J., Ribot, C.A., Dargent-Molina, P., 2010. "Fracture Risk Prediction Using BMD and Clinical Risk Factors in Early Postmenopausal Women: Sensitivity of the WHO FRAX Tool". *Journal of Bone and Mineral Research 25, 1002-1009*.

Tsuda, H., Arends, J., 1994. "Orientational micro-Raman spectroscopy on hydroxyapatite single crystals and human enamel crystallites". *Journal of dental research 73, 1703*.

Tye, C.E., Hunter, G.K., Goldberg, H.A., 2005. "Identification of the type I collagen-binding domain of bone sialoprotein and characterization of the mechanism of interaction". *Journal of Biological Chemistry 280, 13487*.

Ulrich, D., Hildebrand, T., Van Rietbergen, B., Müller, R., Rüegsegger, P., 1997a. "The quality of trabecular bone evaluated with micro-computed tomography, FEA and mechanical testing". *Studies in Health Technology and Informatics, 97-112*.

Ulrich, D., Hildebrand, T., Van Rietbergen, B., Müller, R., Rüegsegger, P., 1997b. "The quality of trabecular bone evaluated with micro-computed tomography, FEA and mechanical testing". *Studies in Health Technology and Informatics 40, 97-112*.

Vashishth, D., 2004. "Rising crack-growth-resistance behavior in cortical bone:: implications for toughness measurements". *Journal of biomechanics 37, 943-946*.

Vashishth, D., 2007. "Hierarchy of bone microdamage at multiple length scales". *International journal of fatigue 29, 1024-1033*.

Vashishth, D., Behiri, J., Bonfield, W., 1997. "Crack growth resistance in cortical bone: concept of microcrack toughening". *Journal of biomechanics 30, 763-769*.

Vaughan, T., McCarthy, C., McNamara, L., 2012. "A three-scale finite element investigation into the effects of tissue mineralisation and lamellar organisation in human cortical and trabecular bone". *Journal of the Mechanical Behavior of Biomedical Materials*.

Viguet-Carrin, S., Garnero, P., Delmas, P., 2006. "The role of collagen in bone strength". *Osteoporosis International 17, 319-336*.

Viswanath, B., Raghavan, R., Ramamurty, U., Ravishankar, N., 2007. "Mechanical properties and anisotropy in hydroxyapatite single crystals". *Scripta Materialia 57, 361-364*.

Wagermaier, W., Gupta, H., Gourrier, A., Burghammer, M., Roschger, P., Fratzl, P., 2006. "Spiral twisting of fiber orientation inside bone lamellae". *Biointerphases 1, 1*.

Wallwork, M., Kirkham, J., Chen, H., Chang, S., Robinson, C., Smith, D., Clarkson, B., 2002. "Binding of dentin noncollagenous matrix proteins to biological mineral crystals: an atomic force microscopy study". *Calcified tissue international 71, 249-256*.

Wang, X., Puram, S., 2004. "The toughness of cortical bone and its relationship with age". *Annals of Biomedical Engineering 32, 123-135*.

Wang, X., Shen, X., Li, X., Mauli Agrawal, C., 2002. "Age-related changes in the collagen network and toughness of bone". *Bone 31, 1-7.*

Weiner, S., Traub, W., 1992. "Bone structure: from angstroms to microns". *The FASEB journal 6, 879-885*.

Weiner, S., Traub, W., Wagner, H.D., 1999. "Lamellar bone: structure-function relations". *Journal of Structural Biology 126, 241-255*.

Weiner, S., Wagner, H.D., 1998a. "The material bone: structure-mechanical function relations". *Annual Review of Materials Science 28, 271-298*.

Weiner, S., Wagner, H.D., 1998b. "The material bone: Structure mechanical function relations". *Annual Review of Materials Science 28, 271-298*.

Wolff, J., 1892. "Das Gesetz der Transformation der Knochen (The Law of Bone Remodelling). Springer-Verlag, Berlin, Germany.

Xu, J., Rho, J., Mishra, S., Fan, Z., 2003. "Atomic force microscopy and nanoindentation characterization of human lamellar bone prepared by microtome sectioning and mechanical polishing technique". *Journal of Biomedical Materials Research Part A 67, 719-726*.

Yan, J., Mecholsky, J.J., Clifton, K.B., 2007. "How tough is bone? Application of elastic–plastic fracture mechanics to bone". *Bone 40, 479-484*.

Yang, L., Van der Werf, K.O., Fitié, C.F.C., Bennink, M.L., Dijkstra, P.J., Feijen, J., 2008. "Mechanical properties of native and cross-linked type I collagen fibrils". *Biophysical Journal 94, 2204-2211*.

Yang, Q., Cox, B., Nalla, R., Ritchie, R., 2006. "Re-evaluating the toughness of human cortical bone". *Bone 38, 878-887*.

Zappone, B., Thurner, P.J., Adams, J., Fantner, G.E., Hansma, P.K., 2008. "Effect of Ca2+ ions on the adhesion and mechanical properties of adsorbed layers of human osteopontin". *Biophysical Journal 95, 2939-2950*.

Zimmermann, E.A., Launey, M.E., Ritchie, R.O., 2010. "The significance of crack-resistance curves to the mixed-mode fracture toughness of human cortical bone". *Biomaterials 31, 5297-5305*.

Zimmermann, E.A., Schaible, E., Bale, H., Barth, H.D., Tang, S.Y., Reichert, P., Busse, B., Alliston, T., Ager, J.W., Ritchie, R.O., 2011. "Age-related changes in the plasticity and toughness of human cortical bone at multiple length scales". *Proceedings of the National Academy of Sciences 108, 14416-14421*.

Zioupos, P., Currey, J., 1998a. "Changes in the stiffness, strength, and toughness of human cortical bone with age". *Bone 22, 57-66*.

Zioupos, P., Currey, J.D., 1998b. "Changes in the stiffness, strength, and toughness of human cortical bone with age". *Bone 22, 57-66*.

Ziv, V., Sabanay, I., Arad, T., Traub, W., Weiner, S., 1996. "Transitional structures in lamellar bone". *Microscopy Research and Technique 33, 203-213*.

Zysset, P.K., Guo, X.E., Hoffler, C.E., Moore, K.E., Goldstein, S.A., 1999. "Elastic modulus and hardness of cortical and trabecular bone lamellae measured by nanoindentation in the human femur". *Journal of Biomechanics 32, 1005-1012*.

Notes